Observations of Upper Mesosphere Temperatures on Venus

and

Evaluation of Mid-Infrared Detectors for the Tuneable Heterodyne Infrared Spectrometer (THIS)

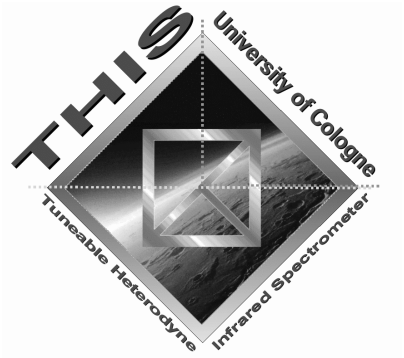

Inaugural-Dissertation
zur
Erlangung des Doktorgrades
der Mathematisch-Naturwissenschaftlichen Fakultät
der Universität zu Köln

vorgelegt von

Peter Krötz

aus Karlsruhe

im Mai 2010

Berichterstatter:

Prof. Dr. R. Schieder
Prof. Dr. S. Crewell

Tag der mündlichen Prüfung: Juli 2010

Contents

Abstract **1**

Zusammenfassung **2**

1 Introduction **5**

2 Infrared Heterodyne Spectroscopy **9**
2.1 Instruments: THIS 10
2.1.1 Spectrometer Details 10
2.1.2 The Local Oscillator 14
2.1.3 The Detector 19
2.2 Instruments: IRHS / HIPWAC 21
2.3 Expanding THIS to Longer Wavelengths 24
2.3.1 Comparison: Heterodyning vs. Direct Detection 24

3 Venus Atmosphere **29**
3.1 Venus Atmosphere: Models 30
3.2 Ground-based Observations 34
3.2.1 Sub-mm 35
3.2.2 Air-glow Measurements 38
3.3 Observations from Space 40
3.4 Non-LTE Emission 45

4 Observations **49**
4.1 THIS @ McMath 52
4.2 HIPWAC @ IRTF 58
4.3 IRHS @ IRTF 66

5 Data Analysis **71**
5.1 HIPWAC @ IRTF 71
5.2 IRHS @ IRTF 73
5.3 Short-Term Variations 74
5.4 Mid-Term Variations 76
5.4.1 Inferior Conjunction 76
5.5 Long-Term Variations 79
5.5.1 2007-2009 Maximum Elongation 79
5.5.2 1990-2009 Inferior Conjunction 80
5.6 Comparison to mm / sub-mm Observations 84
5.7 Comparison to model predictions 91
5.8 Conclusions 96

6 Expanding to longer wavelengths **99**
6.1 Motivation: Potential for Atomic and Molecular Line Spectroscopy 99
6.2 Molecular Hydrogen 100
6.2.1 Molecular Hydrogen in the Interstellar Medium (ISM) 100
6.2.2 Cold H_2 from CO 102
6.2.3 Star Formation and Protoplanetary Discs . . . 102
6.2.4 Molecular Hydrogen in Planetary Atmospheres 103
6.2.5 H_2 Observations 104
6.3 Preliminary Work - Astronomy 105

7 Laboratory Measurements **107**
7.1 Test setup for 17 μm 107
7.1.1 The pulsed 17 μm test-Laser 109
7.2 Detectors 110
7.3 Mercury-Cadmium-Telluride Photodiode 110
7.3.1 MCTs at 4 K 113
7.4 Quantum Cascade Detector 119
7.5 Results and Outlook 123

8 Conclusion and Outlook **124**

Acknowledgements **143**

List of Figures

2.1 THIS schematic 11
2.2 Diplexer Transmission 12
2.3 AOS schematic 13
2.4 QCL principle 14
2.5 THIS: present wavelength coverage 16
2.6 Detector stability 18
2.7 Detector stability 19
2.8 THIS 20
2.9 HIPWAC 23
2.10 Direct vs Heterodyne detection: signal-to-noise ratios 28

3.1 Model of Venus' Thermosphere 31
3.2 PVO T-Profile 33
3.3 Sub-mm measurements of CO 35
3.4 CO line centre variations 37
3.5 CO 2-1 observations 38
3.6 Temperatures from O_2 air-glow 39
3.7 Venus Express: VIRTIS 41
3.8 Venus Express: SPICAV 43
3.9 Venus Express: VeRa 44
3.10 Non-LTE emission: population inversion 47
3.11 VIRTIS: non-LTE altitude 48
3.12 Modelled non-LTE emission altitude 48

4.1 THIS Spectrum 52
4.2 Temperatures March 2009 53
4.3 Temperatures April 2009 55

4.4 Temperatures June 2009 56
4.5 HIPWAC spectrum 59
4.6 Temperatures HIPWAC 2007 60
4.7 All observed lines in the 10.6 μm P-branch 61
4.8 Line Intensities 63
4.9 Temperatures retrieved along the Equator 64
4.10 IRHS Spectrum 67
4.11 IRHS Temperatures 1990 69
4.12 IRHS Temperatures 1991 70

5.1 Venus polar vortex 73
5.2 Variations at Equator / Limb 74
5.3 Temperatures at Limb (June '09) 75
5.4 IC 2009: Temperature Symmetries 77
5.5 ICs 1990/91: Temperature Symmetries 78
5.6 Comparison of ICs 1990/91 / 2009 80
5.7 Sub-mm observing Geometry 81
5.8 Inter heterodyne comparison 82
5.9 Solar Cycles 19-24 83
5.10 Simultaneous Observation Sub-mm / IRHet: Equator 85
5.11 Simultaneous Observation Sub-mm / IRHet: Equator 85
5.12 Simultaneous Observation Sub-mm / IRHet: South Pole 86
5.13 Sub-mm observing Geometry 88
5.14 Comparison: THIS/sub-mm at max. elongation . . . 89
5.15 Long-term mm observations 90
5.16 Venus Atmosphere: IC Model 93
5.17 IC Model (2) 94
5.18 Comparison to VTGCM 95

6.1 Zeeman splitting of Solar lines 100
6.2 Telluric Ozone Absorption against Betelgeuse 106

7.1 Optics transmission I 108
7.2 Optics transmission II 108
7.3 17 μm laser emission 109
7.4 MCT material dependence 110
7.5 Long wavelength reference detector 111

7.6 THIS - MCT 112
7.7 Comparison JMCT RMCT 114
7.8 Power meter absorption 115
7.9 MCT temperature dependence 116
7.10 RMCT resistance 116
7.11 RMCT @ 9μm 117
7.12 RMCT @ 13μm 117
7.13 RMCT @ 17μm 118
7.14 QCD schematic 119
7.15 Quantum cascade detector 120
7.16 QCD illumination 120
7.17 QCD responsivity 121
7.18 Pulsed QCD response 122

List of Tables

4.1 Results March 2009 54
4.2 Results April 2009 55
4.3 Results June 2009 57
4.4 Results IRTF 2007 62
4.5 Comparison rotational / kinetic temperature 63
4.6 Kinetic temperatures along the equator 65
4.7 IRHS observing campaigns 66
4.8 IRHS: temperature results 68

5.1 Comparison rotational / kinetic temperature 71

6.1 THIS sensitivity characteristics at 17 μm 105

7.1 MCT response 113

Abstract

Infrared heterodyne spectroscopy today is an inherent part in planetary atmosphere observations. It is based on the superposition of the observed signal to a local oscillator and provides highest possible spectral resolution. Non-thermal emission of CO_2 in the upper mesosphere of Venus was discovered by the NASA Infrared Heterodyne Spectrometer (IRHS) in the 1970s and was repeatedly target of observations since then. In the course of this thesis, data of with IRHS, its successor HIPWAC and the Cologne Tuneable Heterodyne Infrared Spectrometer (THIS) was taken or analysed. From the measured line widths the kinetic temperature of the atmosphere at the emission altitude of around 115 km could be determined.
Observed temperatures are generally higher than predicted by the Venus International Reference Atmosphere (VIRA). VIRA is a empirical model mainly based on data of the Pioneer Venus space mission and exhibits only a limited data set.
Other ground-based observations as well as results from Venus Express confirm the warm atmosphere at similar altitudes. At the day side of Venus and at this specific altitude, infrared heterodyne spectroscopy is currently the only method to observe temperatures.
Another result is the high variability of the observed atmosphere which is not expected by the VIRA model but which was also seen in earlier mm-wavelength observations. The obtained results also set new constraints for modern global circulation models. Improving those models will lead to a improved knowledge of planetary atmospheres. As all those models are based on the Earth atmosphere model, our observations might subsequently lead to a better understanding of the terrestrial climate as well.

The second part of this thesis deals with the evaluation of possible detectors for THIS to expand the wavelength coverage to longer wavelengths. Many atomic and molecular lines could be targeted within the solar system and beyond. The main target will be cold molecular hydrogen in the interstellar medium which is of highest importance in astrophysical questions concerning star forming, dark matter and cosmology. For this reason first tests at 17 μm wavelength were done in the course of this work.

Zusammenfassung

Infrarot Heterodyn Spektroskopie hat heute ihren Platz in der Planetenbeobachtung gefunden. Sie beruht auf der Überlagerung des beobachteten Signals mit einem Lokaloszillator und bietet höchstmögliche spektrale Auflösung. Nicht-thermische CO_2 Emission in der oberen Mesosphäre der Venus wurde mit dem Infrared Heterodyne Spectrometer (IRHS) des NASA Goddard Space Flight Centers entdeckt, und seit den Siebziger Jahren des vergangenen Jahrhunderts regelmäßig beobachtet. Daten von IRHS, dem Nachfolgegerät HIPWAC (Heterodyne Instrument for Planetary Wind and Composition) und dem Kölner Spektrometer THIS (Tuneable Heterodyne Infrared Spectrometer) wurden im Rahmen dieser Arbeit aufgenommen, bzw. ausgewertet. Anhand der Linienbreite der CO_2-Emission konnte die kinetische Temperatur der Venusatmosphäre in einer Höhe von circa 115 km bestimmt werden.
Im Vergleich zur Venus Referenzatmosphäre (VIRA, Venus International Reference Atmosphere) sind die erhaltenen Temperaturwerte deutlich höher, um bis zu 50 K. VIRA wurde empirisch anhand von Satellitenmissionen (hauptsächlich die Pioneer Venus Mission) erstellt und weist an vielen Stellen nur einen unzureichenden Datensatz auf.
Andere bodengebundene Beobachtungen sowie Experimente an Bord des aktuellen Orbiters VenusExpress bestätigen die tendenziell wärmere Venusatmosphäre in vergleichbaren Höhen. Infrarot Heterodyn Spektroskopie ist allerdings die einzige Methode um die Temperaturen in dieser Höhe auf der Tagseite und mit hoher räumlicher Auflösung zu messen.
Aus einzelnen Meßkampagnen sowie im Vergleich mit anderen Messungen ergibt sich ein extrem variables Bild der Venus Atmosphäre in 115 km Höhe. Dies war laut VIRA nicht zu erwarten und stellt Ansprüche an neue Atmosphärenmodelle. Da sich die Modelle der Planetenatmosphären in der grundlegende Physik nicht unterscheiden können Verbesserungen des Venusmodells auch dazu beitragen das Verständnis physikalischer Vorgänge in der Erdatmosphäre und somit der Entwicklung des Erdklimas zu verbessern.

Weiterhin war es Ziel dieser Arbeit, den Wellenlängenbereich des THIS Spektrometers zu längeren Wellenlängen zu erweitern. Zahlre-

iche Molekül- und Atomlinien könnten so in Planetenatmosphären und auch extrasolar beobachtet werden. Das Hauptziel dabei ist die Beobachtung von kaltem molekularen Wasserstoff im interstellaren Medium. Wasserstoff ist der grundlegende Baustein des Universums, zahlreiche Fragen der Kosmologie, z.B. die nach der dunklen Materie, oder der Sternentstehung sind mit der Verteilung und der Häufigkeit von Wasserstoff verknüpft.
Erste Labortests bei 17 μm Wellenlänge sowie eine Evaluierung geeigneter Detektoren wurden dazu durchgeführt.

Chapter 1

Infrared Heterodyne Spectroscopy: Research and Development

Infrared Heterodyne (IRHet) Spectroscopy fills a niche in today's astronomical instrumentation. Its characteristics - ultra high spectral resolution over a relatively small bandwidth - call for very distinct science applications.

While heterodyne techniques are state of the art at radio and THz frequencies, observations in the infrared atmospheric windows are dominated by direct detection systems.

In the mid 1970s a group at the NASA Goddard Space Flight Center (GSFC) near Washington D.C. started to develop an **I**nfra**r**ed **H**eterodyne **S**pectrometer (IRHS) which later was redesigned and upgraded to the **H**eterodyne **I**nstrument for **P**lanetary **W**ind **A**nd **C**omposition (HIPWAC). Together with the Cologne **T**unable **H**eterodyne **I**nfrared **S**pectrometer (THIS) these two instruments today are the only ones applying heterodyne techniques in the mid-infrared.

The mid-infrared around wavelengths of 10 μm is a transition zone, where one has to decide which technique is more favourable. If high spectral resolution is not needed, direct detection can provide higher sensitivities. For some applications, however, the ultra high

spectral resolution of heterodyne spectroscopy is needed. The key science application from the beginning of IRHet was the observation of planetary atmospheres, more precisely of planetary atmosphere dynamics. There, spectral resolution of more than 10^5 ($\nu/\delta\nu$) is mandatory.

In this thesis IRHet observations are analysed for mesospheric temperatures for the first time. Therefore, temperature dedicated observing runs with the instruments THIS and HIPWAC are analysed as well as old IRHS data, taken in 1990 and 1991. These data are extremely valuable for the verification of global circulation models of planetary atmospheres, which recently developed very fast thanks to data from orbiters like Mars- and VenusExpress. A better understanding of atmospheres around other planets will ultimately also increase the knowledge about our own atmosphere and help to refine models on climate change. In this way, observations of temperatures in the upper mesosphere of Venus are of great interest concerning relevant ongoing discussions about global warming on Earth.

Temperatures can be retrieved by investigating the line width of non thermal emission of CO_2. This effect takes place in a distinct pressure region in the upper mesosphere of Venus, roughly corresponding to 115 km altitude. The line with is purely determined by the kinetic temperature of the emitting gas. Due to the low pressure environment - the emission originates around $5 \cdot 10^{-}3$ mbar - the emission can be fitted using a Gaussian line profile. The narrow line width of some ten MHz make ultra high spectral resolution necessary in order to fully resolve the lines. Thus, infrared heterodyne spectrometers are the only possible instruments to realise such measurements.

Compared to other possibilities to measure atmospheric temperatures on Venus, infrared heterodyne spectroscopy has some strong advantages: it is the only way to observe temperatures at this specific altitude an the day side of Venus, and it has a very high spatial resolution compared to other ground-based observation techniques like mm or sub-mm measurements. Those observations can retrieve temperature profiles over big altitude regions, but always have a convolution of temperatures across a big fraction of the Venus disc.

Apart from planetary atmospheres, infrared heterodyne spectroscopy has more potential scientific targets like the observations of transition lines of molecules without permanent dipole moment. These molecules are not observable at radio frequencies, and the

lines can only be fully resolved by infrared heterodyne spectroscopy. There are many molecules of astrophysical interest, e.g. Acetylene (C_2H_2, band centre at 13.5 μm) and other hydro carbons which also play a role in astro biology. They are the ingredients to form more complex biological molecules like amino acids. It is therefore of great interest to study those molecules in the vicinity of star forming regions.
An ideal future target would be the ground state transitions of molecular hydrogen at 17 and 28 μm . Seen in absorption against warm background sources, this would be a method to investigate the distribution of H_2 in the cold interstellar medium, which today can only be deduced indirectly e.g. by correlating it with the distribution of CO. Molecular hydrogen can be a solution of many fundamental astrophysical questions like dark matter and star forming processes.

To reach these goals it is necessary to extend the wavelength coverage of THIS to longer wavelengths. This is subject of the second part of this thesis by evaluating possible detectors, capable of heterodyne detection up to 17 micron. Current semiconductor photo diodes are tested at temperatures down to 4.6 K. Also, novel detectors like the Quantum Cascade Detector are studied for their potential in infrared heterodyne spectroscopy.

The layout of this work is as follows: in chapter 2, I will introduce the basics of infrared heterodyne spectroscopy and an overview of the three used instruments for temperature measurements in the atmosphere of Venus: THIS, HIPWAC and IRHS. Chapter 3 will summarise the knowledge about Venus's atmosphere with emphasis to its temperature distribution and I will show other methods of temperature retrieval. Observations results and data analysis will be presented in chapters 4 and 5. In the second part I present possible targets at longer wavelengths in chapter 6, and chapter 7 will finally address first tests of possible long wavelength detectors.

Chapter 2

Infrared Heterodyne Spectroscopy: Instruments

Heterodyne spectroscopy provides the highest possible spectral resolutions in the mid-infrared. There are two operating spectrometers, the Cologne Tuneable Heterodyne Infrared Spectrometer (THIS) and the Heterodyne Instrument for Planetary Wind And Composition (HIPWAC). HIPWAC is a new and transportable redesign of the NASA Goddard Space Flight Center Infrared Heterodyne Spectrometer (IRHS). Results of all three instruments will be presented in this thesis. In this chapter, I will briefly explain the principles of heterodyne spectroscopy and introduce the characteristics and differences of the instrumental implementation. Emphasis will be laid on the linewidths of the local oscillators as this is the key element when calculating kinetic temperatures in planetary atmospheres from observed linewidths. For a more detailed overview of the rest of the spectrometer, see the thesises of Manuela Sornig [1] and Guido Sonnabend [2]. Finally I will discuss theoretical aspects of the advantages in sensitivity of heterodyne spectroscopy when moving to longer wavelengths.

Heterodyne Spectroscopy is commonly used in radio wavelengths. Used in the infrared, it provides unrivalled high spectral resolution (up to $3 \cdot 10^7$). The basic principle of heterodyning is to generate a beat spectrum with the astronomical source signal and the local oscillator (LO) and thus to mix the spectrum down from high (tens of THz) to radio frequencies, creating the 'intermediate frequency' (IF). All spectroscopic information is maintained in that process. After

that, amplification and signal processing is rather easy using standard radio devices.
The total electric field at the detector is the superposition of the electric fields of the LO and the source. This has some important consequences: only one polarisation is detectable as the LO is usually linearly polarised. And the resulting spectrum is 'double sideband' (DSB) as the detector can not distinguish between frequencies below or above the LO:

$$I_{det}(t) \sim I_{DC} + 2\sum \sqrt{I_{lo} \cdot I_{sig}} \cos(\Delta\omega_i \cdot t)$$

I_{DC} represents all 'fast' components, at the original frequencies or the sum thereof, which are all averaged by the detector to a constant DC current. Thanks to the high spectral resolution DSB detection imposes usually no problem as single lines can usually still be distinguished, even if originating from different sidebands.

2.1 Instruments: THIS

2.1.1 Spectrometer Details

The outline of the Cologne Tuneable Heterodyne Infrared Spectrometer (THIS) is the following: the telescope beam is optically matched to the spectrometer in superimposed to the frequency stabilised LO by means of the diplexer. The mixing is done by a Mercury-Cadmium-Telluride (MCT) detector and the IF is analysed by an Acousto-Optical Spectrometer (AOS). A schematic of the spectrometer is shown in Fig 2.1. In the following I will describe the single components in more detail.

Optical Beam Matching and Guiding

THIS can be adapted to match different beam conditions at any telescope resulting from different telescope optics. This can be done at the top of the spectrometer (see Fig 2.8) by choosing the correct off-axis parabolic mirrors to collimate the beam into the spectrometer. Gaussian optics is used to determine the necessary focal lengths. A dichroic mirror is used to separate infrared (being fed into the spectrometer)

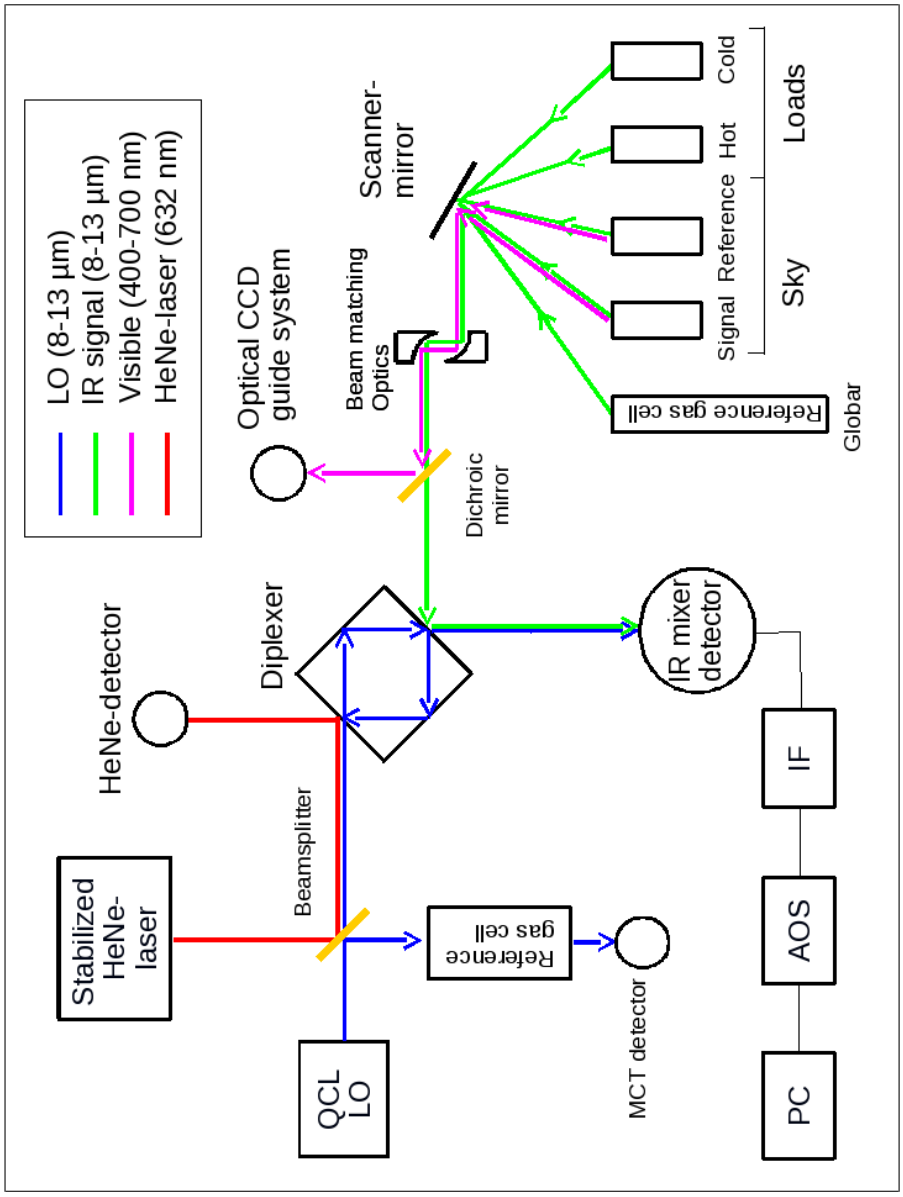

Figure 2.1: *THIS (schematic) Different signals - source, background sky, hot load, cold load, calibration gas cell - can be chosen with a fast scanner mirror. The LO is then stabilised and superimposed to the signal by means of the diplexer. The difference frequency is detected by a MCT and the spectrum is expanded by an acousto optical spectrometer.*

from visible radiation which is monitored by a CCD camera to guarantee correct pointing. A scanner mirror enables fast scanning between two sky positions (signal and reference), two calibration loads at known temperature (hot and cold) and a reference gas cell for absolute frequency precision.

The Diplexer

The diplexer - a confocal Fabry-Pérot ring resonator consisting of two elliptical mirrors and two beamsplitters - is the central optical element in the spectrometer THIS. Other than a beamsplitter, it provides more than 95% signal reflection while at the same time transmitting up to 60% LO power and thus enhancing the superpositioning of the two beams. The frequency stability of the LO is ensured by locking it to a transmission maximum of the diplexer using a PI control loop. The diplexer itself is locked with a second PI control to a commercially available frequency stabilised Helium-Neon laser (stable to 10^{-8} in 1 hour).

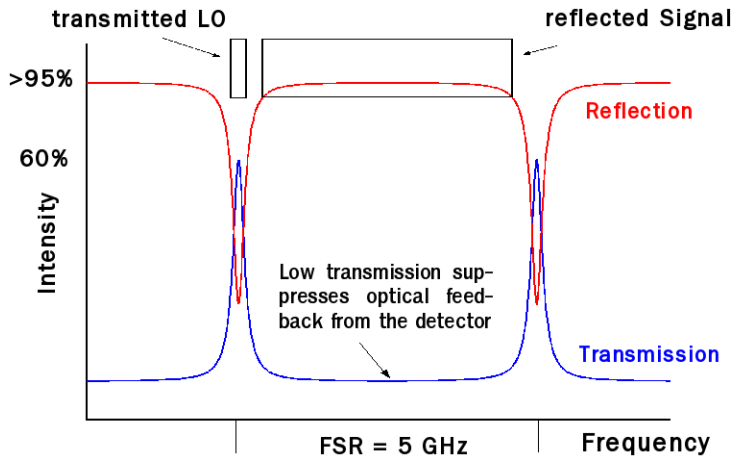

Figure 2.2: *The diplexer transmits at its resonances ∼60% LO power while more than 95% of the signal get reflected in the free spectral range (FSR) in between. The low transmission in the FSR filters out any unwanted optical feedback from the detector facet.*

The Acousto-Optical Spectrometer

The difference frequency is analysed with an in-house-built acousto-optical spectrometer (AOS) with an instantaneous bandwidth of 3 GHz [3, 4]. In the AOS, the spectral distribution of the IF signal is converted into a spatial distribution of laser light which can be detected by a linear CCD chip. This is achieved by feeding the IF into a crystal (the Bragg cell) with a piezoelectric transducer. The thus generated ultrasonic waves modulate the refractive index of the Bragg cell. A laser is now diffracted by this new phase grating and detected by the CCD, see Fig. 2.3. The diffraction is happening instantaneously for all frequencies of the IF signal. The AOS back-end is setting the constraints of $\sim$ 1 MHz spectral resolution and 3 GHz DSB bandwidth.

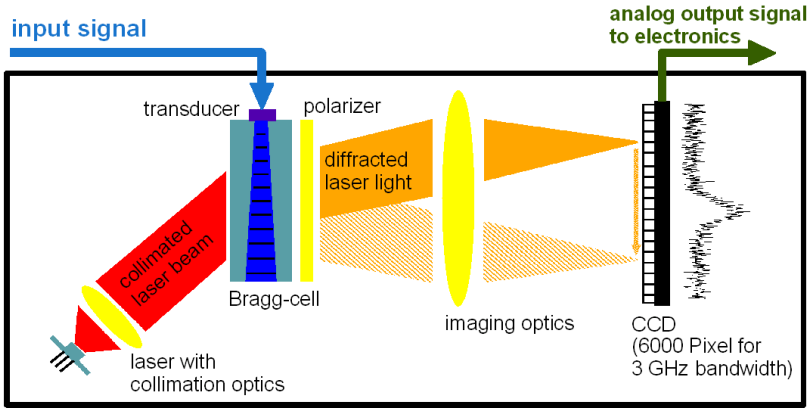

Figure 2.3: *Schematic of the Acousto Optical Spectrometer back-end [5].*

2.1.2 The Local Oscillator

As local oscillator a quantum cascade laser (QCL) is used. These state-of-the-art semiconductor lasers, suggested and discussed by Kazarinov et al. [6] and realised only 15 years ago [7], today are a powerful alternative to other laser sources because of their little size and wavelength coverage. Other advantages like high output power and room temperature operation are also evolving recently. For this work especially the linewidth of the QCL is important as the temperatures in the Venus atmosphere are directly inferred from the width of non-LTE emission lines. As two linewidths add quadratically, $w_{total} = \sqrt{w_{LO}^2 + w_{QCL}^2}$ assuming Gaussian line shapes for both lines, a sufficiently small LO linewidth is needed to avoid systematical errors in the temperature measurements.

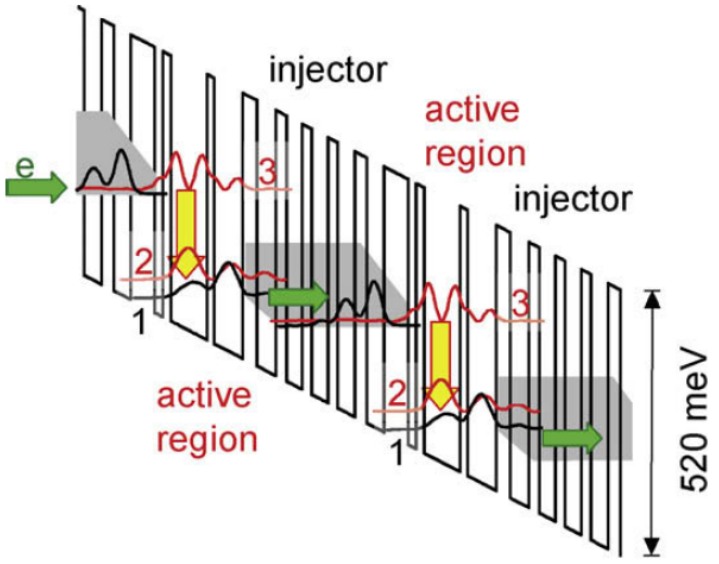

Figure 2.4: *Energy diagram of a quantum cascade laser. The energy levels and the corresponding probability distributions obtained from solving Schrödinger's equation are shown. [8]*

QCL operating principle

A QCL is a multi layer semiconductor sandwich e.g. made out of GaInAs and AlInAs, creating potential or quantum wells of different sizes according to the thickness of the layers. A bias voltage is applied to shift the wells to an energy staircase. There are two distinct regions alternating: the active region and the injector.
In the active region electrons can jump between energy levels 3 and 2 (see Fig. 2.4) creating a laser photon. The needed population inversion is realised by positioning a lower energy level 1 nearby to level 2, so that the electrons can scatter very fast into level 1 by phonon emission.
The following injector region is designed such, that there is no resonant electronic state corresponding to level 3, but a variety of states (the miniband) corresponding to levels 1 and 2. The electron is then transferred into energy level 3 of the following active region by resonant tunneling, and the whole process can start again from the beginning
One electron can thus emit as much photons as existing active regions (typical several tens up to ~ 100) resulting in an intrinsically high lasing power of QCLs.

In principle, QCLs can be produced at any given wavelength from the near infrared up to the far infrared and THz regime. There are restrictions like the reststrahlenband, which is inherent to the commonly used QCL material gallium arsenide, and prevents efficient lasing between $\sim$30 and 50 micron. But this also can be avoided by using other materials which is currently investigated. This in principle enables THIS to continuously cover a full wavelength range from about 7 to 17 micron.

An overview of currently available lasers for THIS is displayed in Fig. 2.5. Usually a QCL is used with an applied grating (called 'distributed feedback', DFB) to force the laser to single mode emission. The laser can then be tuned in frequency by a few wavenumbers by changing the laser current and temperature. Without a DFB structure, as a pure Fabry-Pérot cavity, a QCL is running multimode and therefore it is needed to be controlled by an external cavity (EC). This method, which proved to operate nicely in our laboratory [9], will enable THIS to continuously cover wavelength regions as large as 2 micrometres with a single QCL device.

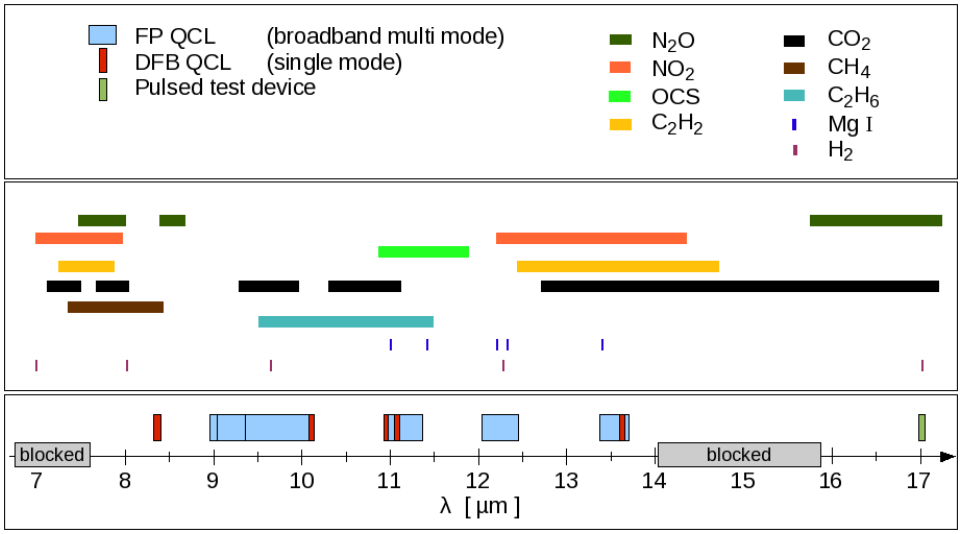

Figure 2.5: *Wavelength coverage of THIS: plotted are the available laser frequencies at the bottom (light blue and red), and some important molecular bands or transitions. Around atmosphere transmission is blocked at 7 and 15 µm by water vapour and CO_2. Fabry-Pérot type QCLs need external cavity control.*

Laser linewidth

QCL intrinsic linewidth

The quantum limit of a laser linewidth was given by Schawlow and Townes [10] even before the first laser was realised:

$$\delta\nu_{(ST)} = \frac{2\pi \cdot h\nu \cdot (\Delta\nu_{tr})^2}{P_{out}}$$

where $(\Delta\nu_{tr})^2$ is the linewidth of the laser's atomic or molecular transition, P_{out} is the output power. Losses in the cavity or from the mirrors are neglected. In semiconductor lasers, a much broader linewidth was found and the Schawlow-Townes formula was appended by a factor $(1+(\alpha_e)^2$[11]. This 'Henry linewidth enhancement factor' is due to the coupling between intensity and phase noise. The refractive index is dependent on the carrier density in the semiconductor. Electron density fluctuations then create refractive index variations causing a line broadening of the laser. QCLs, however, are only insignificantly affected by refractive index variations, therefore the α_e value is assumed close to zero [7, 12].

Now we can estimate the minimum linewidth of a QCL, given a typical output power of 10 mW and a photon lifetime of 1.5 ps [13]. The expected Schawlow-Townes linewidth is then in the order of 200 kHz. Yet, recently there has been shown that the Schawlow-Townes formula is only the upper limit for a quantum limited linewidth (discussed e.g. in [14]). A modification of the Schawlow-Townes formula, adapted to the quantum cascade laser design was given by Yamanishi et al. [15]:

$$\delta\nu = \frac{1}{4\pi}\frac{\gamma\beta_{eff}}{1-\epsilon} \cdot [\frac{1}{(I_o/I_{th}-1)} + \epsilon] \cdot (1 + (\alpha_e)^2)$$

Here, the ϵ-factor is calculated from the lifetimes of the involved energy levels, γ is the inverse photon lifetime, β_{eff} the 'effective coupling' of the spontaneous emission and the (only) experimental parameter is the ratio of the operating current I_o to the threshold current I_{th}. The effective coupling of the spontaneous emission is given by the ratio of the spontaneous emission rate coupled into the lasing mode to the total relaxation rate. Above the laser threshold, the fast non-radiative relaxation process run in parallel with the spontaneous emission. This competition leads to a strong suppression of the noise associated with spontaneous emission and to a linewidth reduction.
Recently, the intrinsic linewidth of a free-running DFB QCL was claimed to be ∼500 Hz (at $I_o/I_{ht} = 1.5$) [12], and two frequency locked QCLs showed a relative linewidth of 5.6 Hz [16].

Early measurements with THIS using a lead salt diode laser as LO and a external cavity controlled QCL as signal, detected a beat signal at the resolution bandwidth of the spectrometer (1.5 MHz) [17], indicating a QCL width of well below 1.5 MHz (assuming Gaussian line shapes, the two lines add up following $w_{total} = \sqrt{w_{LO}^2 + w_{QCL}^2}$), see Fig. 2.6. Recent experiments in the laboratory with THIS using a DFB QCL as LO and an EC QCL as signal showed a minimum linewidth of 5 MHz during short integration times of around 0.1 s, and up to 15 MHz when integrating at time scales comparable to observing (2-5 min). However, this broadening is attributed to instabilities in the external cavity stabilisation control setup which is still in a phase of early development. Possible pick-up of noise (due to the piezo controlled cavity lengths, to several loop-back control circuits and to the laser power supply) can easily lead to such a broadening.
In the literature, EC QCL linewidths have been measured in the range of 20-30 MHz [18, 8]. Without the lock of a distributed feed-

back grating, the dominant broadening was also attributed to the noise of the laser power supply [8].
The upper limit for the noise of the Spectra-Physics power supply of the THIS EC QCL is given to be 50 μA which would explain the broadening of 5 MHz given the QCL frequency/power dependency of 1 GHz per 11 mA.
Still, even when assuming 5 MHz as linewidth of the local oscillator of THIS, this will lead only to a broadening of $\sim$310 kHz in the measurement of a FWHM = 40 MHz Venusian emission line (40 MHz is a lower limit, measured linewidths are usually around 45 MHz, see chapter 6.2.5, reducing the broadening effect of a noisy LO). This is well within the error bars of the temperature retrieval. As worst-case scenario with both lasers contributing equally to the 15 MHz broadening after two minutes of integration time, a FWHM of 10.6 MHz of the LO would result in an extra line broadening of 1.38 MHz resulting in an temperature error of $\sim$10 K.
Concluding this paragraph, I don't assume the LO linewidth to broaden the measured non-LTE emission line significantly, but a final experiment to verify this assumption has to be done in the near future.

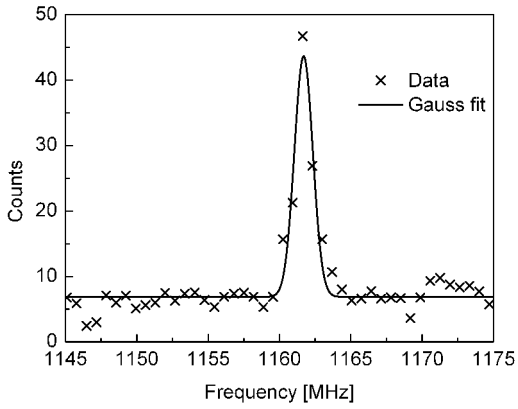

Figure 2.6: *Direct heterodyne linewidth measurement of a cw QCL at 9.2 μm . The QCL emission was fed as a signal into THIS. The emission was fitted with a Gaussian. The calculated linewidth of 1.53 MHz reproduces the fluctuation bandwidth of the spectrometer; therefore the laser linewidth is well below 1.53 MHz [17].*

Laser stability

The spectral stability of the system was tested in the laboratory. To simulate observing conditions, a reference gas cell was observed for ~ 1 second every 30 s for 75 minutes. The result is shown in Fig. 2.7. The standard deviation of the spectral position of the QCL is 300 kHz. Long term deviations and concurrent line broadening can be ruled out due to the frequent measurements of the reference cell within the astronomical observation.

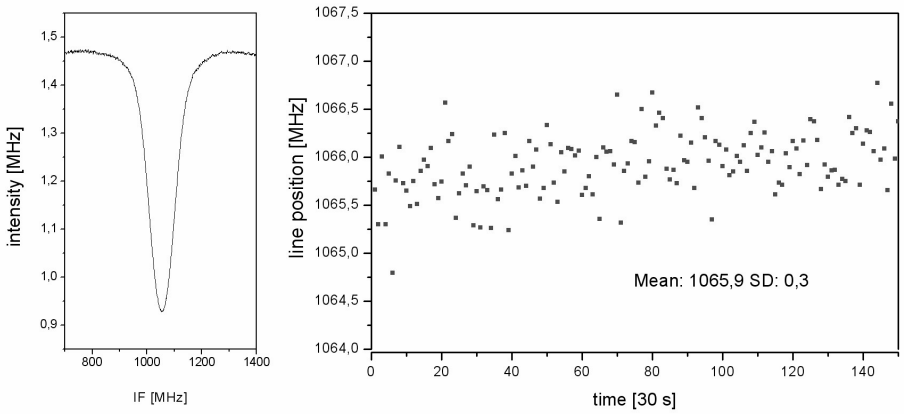

Figure 2.7: *Stability measurement using a ethylene gas cell*

2.1.3 The Detector

Currently a fast Mercury-Cadmium-Telluride (MCT) photo diode is implemented as mixer/detector in THIS. It is equipped with an optical resonant cavity in which the incident infrared radiation is reflected several times. This enhances the absorption and thereby increases the quantum efficiency of the detector. To cover a wide spectral range, the chip contains four elements, each optimised for adjacent wavelength regions, enabling a coverage from 7.5 - $\sim$12 μm . Quantum efficiencies of more than 80% are reached.
For the measurements at higher wavelengths, chapter 7, another MCT detector without resonant cavity was used. There, I will also go more into detail on MCT detectors in general.

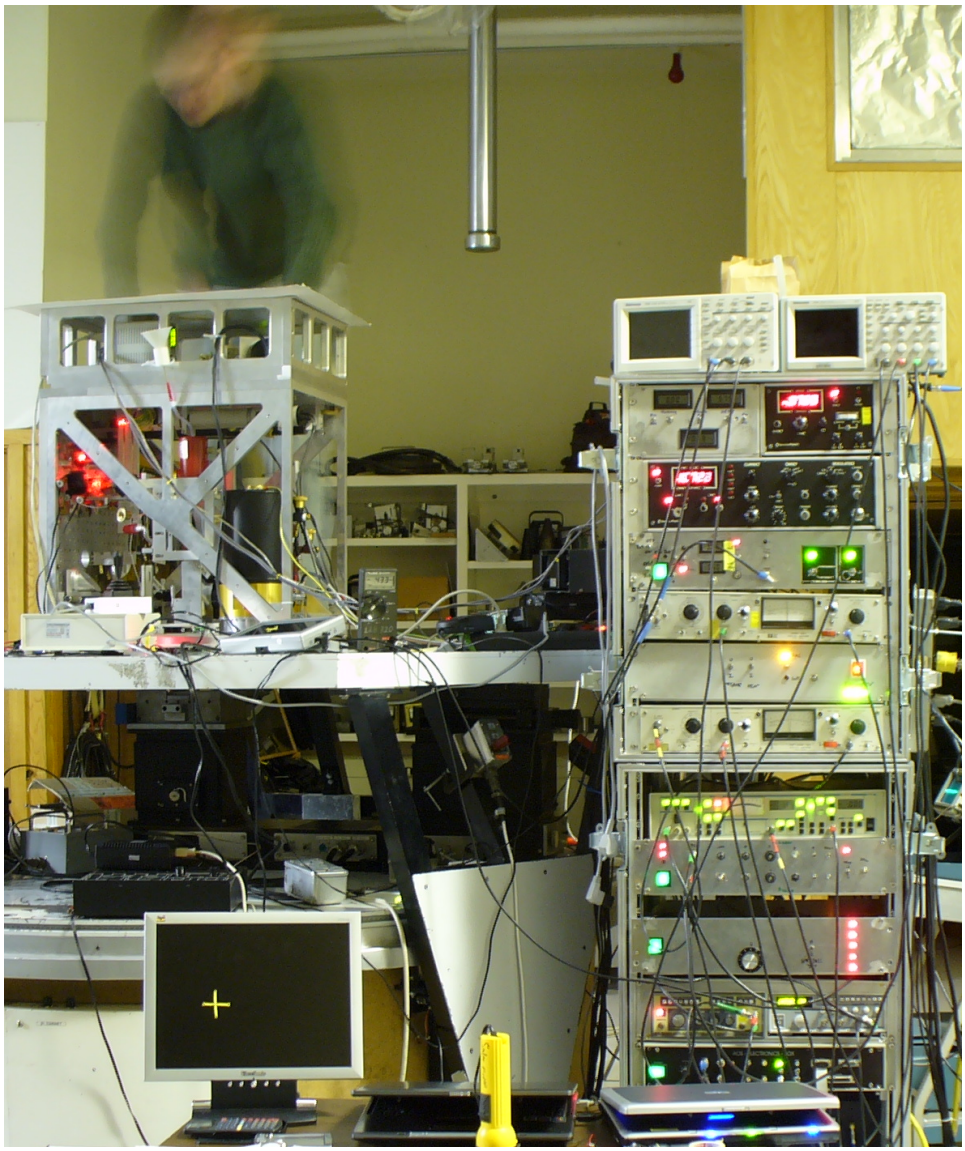

Figure 2.8: *THIS set up at the observing table at the McMath-Pierce Solar Telescope, Kitt Peak. The spectrometer is the aluminium cube with the fading author above. On the right the corresponding electronics can be seen.*

2.2 Instruments: IRHS / HIPWAC

Infrared Heterodyne observations of planetary atmospheres already started in the 1970s with the detection of the non-LTE emission in the atmosphere of Mars. Since then, both planets, Venus and Mars were observed many times, mostly studied for winds and atmospheric composition. But much of the accumulated data was not analysed for temperatures. Within this work it was possible to re-analyse data taken in four observing runs from January 1990 until September 1991. Similar to both campaigns in March and April 2009 with THIS, Venus was observed shortly before and after inferior conjunction.

The first infrared heterodyne spectrometer (IRHS) was implemented in 1976 at the NASA Goddard Space Flight Center (GSFC) [19]. It was used at the Coudé foci of the McMath-Pierce Solar Telescope at Kitt Peak and the IRTF on Mauna Kea. When the Coudé room of the IRTF was decommissioned, a transportable version was built, the Heterodyne Instrument for Planetary Wind And Composition (HIPWAC), being able to operate at the Cassegrain focus of the IRTF. The principle is of course the same as for THIS, in fact, both spectrometers make use of identical MCT detectors, but there are some big differences in the layout of both spectrometers.

The local oscillator

A CO_2 gas laser is the local oscillator of IRHS/HIPWAC. It is possible to switch between two laser tubes which can be operated with different CO_2 isotopes and at various transitions to cover as much wavelength regions as possible. The desired transition can be selected by tilting an incorporated diffraction grating. The LO beam is also optically matched with the telescope beam before heterodyning.

The high output power of CO_2 lasers is an advantage compared to early QCLs or lead salt diode lasers, it even makes attenuation necessary, but the tuneablitiy is restricted to a small region around the transition frequencies which can be realised by pressure and laser cavity alignment variations. The laser frequency can be stabilised using Lamb dip stabilisation (IRHS see below) or power peak stabilisation (HIPWAC) where the emission is locked to the peak of the laser gain profile.

Lamb dip stabilisation Using Lamb dip stabilisation, the centre frequency of the LO can be stabilised very precisely within $\sim$0.1 MHz [20]. This is realised by introducing a absorption cell into the laser cavity. Molecules in this cell will resonantly absorb radiation at the rest frequency of the laser transition (ν_{lt}). In the case of IRHS, molecules then radiatively relax to the ground state by emitting a photon at 4.3 μm wavelength (which is the dominant de-excitation pathway compared to the 9.4 and 10.4 μm bands) which can be monitored. If the laser ν_{lo} is detuned from ν_{lt}, molecules can still absorb if their velocity along the cavity axis is Doppler shifting the laser photons from ν_{lo} to ν_{lt} in the molecule's rest frame. This can be done in both axial directions. Shifting ν_{lo} towards ν_{lt} increases the 4.3 μm emission as more molecules inhibit the right axial velocity. At $\nu_{lo} = \nu_{lt}$ only molecules with the axial velocity = 0 do absorb the radiation, leading to a dip in 4.3 μm emission. Also, molecules being excited in the initial path leave fewer molecules to be excited in the return path of the cavity, which is further amplifying the dip.

Linewidth The initial laser gain width is dominated by the pressure broadening of 7.5 MHz/Torr for CO_2 yielding a $\sim$170 MHZ gain profile at $\sim$ 20 Torr gas pressure. The effective length of the laser cavity then selects the actual laser frequency which has a very narrow Lorentzian profile of less than 10 kHz FWHM for IRHS and basically the same value for HIPWAC.

Beam switching and Heterodyning

The switching between sky signal, sky reference can be done by using the wobbling secondary mirror at the IRTF, which can be synchronised to the observing process of double beamswitch, or a by chopper wheel by which also a blackbody calibration source can be selected. The superpositioning of the signal radiation to the local oscillator is achieved by using a ZnSe beam splitter.

Back-end IF Analysis

The IF is analysed by two 64 channels RF filter banks. One low resolution filter bank with 25 MHz filter width providing a bandwidth of 1.6 GHz. The high resolution (5 MHz, 320 MHz bandwidth) filter

bank can be tuned within the low resolution bandwidth by mixing the IF with a radio frequency local oscillator. In this way narrow features like line peaks can be investigated using the high resolution filter bank, while broad features like the line wings are sufficiently resolved by the low resolution filter bank.

In recent years, HIPWAC also is starting to use an AOS back-end spectrometer and is currently evaluating QCLs as local oscillators due to the successful operation of both elements in THIS.

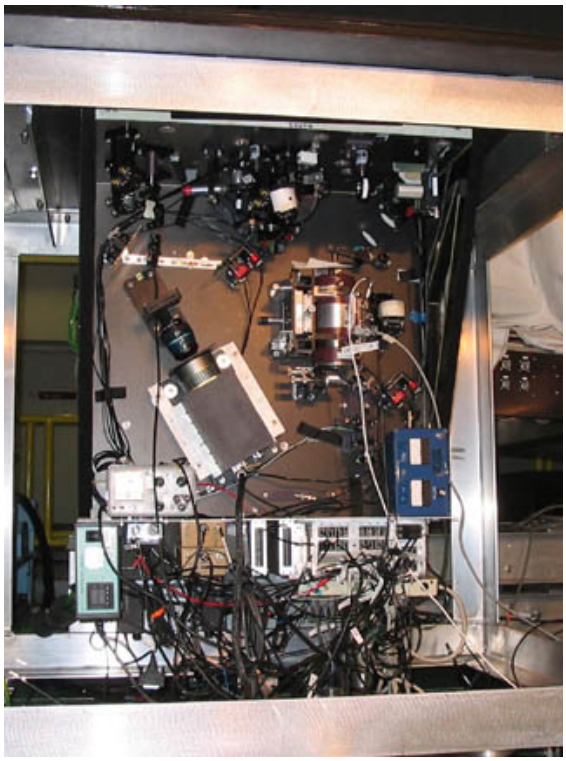

Figure 2.9: *HIPWAC mounted at the Subaru telescope.*

2.3 Expanding THIS to Longer Wavelengths

One main part of this thesis is the evaluation of mid-infrared detectors for THIS, with emphasis to longer wavelengths than 10 μm . A detailed presentation of possible targets and laboratory measurements will be given in chapters 6 and 7. In this section, I will discuss the instrumental pros and cons, including a brief comparison to direct detection techniques.

Leaving the CO_2 region

Beyond 12 micron, there are many scientific targets which call for high spectral resolution, see chapter 6. THIS is currently starting to implement LOs with longer wavelengths, making it a unique instrument in that wavelength region. There are molecules without permanent dipole moment like Acetylene which are not detectable at radio wavelengths or atomic lines like Magnesium (I) where investigations of magnetic field induced Zeeman splitting makes high spectral resolution necessary. In contrast to HIPWAC which is restricted to narrow areas surrounding the CO_2 transitions, THIS can in principle cover any wavelength region, given the availability of QCLs.

2.3.1 Comparison: Heterodyning vs. Direct Detection

Infrared heterodyne spectroscopy fills a niche in contemporary astrophysical instrumentation. Usually, direct detection systems with spectral resolutions of up to 10^5 are used for investigating astronomical problems if high spectral resolution is needed. Direct detection involves a dispersive element (usually a grating) and has obvious advantages like not being limited by the quantum limit and by instrumental limits of the bandwidth. On the other hand, if extremely high spectral resolution is needed (10^6 or higher) direct detection is limited by the size of the necessary grating, which scales with the product of wavelength and spectral resolution. At 10 μm wavelength and spectral resolution of 10^5 the necessary size of the grating (which needs to be cryogenically cooled to reduce background noise) is already 1 m and therefore on the limit of technical feasibility.

The quantum limit

Every heterodyne receiver adds noise to the observation. A convenient measure of this is the system temperature T_{sys}, an expression used in radio astronomy. It can be viewed as the transfer of all noise contributions of the receiver to an external source which then can be described by a brightness temperature a hypothetical, noise-free receiver would see. The lower boundary of the system temperature is given by the so called 'quantum limit':

$$T_{QL} = \frac{h \cdot \nu}{k_B}$$

It is the noise seen after the mixer of an ideal heterodyne receiver where all external noise contributions are zero.
In a real receiver, the system temperature is increased by the quantum efficiency η of the mixer non-perfect heterodyning, background IF photons, losses in the spectrometer optics etc. (all combined in the factor α):

$$T_{Sys} = T_{QL} \cdot (1 + \alpha)$$

To experimentally determine the system temperature, usually the 'y-factor-method' is used. The signals from two loads are compared to their known temperatures:

$$y = \frac{S_{Hot}}{S_{Cold}}$$

$$T_{sys} = \frac{J_{Hot} - y \cdot J_{Cold}}{y - 1}$$

with: S_i = observed output signals and J_i = brightness Temperatures of the two loads. At 10 μm wavelength (T_{QL}= 1440 K) system temperatures of less than 2500 K were measured with THIS, only about 70% above the quantum limit [1].

Sensitivity

A comparison of direct and heterodyne detection methods is a difficult task, because many different parameters have to be taken into account and information given in the literature is usually not directly comparable as different definitions are used. Here I try to compare

the values of the noise equivalent power (NEP, which depends on the frequency resolution) and show an estimation of the behaviour of the signal-to-noise ratio (SNR) with varying resolution and wavelength as discussed in detail in [21]. Generally, heterodyne detection suffers severely from the quantum limit at high frequencies, while direct detection is more affected by increasing background noise at longer wavelengths. If the contribution of the background exceeds the quantum limit, heterodyne systems perform better than direct detection because of the higher coupling efficiencies. This is specially true if going to high resolutions where the throughput of direct detection instruments decreases. Frequency dilution effects even amplify the heterodyne advantage.

With the heterodyne system temperature one can calculate the NEP:

$$NEP = 2^{\frac{3}{2}} \cdot k_B \cdot T_{Sys} \cdot \sqrt{\frac{\delta_{Res}}{q}},$$

where $\delta_{Res} = \frac{1}{L_{max}} \int L(\nu) \cdot d\nu$ is the resolution bandwidth, q is the ratio of fluctuation and resolution bandwidth $q = \frac{B_{Fl}}{\delta_{Res}}$, $B_{Fl} = \frac{(\int L(\nu) \cdot d\nu)^2}{\int L^2(\nu) \cdot d\nu}$. $L(\nu)$ is the power transmission of the filter. q equals unity for a boxcar filter.
For example, the NEP for an ideal heterodyne receiver at 30 THZ is

$$NEP_{Ideal} = 7.9 \cdot 10^{-16} W/\sqrt{Hz}$$
$$NEP_{THIS} = 1.4 \cdot 10^{-15} W/\sqrt{Hz}$$

(with $q = 1.5, \lambda = 10$ μm $T_{Ideal} = T_{QL} = 1440K, T_{THIS} = 2500K$ and $\delta_{Res} = 300MHz$).

The NEP for TEXES (Texas Echelon Cross Echelle Spectrograph [22]) is given by:

$$NEP_{Texes} = 3.9 \cdot 10^{-16} W/\sqrt{Hz}$$

(for 1.5 m telescope radius, $\lambda = 10$ μm , 300 MHz resolution)
This corresponds to a noise temperature of $\sim$700 K, or 50% of the heterodyne quantum limit.

With such spectral resolution, the NEP of TEXES is lower by a factor of 3.5 meaning THIS needs 12 times the observing time to get

the same SNR. However, at a higher spectral resolution of 10 MHz the NEP of THIS reduces to $NEP_{THIS} = 2.5 \cdot 10^{-16} W/\sqrt{Hz}$, whereas TEXES is suffering from frequency dilution. At this resolution heterodyne spectroscopy is clearly advantageous to direct detection.

In order to achieve an illustrative comparison of the sensitivities of THIS and TEXES, [21] generated a plot showing the change of the signal to noise ratio with wavelength and frequency resolution, see Fig. 2.10. The plot is based on the best case sensitivity values found in the literature for TEXES [22] and THIS [23] which are interpolated to longer wavelengths. Plotted is the achievable SNR over observed wavelength for a given signal width in km/s (the frequency width of the smallest feature to be detected). It can be seen that the sensitivity of the heterodyne system rises with increasing wavelength due to the decrease of the quantum limit. Direct detection on the other hand shows a decreasing sensitivity towards longer wavelengths as the background contribution increases and the frequency dilution becomes more important. This is the explanation for the existence of a turnover point for every signal width where one technique becomes more advantageous than the other. The dotted line shows this border for TEXES and THIS. TEXES is more sensitive at short wavelengths and at lower resolution, whereas THIS is preferred at long wavelengths and at high spectral resolution.

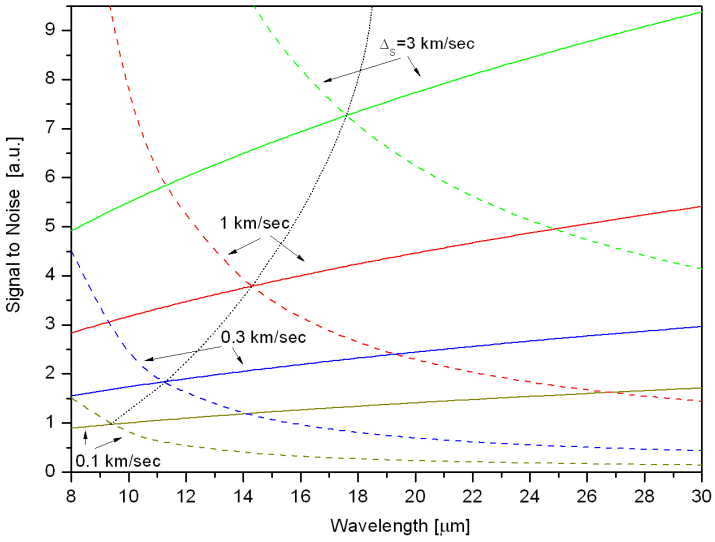

Figure 2.10: *Direct (dotted) vs heterodyne (solid) signal-to-noise ratios* for different signal widths.

Chapter 3

Venus Atmosphere

Venus, Earth's neighbour planet, is (apart from the moon) the brightest object in the night sky. It was targeted by Galileo Galilei's first telescope, and today it is again target of modern science being observed from the ground as well as from space with current and future orbiters like ESA's Venus Express and the Japanese orbiter Akatsuki.
The atmosphere of Venus consists of $\sim$96% CO_2 and $\sim$3% N_2, similar to Mars. In the very contrast to Mars, the density is extremely high, reaching 92 bar at the surface (Mars: $\sim$6 mbar). Venus also shows similarities to Earth as the diameter is comparable, but most features are drastically different. Its spin direction is contrary to the rotation around the sun, and it rotates extremely slow. In fact, one sidereal day is longer than a sidereal year, only the 'wrong' direction of rotation leads to a 'shorter' (166 Earth days) solar day. This very long exposure to the sun together with a greenhouse-heated CO_2 atmosphere leads to a completely different atmospheric picture compared to that of Earth.

Nevertheless, the physics is the same on every planet. Refined atmospheric models, developed from data collected by countless satellites and weather stations on Earth, able to predict the weather for some days and the climatic changes for decades, should in principle be applicable to all other planetary atmospheres, given that the different initial conditions like composition and solar flux are taken into account properly. In reverse, lessons learnt on the Venusian atmosphere can improve the understanding of climatological procedures

on Earth. Apart from scientific curiosity, this is the main motivation for observing planetary atmospheres. While refined global circulation models (GCMs) exist for Mars (extensively studied by numerous landers, orbiters and ground-based facilities) and Titan (the biggest moon of Saturn, possessing a dense atmosphere which is very 'earth-like'), models for the Venusian atmosphere were rather simple until the arrival of Venus Express, which relaunched the scientific interest in Venus and lead to many surprises and open questions.
Temperatures are a key parameter in the understanding of atmospheric structure, dynamics and composition. Strong temperature gradients due to the long solar exposure drive global patterns like the subsolar to antisolar stream in the upper atmosphere. Chemical processes are dependent on the temperature and changes of some 10 K can lead to fundamental changes in reaction chains.
In the following chapter, I will introduce shortly the current knowledge about Venus' atmosphere, summarise the main observation campaigns measuring mesospheric temperatures and will discuss the non-LTE emission of CO_2, which enables infrared heterodyne temperature measurements.

3.1 Venus Atmosphere: Models

The atmosphere of Venus is dominated by two fundamentally different regions. One region is the dense cloud layer in the troposphere from $\sim$40 km to $\sim$60 km altitude, covering the whole planet and rotating up to 60 times faster than the planet itself. This massive 'superrotation' is still not understood today. The other dominating dynamical feature is the sub-solar to anti-solar (SSAS) flow, located in the thermosphere above $\sim$140 km. It can be seen as a global anticyclone(SS)/cyclone(AS) system, driving a spherically symmetric wind from the subsolar point towards the antisolar point (see also Fig.3.1).
These two dynamical features of course have fundamental influence on the temperature field. In the troposphere, within the superrotation, the atmosphere is turbulent, well mixed and temperatures do not change between day and nightside. Due to the CO_2 atmosphere and the dense cloud layers, temperatures at the surface are greenhouse-driven and reach up to $\sim$ 750 K, and almost constantly cool down to about 230 K at the cloud tops at 60 km altitude.

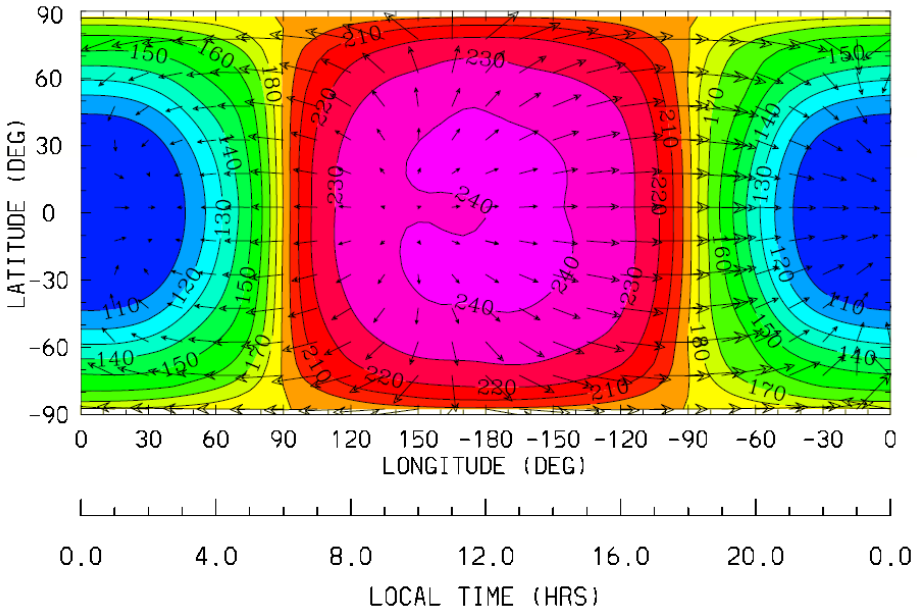

Figure 3.1: *Modelled thermospheric temperatures (colours) and subsequent subsolar to anti-solar flow (arrows) in 180 km altitude [24].*

In the SSAS dominated region, there are huge diurnal temperature differences up to $\sim$ 200 K[1]. At the dayside, there is an inversion and temperatures again reach more than 300 K at altitudes above 180 km. Vice versa, at night temperatures cool to $\sim$120 K. This diurnal difference starts to become significant above $\sim$100 km.
Infrared heterodyne spectroscopy is targeting the transition zone between superrotation and SSAS flow at around 115 km altitude. Of course, it is interesting to see how both regions interact and maybe how sharp the transition is, as this will be valuable information constraining evolving global circulation models.

Models of the atmosphere of Venus have been very simple until the arrival of Venus Express because of the lack of sufficient data. Since the first probes like Venera 1 (which was actually the first spacecraft reaching another planet) and Mariner 2 in 1961/62, Pioneer Venus was the only space mission dedicated to investigate the atmosphere of Venus. It consisted of several landers and the Pioneer Venus Orbiter (PVO) which stayed in orbit from 1978 until 1992. Together

[1]This was leading to the differentiation of the dayside 'thermosphere' and the nightside 'cryosphere'. For simplicity, and as all infrared heterodyne measurements are dayside only, I will describe altitudes higher than $\sim$120 km as 'thermosphere'.

with a series of Venera landers and orbiters it provided first detailed insight which resulted in the empirical 'Venus International Reference Atmosphere' (VIRA) model. Today, there are various attempts to update the VIRA model and also to derive complete global circulation models.

Venus International Reference Atmosphere (VIRA)

VIRA, published in 1985 [25] is based on data accumulated during the Pioneer-Venus mission and numerous Venera probes. After the historic first interplanetary probe Venera 1 (1961) the climax of these observations was in the late 1970s with the arrival of Pioneer-Venus 1 and 2. With data from orbiters and Landers the first detailed picture of another planet emerged. It was updated in 1997 (VIRA-2 [26], with further additions 2006 and 2007 [27, 28]) after the end of PVO and after more data was acquired e.g. from the Magellan, Galileo, Venera and VEGA missions.

The observed data and an averaged temperature profile [29] can be seen in Fig. 3.2. In the altitude region important for this thesis, there is only very few data from all VIRA contributing instruments. With three descent probes, one at the day side, one at the night side (both in mid- latitudes) and one in the north polar region, conclusions to the general atmosphere can only be drawn if the atmosphere is globally stable and homogeneous. This is already challenged by the high variability of the measured temperatures during the descent of the day side probe above 110 km.

Resulting from this lack of data, the spatial resolution is rather broad with a latitudinal separation of up to 30 degrees. It therefore can only be handled as a very averaged global model which ignores possible local or temporal variations. Since the first view of the upper atmosphere described it as rather static and uniform, VIRA was a suitable model in the beginning, but today more and more deviations are observed (see section 3.2 below). However, despite its known problems, VIRA is still the most used reference for atmospheric temperatures.

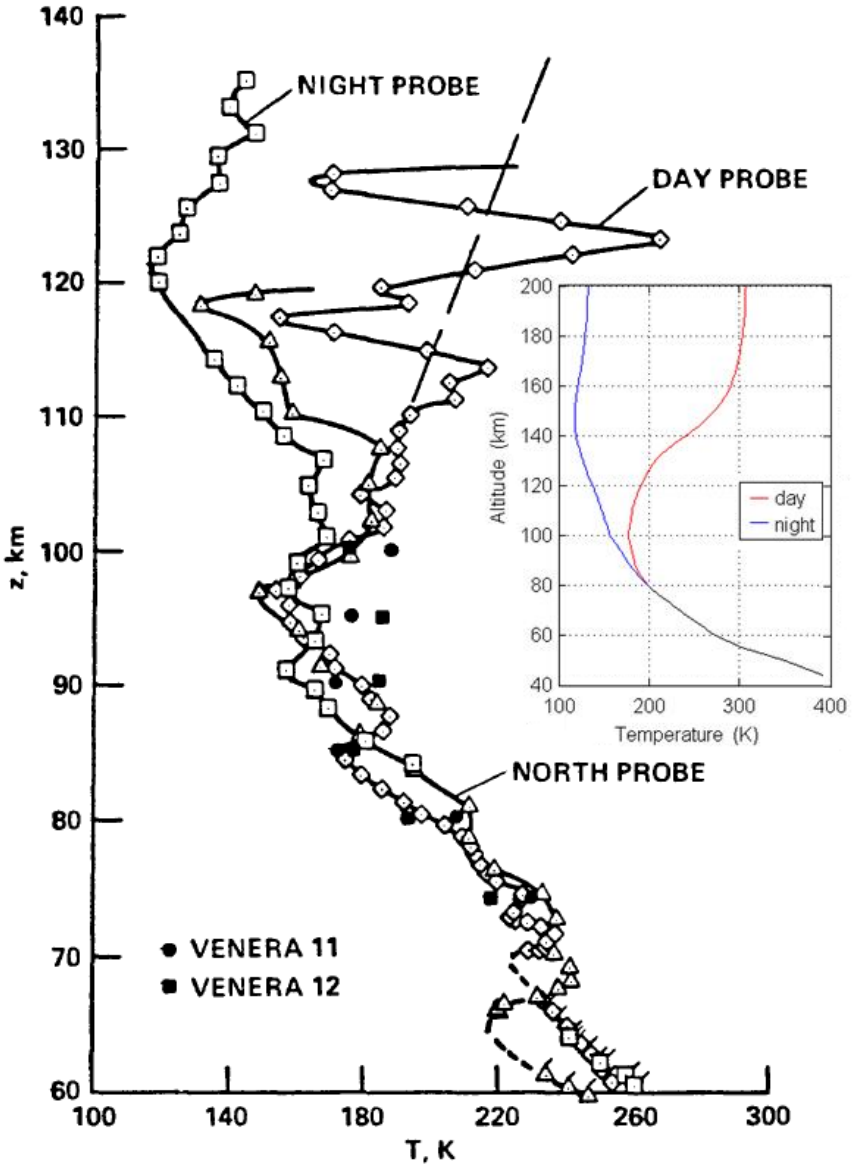

Figure 3.2: *Temperature Profiles taken with Pioneer Venus and Venera probes [25]. As indicated, Pioneer Venus 2 deployed three probes into the Venusian atmosphere, one on the day side one on the night side and one in the north polar region. The inset shows the averaged VIRA model [29], which clearly under-represents the dayside variations seen above 110 km.*

Modern global circulation models (GCM)

Recently, there are many attempts to create a more realistic model for the atmosphere of Venus. However, they all are either still in an early phase of evolution or restricted to distinct atmospheric regions. For example the Venus Thermosphere GCM by Bougher et al.(VTGCM [30, 31]) was developed from Earth GCMs [32]. It models nicely the SS-AS flow but is restricted to altitudes higher than 100 km. For the middle atmosphere (30-90 km altitude) there is a lot of data from Venus Express. To couple this observationally good covered region to the thermosphere is the goal of the model developed at the Imperial College by Mueller-Wodarg and coworkers. They are trying to adapt a model of Titan's atmosphere [33] to Venus. Titan has a more 'earth-like' atmosphere, which makes it easier to predict using well-proven models of the Earth's atmosphere. Assuming boundary conditions for the cloud tops and the high thermosphere, this model is targeted at the mesosphere of Venus with a quite empirical approach, trying to incorporate results of observations as soon as possible.

In contrast, Lebonnois et al. ([34]) is starting from an analytical point of view, at first trying to reproduce the very basic attributes of Venus atmosphere like the superrotation from basic physical considerations and only in a second step to adapt the model to specific observations.

3.2 Ground-based Observations

Despite the increasing interest in Venus and its atmosphere since the arrival of Venus Express, temperature measurements in the mesosphere are still insufficient. The temperatures presented in this thesis are the only ones at the day side of Venus probing the upper mesosphere with an adequate spatial resolution. In this chapter I will summarise other measurements in the vicinity and discuss their comparability to the infrared heterodyne results.

Ground based observations are mostly done using sub-mm observations of CO. I will here present measurements by Clancy et al. and Rengel et al., as they will be later compared to infrared heterodyne measurements. Other methods include observations of airglow emission of molecular oxygen at 1.3 μm , but as they are pure

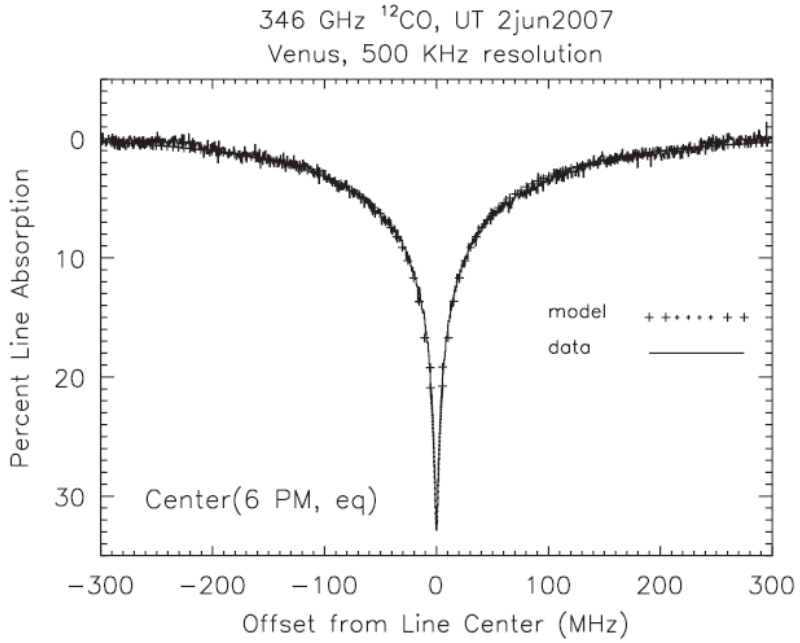

Figure 3.3: *Observed ^{12}CO absorption line at 346 GHz (J=2 $\mapsto$ 3), from Clancy et al. [35]. From fits to the line shape, temperature profiles can be modelled.*

nightside observations they are mentioned here more to get a general idea about temperature measurements in the upper atmosphere of Venus.

3.2.1 Sub-mm

Sub-mm measurements of CO absorption lines (see Fig. 3.3) of various isotopes and at different rotational transitions provide temperature profiles from 75–110 km altitude. Fig. 3.4 shows the diurnal temperature difference which is clearly visible in the line centre. While the cold night side produces an enhanced dip, on day side observations even a little (LTE) emission is visible.
To derive the temperature profile from the measured line-shape, one has to include the CO mixing profile and an a-priori temperature profile as a starting point for fit algorithms. CO mixing profiles can be retrieved from simultaneously fitting different spectra constraining different altitude ranges (e.g. ^{12}CO and ^{13}CO, [35]). As a-priori temperature profile, usually the VIRA model is used [36]. When

fitting the temperature profile, constant atmospheric spheres are assumed [36].

A major drawback of ground based sub-mm observations of planetary atmospheres is the low spatial resolution due to the big field of view. Using the James Clerk Maxwell Telescope (JCMT, Mauna Kea, Hawaii, 15 m dish) and a CO transition line at 346 GHz, the resulting FWHM of the antenna beam is 14 arc-seconds (valid for most Clancy et al. observations). This is more than 8 times larger than THIS at the McMath-Pierce Solar Telescope (FOV: 1.7 arc-seconds) or even 16 times larger than THIS or HIPWAC at the IRTF (FOV: 0.85 arc-seconds) . As an example, at Venus's maximum elongation ($\sim$50% illumination) the sub-mm beam fills the whole day side, whereas infrared heterodyne can do many independent measurements all over the illuminated disk.
This has also to be taken into account when thinking about the sub-mm temperature profile modelling, assuming constant spheres. Resolving large fraction of a planetary disc, this can be only an approximation.
Summarising, sub-mm observations of CO are a nice tool to obtain mesospheric temperature profiles at both, day and nightside of a planet, but they lack spatial resolution which prevents detailed information which can be provided by infrared heterodyne spectroscopy (at the dayside and at the emission altitude).

Clancy et al.
One of the most thorough ground based studies of upper atmospheric temperatures has been done by Clancy et al. using mm (1982, '85, '86, '88, and '90 using the Kitt Peak NRAO–12 m millimeter observatory) and sub-mm (1999, 2000, '01, '02, '07 and '09 using the JCMT) observations of carbon monoxide (CO). Observations were carried out from the mid eighties until today. Being able to observe both,day and night sides of Venus and probing altitudes from 75 to 100 km, these are valuable data to compare to infrared heterodyne measurements. Temperatures observed tend to be higher than expected from VIRA, detailed profiles are discussed in chapter 4.

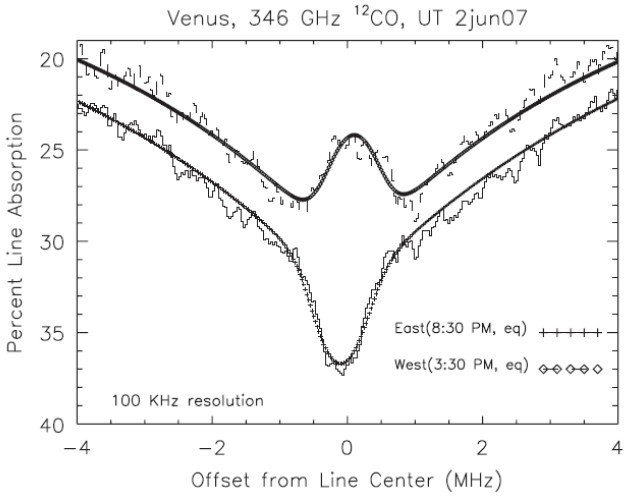

Figure 3.4: *Centres of the line displayed in Fig. 3.3, for both day (West) and night side (East). Big diurnal temperature variations are evident (night side dip vs. day side emission) as well as different wind induced Doppler shifts.*

Rengel et al.

Rengel et al. [36, 37] observed also CO but J=2 $\mapsto$ 1 transitions at 220 and 230 GHz. Using the 10 m Heinrich Hertz Submillimeter Telescope (HHSMT, Mt. Graham, Arizona) their FOV was $\sim$33 arc-seconds with the apparent diameter of Venus of 24 arc-seconds during the observations. The observed temperatures in principle agree with VIRA data, but do show big variability (see Fig. 3.5). Taken within 24 hours, 3 out of 4 observations agree within the error bars. One observation (red, Fig. 3.5) shows significant deviations. These variations partly might originate from pointing errors as some nighttime features of the thermal profile appear also in this daytime measurements. The warm layer at 105 km altitude is seen very prominently in every nighttime profile. Also the inversion layer at 70 km is seen in other nighttime profiles. However, using the above mentioned beam sizes, they had to point off the planet anyway to receive only the signal from the selected hemisphere. Usual pointing errors in the order of an arc-second should be negligible. This would be another indication for a high intrinsic variability of the Venus atmosphere.

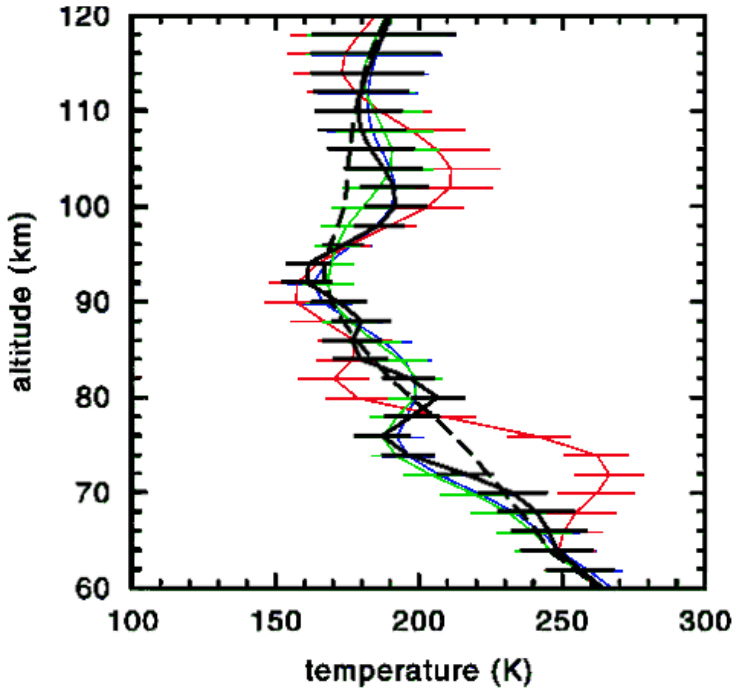

Figure 3.5: *Superposition of four dayside observations of $^{12}CO(J=2 \mapsto 1)$ at 230 GHz from [37]. Dashed line: VIRA profile. Temperature variations reach up to 50 K within 24 hours.*

3.2.2 Air-glow Measurements

Air-glow emission is the result of recombination of oxygen atoms which are formed by photo-dissociation of CO_2 molecules on the day side of Venus. These atoms are carried by the SSAS flow to the night side, descend to higher density regions, recombine producing excited O_2 which then emits the air-glow photons. Temperatures can be retrieved by fitting the rotational temperature to the relative strengths of individual lines of the emitting band [38]. Observations were taken at the Anglo-Australian Telescope using an infrared imager and spectrograph at 1.3 μm wavelength and with a spectral resolution of 2400 ($\lambda/\delta\lambda$). Results show mean temperatures of around 190 $\pm$ 10 K in agreement to earlier measurements [39, 40]. These temperatures are significantly higher (15-30 K) than those expected from VIRA see Fig. 3.6. The altitude of the air-glow emission can be constrained by chemical model predictions to 90-100 km, validated

by Venus Express data described in the following section.

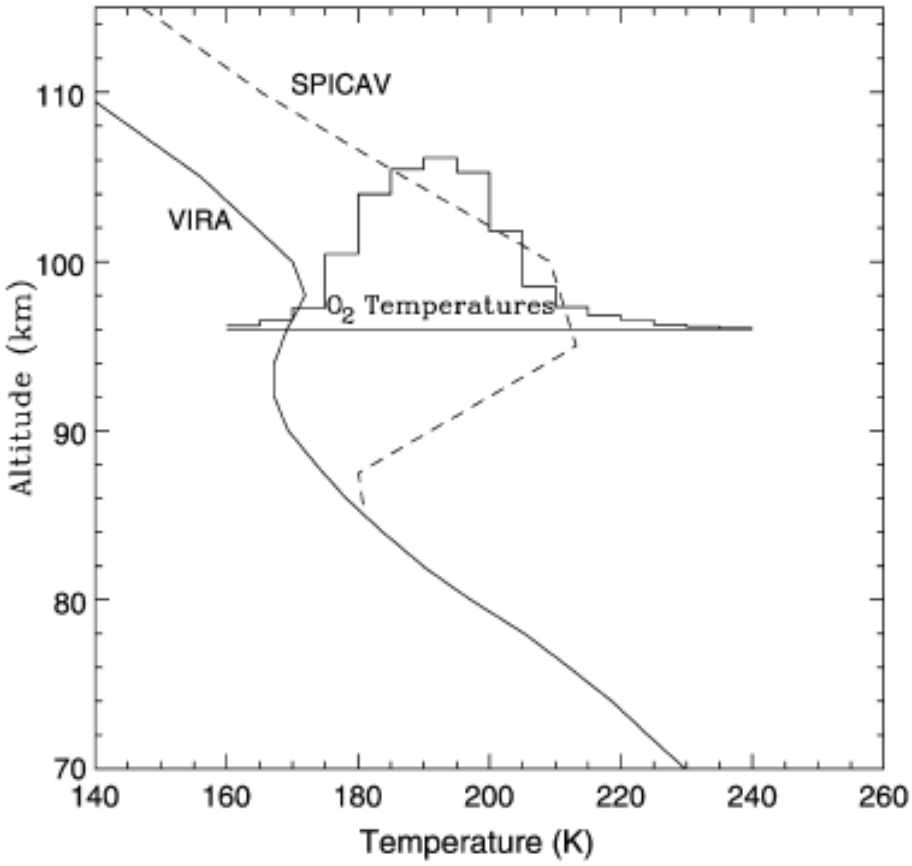

Figure 3.6: *Nighttime temperatures from O_2 airglow measurements [38]. The histogram of the observed temperatures is plotted at an altitude of 96 km where the emission is thought to originate. It shows the distribution of temperature values retrieved during 6 observing nights. The data is compared to the VIRA model and SPICAV observations (see chapter 3.3). The dashed line represents the average of the six orbits shown in Fig. 3.8*

3.3 Observations from Space

The main target of the Venus Express mission is to investigate the atmospheric properties of our neighbour planet. Six out of seven instruments are dedicated to atmospheric research. Unfortunately, the instrument which should target, among others, the temperature distribution in the mesosphere, PFS (Planetary Fourier Spectrometer), can not receive any data as a mirror is stuck in the 'calibration' position and can not be targeted at Venus. However, there is still plenty of data of temperature measurements, and I will show results of the other - working - instruments.

VIRTIS

The Visible and Infrared Thermal Imaging Spectrometer (VIRTIS) was designed to observe the lower atmosphere from the ground up to 40 km from UV to near infrared wavelengths. Due to the PFS failure, VIRTIS covered also targets in the higher atmosphere. It observed the O_2 air-glow in limb viewing geometry, thus constraining the altitude of the emission to 96 ± 1 km. VIRTIS also observed CO_2 non-LTE emission at 4.3 μm peaked at 115 km altitude with a solar zenith angle (SZA) dependence of $\sim$10 km from noon to sunset, confirming the previously described non-LTE emission modelling [41, 42, 43].
Temperature measurements by VIRTIS target altitudes from 65-95 km. Observing between 1 and 5 μm , the radiance between 3.8 and 5 μm at nighttime is dominated by thermal emission and absorption by the clouds and the CO_2. By observing lines with different opacity, VIRTIS can retrieve the CO_2 mixing and temperature profiles. Daytime retrieval of temperature profiles was not successful until now, as reflected solar radiation requires careful modelling to extract the spectral information properly.
Two VIRTIS night-time temperature maps are displayed in Fig. 3.7. The time interval between the two observations is 3 hours. This nicely demonstrates the variability on short timescales of the atmospheric temperature structure. Variations up to 20 K at the 1 mbar (approx. 85 km altitude) pressure level can be seen.
Temperatures are in general agreement with the VIRA model, except a warmer layer at the upper boundary above the pole. Whether this can be related to the polar vortex or just to instrumental or observational constraints is not evident.

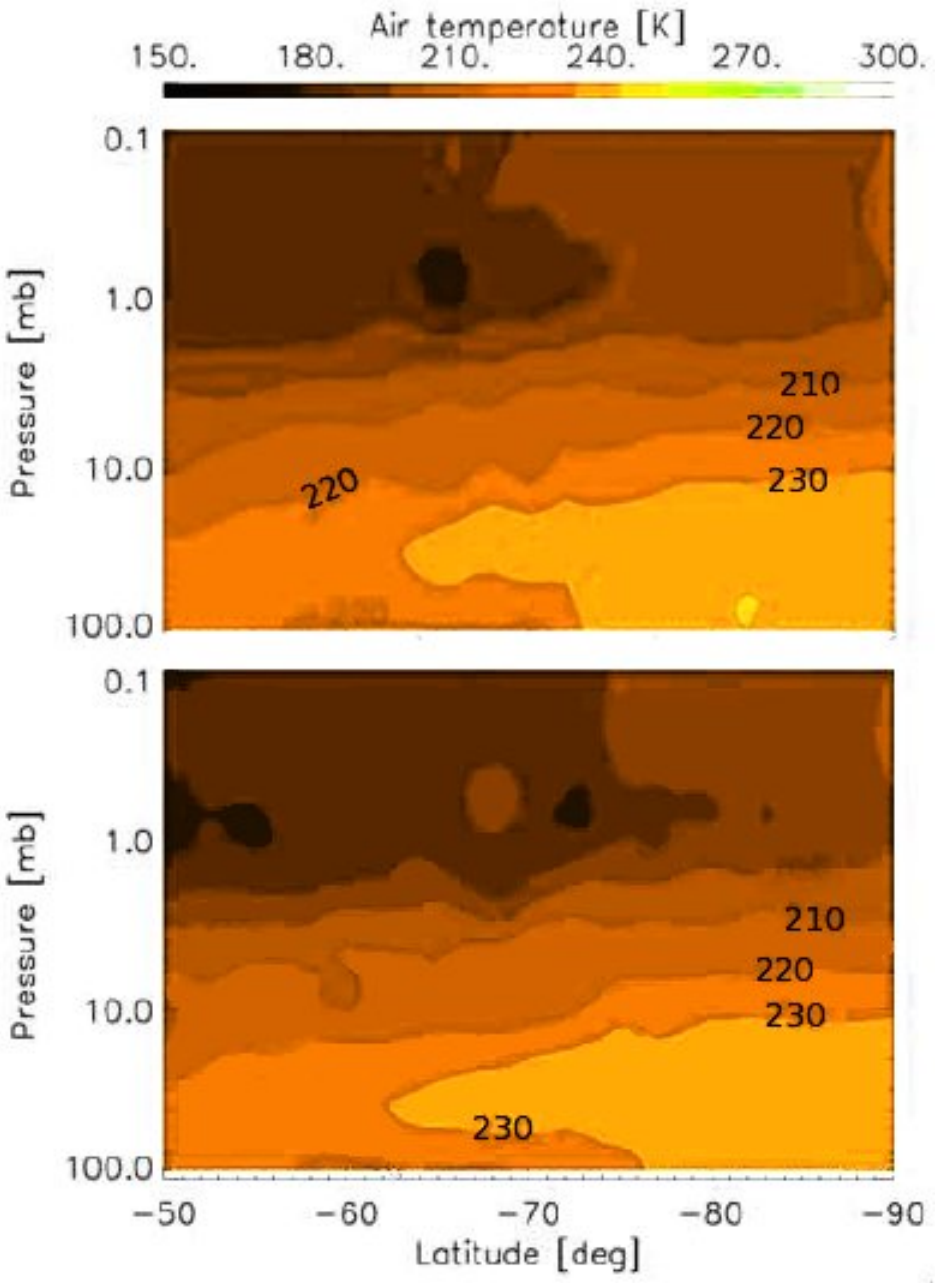

Figure 3.7: *Examples of night-time temperature maps observed with VIRTIS [44] between 65 and 95 km altitude. Time between both measurements: 3 hours. Variability at the 1 mbar level: ∼ 20 K.*

SPICAV

The SPICAV/SOIR (Spectroscopy for Investigation of Characteristics of the Atmosphere of Venus [two channels: one in the UV, the other in the near infrared] / Solar Occultation at Infrared [2-4 μm]) instrument of Venus Express was designed to look for atmospheric trace gases like water or molecular oxygen and to determine the density and temperature of the atmosphere at 80-180 km altitude. The temperatures showed in Fig. 3.8 were observed using solar and stellar occultation, which again restricts the observations to the nightside (stellar) and the terminator (solar occultation) [45]. Spectra of a star unaffected from atmospheric influences taken at high altitudes are compared to spectra with the star being more and more absorbed by the atmosphere. With a given CO_2 absorption cross section on the temperature, an a priori temperature profile (VIRA) and assuming hydrostatic equilibrium, atmospheric density, the scale height and the temperature profile can be fitted to the data.
Fig. 3.8 shows temperatures higher than the VIRA prediction including a warm layer at 100 km. The big temperature variations during the different orbits (up to 50 K at 100 km altitude) correlate to the different solar zenith angles. But, at comparable SZA positions the variation is still around 20 K within only two Earth days (Venus-Express is on a 24-h orbit around Venus). This warm layer has not been seen for example by many sub-mm nighttime observations by Clancy et al. which is still matter of debate. It is possible that this is a short term feature, which will be investigated by upcoming VEX observations. If this is the case, the view of the atmosphere would change to a far more complex, probably more convective and turbulent picture. It is not possible to explain the differences between SPICAV and sub-mm observations with differences in beam size as SPICAV is seeing the warm layer from near-terminator-areas (SZA $\sim$100 deg) all the way until the anti solar point (SZA = 180 deg).

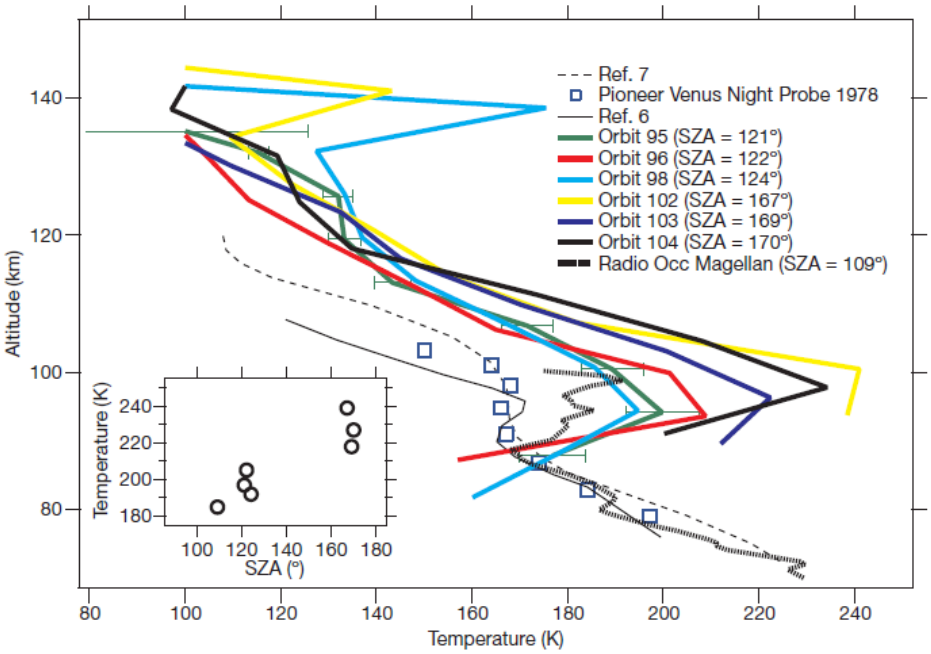

Figure 3.8: *Temperatures retrieved from UV stellar occultations observed with SPICAV [45]. Shown are six temperature profiles retrieved from different orbits (1 orbit ≙ 24 hours) correlated to the solar zenith angles. However, still a big variation of 20 K is seen at similar positions within 2 days. Generally, observed temperatures are higher than those of VIRA and previous sub-mm observations (References 6 and 7 are [46] and [47] respectively).*

Venus Express Radio Science experiment (VeRa)

VeRa is investigating the structure of the Venusian atmosphere at altitudes from 40-90 km. From radio occultation measurements profiles of temperature and pressure versus height can be derived [48, 49]. It targets the transition zone from the upper cloud deck to the mesosphere. For VeRa, the occultation takes place when Venus Express is disappearing behind Venus, as seen from Earth. Signal frequency perturbations in the radio link from VEX to earth can be attributed to diffraction in the Venusian atmosphere, as the initial oscillator frequency is very well known. Thus, a refractivity profile can be retrieved which yields a vertical neutral number density distribution which can be used to calculate the temperatures. For the transition to the upper mesosphere there are different upper boundary conditions assumed at 100 km altitude, as seen in Fig. 3.9. They all merge into the same profile at $\sim$ 90 km. VeRa is seeing roughly the same temperatures as predicted by VIRA [49].

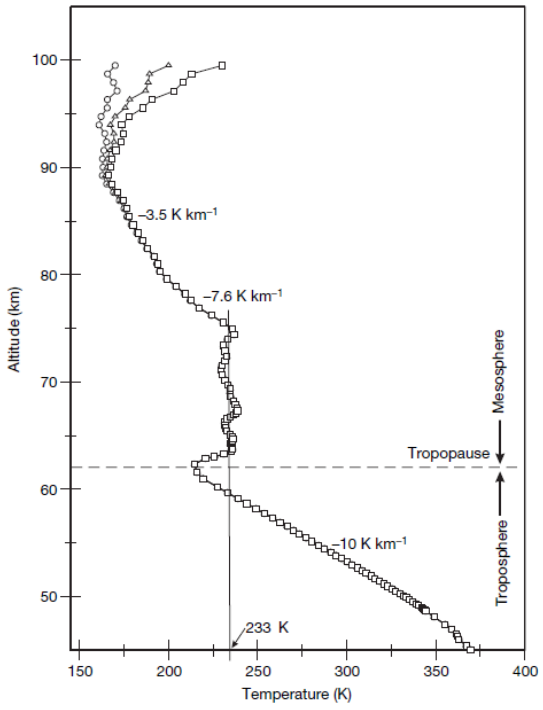

Figure 3.9: *Temperature profile measured by VeRa [48].*

3.4 Non-LTE Emission

Non - local thermodynamic equilibrium (non-LTE) emission is the key to planetary atmospheres for infrared heterodyne spectroscopy. This radiation is locally confined to a narrow altitude region within Venus's atmosphere at pressure levels around $5 \cdot 10^{-3}$ mbar which corresponds roughly to 115 km. Observing the emission line with high spectral resolution enables the deduction of temperatures from its width and winds from its Doppler shift.
Non-LTE emission actually was detected first by infrared heterodyne spectroscopy in 1976 by Betz et al. [50]. The explanation of this phenomenon was soon given by Mumma et al. [51, 52]. Refined models including the radiative transfer process of whole CO_2 bands were developed later [42, 53, 43]. It is important to note that the non-LTE refers to the emission process, caused by vibrational excitation of the CO_2 molecules. As the kinetic properties of CO_2 are assumed to be thermalised to its environment [54] one can expect the kinetic and rotational temperatures to be equal and to represent the physical temperature of the neutral atmosphere at the emitting altitude. This is the reason why temperature retrieval is possible by the determination of the kinetic or rotational temperature as it is done in this work. The Mechanism of the non-LTE emission is the following:
Below a pressure level of $\sim$ 0.15 Pa ($1.5 \cdot 10^{-3}$ mbar), the probability of spontaneous emission for the excited CO_2 molecules gets higher than that of collisions. Absorption of sunlight at 4.3 and 2.7 μm , followed by collisional and radiative relaxation, creates a population inversion between two vibrational levels of the 10-μm band (among others). This is shown in Fig. 3.10 for the atmosphere of Mars, but the same conclusion applies Venus, where processes are similar with the biggest difference being the altitude of the respective pressure levels.
In that altitude region where pressure conditions are appropriate, radiative emission becomes the favoured channel of de-excitation, creating what was described as a natural laser [55]. In fact, however, the majority of the observed emission originates from altitudes below the population inversion. It is therefore an emission mimicking higher (vibrational) temperatures, but with negligible stimulated ('laser') emission, hence non-LTE.
Below 10^{-4} mbar the density gets too low, and non-LTE emission gets negligible [43]. Due to this restriction, the emission originates in a well defined pressure layer between $1.5 \cdot 10^{-3}$ and 10^{-4} mbar. This corresponds to an emission altitude of 110-120 km. The retrieval of

this altitude is shown in Fig. 3.12: for a given altitude the radiance of the whole atmosphere below is calculated. The result is shown in the left panel. The derivative of the radiance vs. altitude function (shown on the right) gives the weighting function of the non-LTE emission. It peaks around 115 km altitude. Changes in illumination (solar zenith angle) at different positions on Venus are not expected to give rise to significant changes of the emission altitude.
However, to determine the exact altitude, a standard (VIRA) pressure temperature profile of the atmosphere is assumed. As the observed temperatures are higher than predicted by VIRA, altitudes might vary as the 0.15 Pa pressure region might shift in altitude. Still, the theoretical values are in agreement to observations using VIRTIS on Venus Express observing non-LTE emission at 4.3 μm [56]. As seen in Fig. 3.11, the measured radiance, observed in limb sounding mode, confirms an altitude of $\sim$120 km for the 4.3 μm non-LTE emission.
Also, observations of the Thermal Emission Spectrometer (TES) on Mars Global Surveyor [57] confirm the respective model predictions. Of course, with Mars, the model atmosphere is much more refined and tested. There, the model predicts an emission altitude of $\sim$80 km.
Recently, first attempts to model observations of 10 μm non-LTE emission on Mars with THIS [58] were successfully performed, further supporting the validity of the model [43].

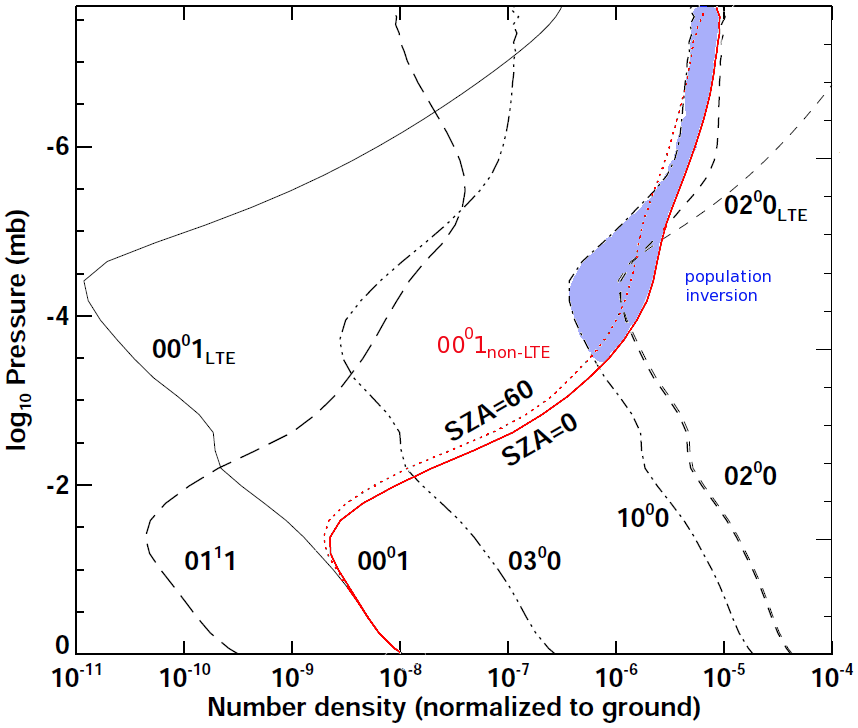

Figure 3.10: *Non-LTE populations of five different CO_2 vibrational levels, as indicated, in the atmosphere of Mars [43] (similar for Venus) for SZA=0. At pressure levels of 0.1 mbar the 00^01 state departs from its LTE case. Due to strong solar pumping it reaches higher levels than the lower 10.4 μm transition state 10^00. For this reason, this emission is called a "natural laser".*

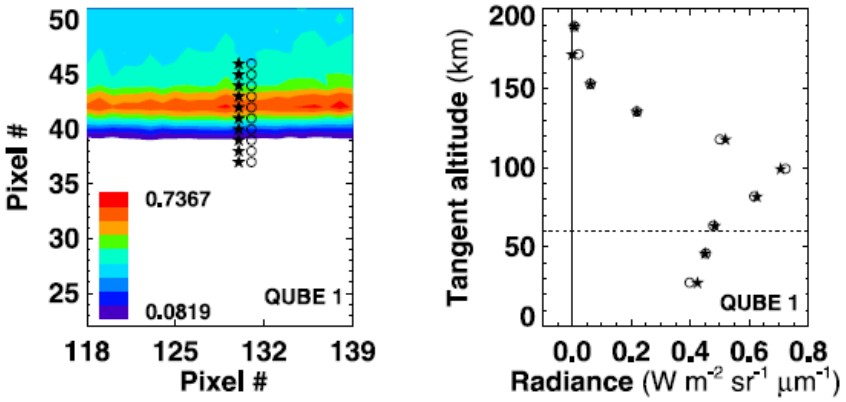

Figure 3.11: *VIRTIS limb sounding of non-LTE CO_2 emission at 4.3 µm [56]. The retrieved altitude of ~120 km confirms non-LTE modelling by Lopez-Valverde et al. [42, 53, 43].*

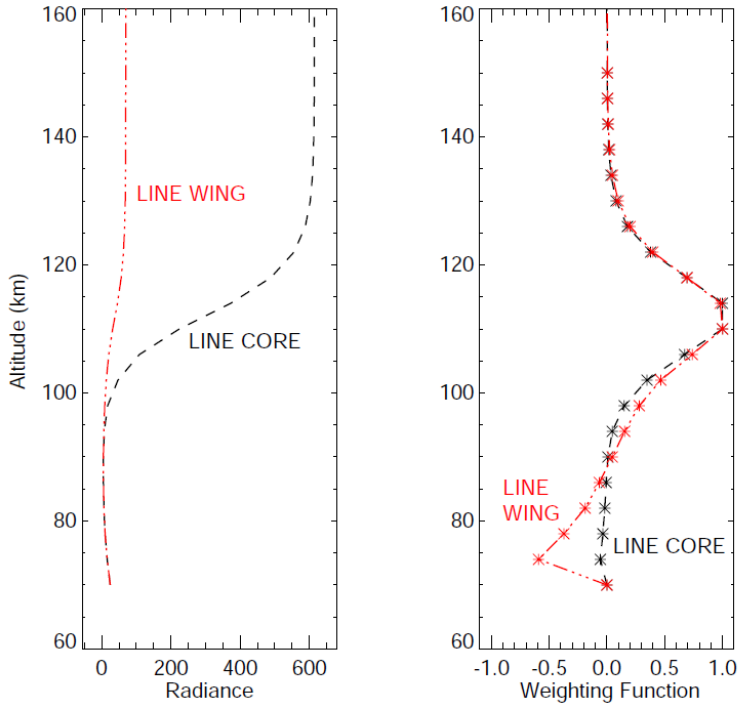

Figure 3.12: *Left panel: radiance profile obtained for line wing and line core (separated by 0.0015 cm-1, [43]). Right panel: altitude derivatives of the radiance function for the two positions can be regarded as weighting function [43].*

Chapter 4

Observations

Observations of Venusian upper mesospheric temperatures were done during this work with the two infrared heterodyne instruments HIPWAC and THIS. HIPWAC was used in October 2007 on the NASA Infrared Telescope Facility (IRTF, Mauna Kea, Hawaii), THIS was operated at the McMath Pierce Solar Telescope at Kitt Peak Observatory (Arizona, USA) during three observing runs in 2009. Within one observation in 2009 it was possible to compare the data with simultaneously observed radio/submm data. Additionally, we got old data for re-analysis, taken with IRHS in 1990/91 (IRTF). In this chapter, I will present the observing procedures, data reduction and analysis and finally compare the results of the three different infrared heterodyne spectrometers as well as the IRHet results with other observations and models.

Some observing procedures are the same for all infrared heterodyne spectrometers and are explained in the following.

Infrared Heterodyne Observing Technique

Observations with all instruments were taken either at the McMath-Pierce Solar Telescope (Kitt Peak Observatory, Arizona, USA) or at the NASA Infrared Telescope Facility (IRTF, Mauna Kea, Hawaii, USA). Infrared heterodyne instruments have a field of view (FOV) of the telescope's diffraction limit [20]. At 10 μm wavelength, the FOV is 1.7 ″ at the McMath-Pierce Telescope and 0.9 ″ at the IRTF. The pointing uncertainty at all telescopes was estimated to be usually 1

FOV beam size, with some exceptions up to 2 times the FOV at the McMath, where telescope tracking is getting difficult due to technical telescope problems sometimes. Seeing conditions were normally varying from 1 to 2 arc-seconds.

Radiation from the telescope is split by a dichroic mirror, coupling the infrared radiation into the spectrometer and feeding the visible light into an integrated optical guide system. The image of the optical camera can be superimposed to a transparency template (IRHS) or to an electronic image of Venus (HIPWAC, THIS). This provides accurate pointing information and allows active telescope tracking by keeping the image within the given template. Spectra were taken both ON and OFF Venus (i.e. source vs. sky background) using two instrumental beam paths, A and B. The observation is divided into repeated 'cycles' of source, background, hot and cold calibration loads. With THIS, a gas cell is additionally observed for an exact frequency reference. The integration time of each target is calculated to an optimal signal-to-noise ratio. (For example, the observation of the hot load blackbody can be very short due to its high signal, whereas the sky source usually was observed as long as possible.)
The spectrum can then be calculated as:

$$Spectrum_{cal} = \frac{Sig - Ref}{Hot - Cold} \cdot (B_{Hot} - B_{Cold})$$

with B_{Hot}, B_{Cold} being the known brightness temperatures of the hot and cold load, which are used here for calibration. The spectrum is then the brightness temperature difference between signal and reference including all instrumental losses. In addition, to eliminate any unwanted signal like standing waves originating in the spectrometer the source was alternated between the A and B beams. The observed emission line will thus switch its sign (appearing like an absorption in the spectrum), whereas the standing wave will not be altered. Subtracting A-B then minimises such systematical errors, a technique known in radio astronomy as "double beamswitch". For more details of infrared heterodyne observing strategies, see [1, 59, 20].

To minimise line broadening due to the changes of Earth rotation and radial Venus-Earth velocities, individual spectra were shifted appropriately before co-adding. However, to reduce any broadening caused by a frequency-drifting or -fluctuating LO as much as possible, single spectra (or packages of a few, depending on the SNR) were fitted separately. The temperature was then retrieved as the mean values of all single spectra from one measurement.

The observed lines can be fitted assuming Gaussian line shapes as the pressure at the emitting altitude is sufficiently low to neglect any pressure broadening, which would result in a more Lorentzian like line shape. Physical temperatures of the atmosphere are assumed to be equal to both, kinetic and rotational temperatures of the emitting CO_2. This can be expected as, although the emission originates from an non-LTE (local thermodynamical equilibrium) effect, the translation and rotation of CO_2 is supposed to be thermalised to its environment (see [54] and section 3.4).

The temperature can then be retrieved using the Doppler-equation

$$\Delta\nu_{\mathrm{D}} = \frac{\nu_0}{c}\sqrt{\frac{8k_B T_{kin}\ln(2)}{m}}, \tag{4.1}$$

relating the observed Doppler widths $\Delta\nu_{\mathrm{D}}$ (FWHM) to the temperature T_{kin} for a molecule with the mass m at the observed frequency ν_0 [60].

Few measured spectra consist of a broad shallow absorption feature in addition to the narrow intense non-LTE emission core. This was sometimes the case for measurements taken directly at the terminator and in the vicinity of the poles. The absorption features were then fitted with a LTE radiative transfer model using the Codat/BEAMINT software [61]. The effect of the underlying broad absorption on the emission features was thus eliminated by the radiative transfer model and the emission lines where subsequently fitted using a Gaussian line profile, as the non-LTE modelling is not yet implemented in the code. The absorption only slightly affects the measured line shapes and retrieved temperatures. The modelling was based on the VIRA temperature/pressure profiles. All fits were performed under the assumption of negligible stimulated emission.

Influences of telluric absorption on the lines were modelled using the atmospheric transmission code GENLN2 [62] and removed, including effects due to changes with air-mass. Due to the high atmospheric transmission in the observed wavelength range the mentioned effects are less than 10 $\%$ for all observed spectra.

4.1 THIS @ McMath

Three observing runs with THIS were scheduled in 2009 to observe temperatures, two symmetrically around inferior conjunction (March and June) and one campaign at maximum western elongation (June).

March 2009

Venus was observed between March 17^{th}-22^{nd}. The angular diameter of Venus varied from 54-56 arc-seconds. The Earth-Venus topocentric Doppler shift varied between -6 and -2.5 km/s (approaching).

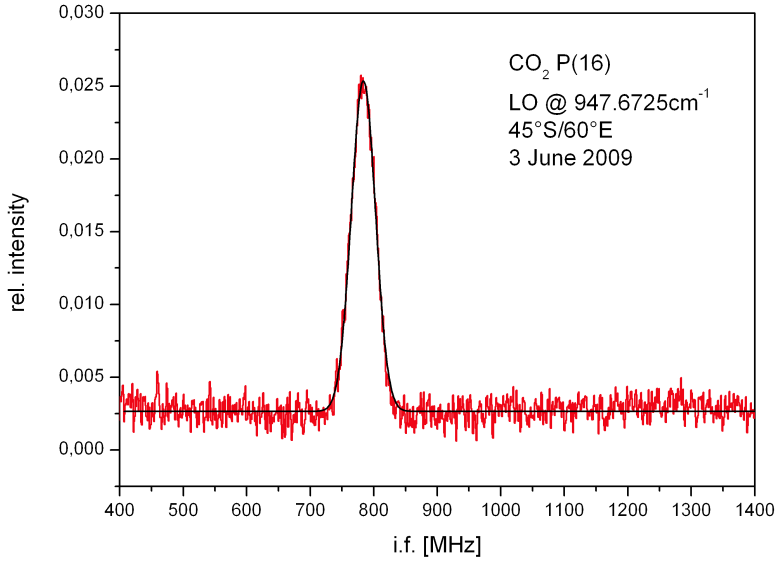

Figure 4.1: *Typical spectrum of a THIS observation (red) with fitted Gaussian profile (black). The spectral resolution is 1 MHz.*

Fig. 4.1 shows a typical spectrum of the observed P(16) line of the 10.6 μm band of CO_2. The spectrum was observed on June 3rd 2009 at 45 degrees South and 60 degrees East of CML. The integration

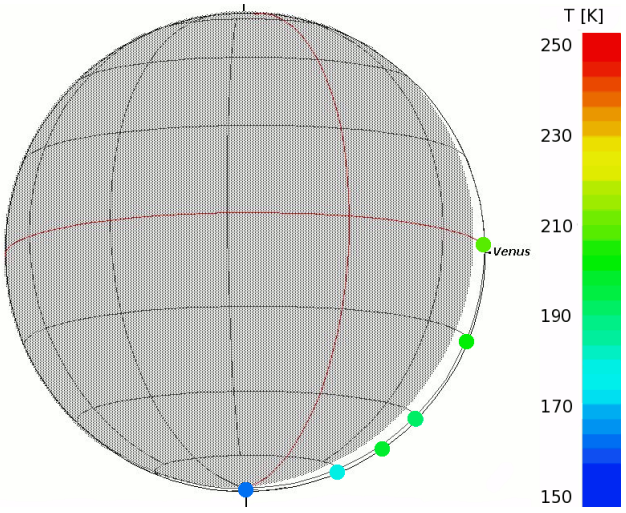

Figure 4.2: *March 2009 Observations. Only the thin evening crescent was illuminated. Point size indicates the FOV on the Venusian disc. Colours show the mean values of all measurements at one position.*

time for a single fitted line was between 8 and 32 minutes depending on the signal strength. From the Gaussian fit to the line in Fig. 4.1 a linewidth of 44.75 MHz was determined. This corresponds to a temperature of 214 K using the Doppler-equation 4.1. The fitting errors for the individual lines are $\sim$3–20 K (1-σ) depending on the intensity (and thus the signal-to-noise ratio) of the emission feature.

Due to weather and technical problems we only observed the southern hemisphere in March. The observational geometry was such that the southern hemisphere was more illuminated than the northern and tilted towards Earth, thus no positions on the northern hemisphere above 67° northern latitude were observable. The observed positions are shown in Fig. 4.2, where the size of the circles represent the actual telescope FOV on the Venusian disc and the temperature is indicated by the colour code.

All retrieved temperature values are given in Table 4.1. The retrieved values range from 160 K at the South pole increasing up to 220 K at the equator.

DATE	UT	LAT	T [K]	ERR		DATE	UT	LAT	T [K]	ERR
20.03	23:40	-45	198	9		21.03	22:30	0	218	26
21.03	0:10	-90	161	17		21.03	22:50	-25	188	11
21.03	16:10	-45	209	7		21.03	23:00	-67	183	10
21.03	16:30	0	212	12		21.03	23:30	-47	169	16
21.03	16:40	-67	212	10		22.03	16:30	-45	199	11
21.03	20:40	0	210	15		22.03	17:10	0	193	19
21.03	21:00	-25	209	9		22.03	20:10	-56	198	9
21.03	21:30	-67	184	9		22.03	20:40	-67	173	10
21.03	21:40	-47	191	9		22.03	22:30	-65	195	14
21.03	22:00	-90	168	13		22.03	23:10	-47	191	14

Table 4.1: Retrieved temperature values in March 2009.

April 2009

After inferior conjunction we observed Venus between April 2^{nd}-6^{th}. The angular diameter of Venus again varied from 54-56 arc-seconds. The Earth-Venus topocentric Doppler shift varied between +2.5 and +6 km/s (receding).

The two campaigns in March and April were scheduled symmetrically around inferior conjunction (March 27^{th}) to investigate possible asymmetries of the temperature distribution between the morning and evening limb.

All retrieved temperature values are given in Table 4.1, the mean temperature values for each position are shown in Fig. 4.3.

The retrieved values range from 165 K at both tips of the morning crescent at the South pole and at 45° north, increasing up to nearly 240 K at 11° south. A clear dependence on the solar zenith angle (SZA) can be seen.

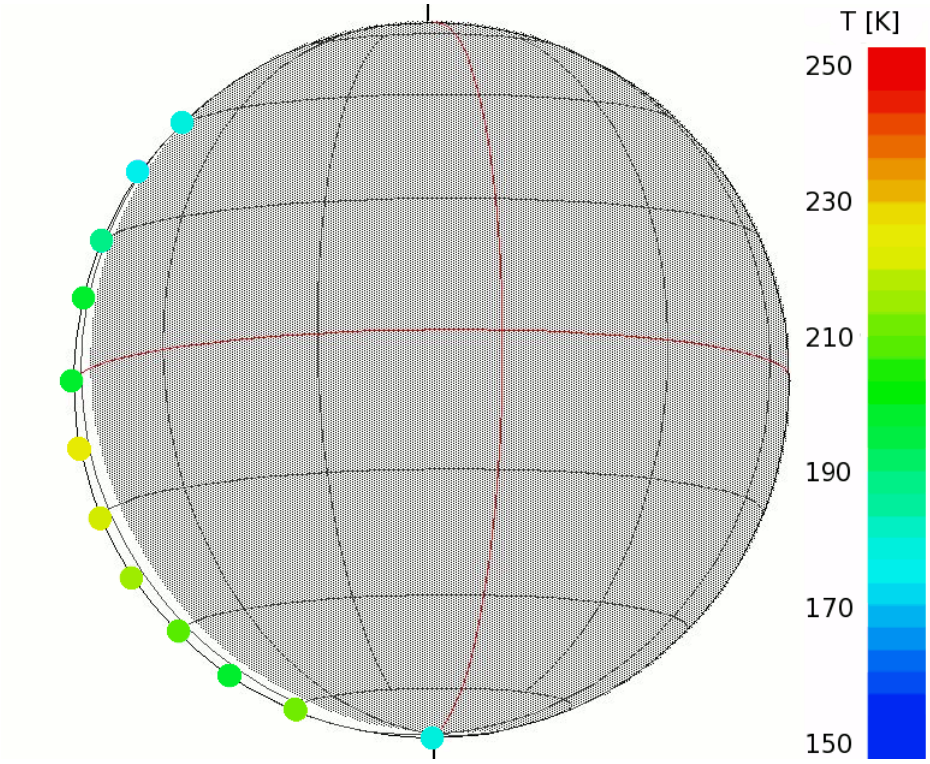

Figure 4.3: *April 2009 Measurements*

DATE	UT	LAT	T [K]	ERR		DATE	UT	LAT	T [K]	ERR
02.04	18:30	-45	210	11		05.04	22:00	0	220	8
02.04	22:10	-22	214	12		05.04	22:30	45	164	17
02.04	22:40	-67	204	28		06.04	14:20	-45	211	6
02.04	23:00	-90	167	16		06.04	15:10	0	190	12
04.04	18:50	-45	188	6		06.04	16:00	-45	208	6
04.04	19:20	0	177	8		06.04	16:20	0	205	6
04.04	20:30	-22	218	9		06.04	16:50	-22	222	6
04.04	21:30	-33	224	11		06.04	17:20	-45	214	6
04.04	21:50	-67	219	17		06.04	17:40	-33	204	5
05.04	16:00	-11	227	9		06.04	18:00	33	176	11
05.04	16:30	11	200	9		06.04	19:00	-45	227	6
05.04	17:00	22	189	8		06.04	19:30	45	193	11
05.04	17:50	-22	203	9		06.04	20:30	-45	206	6
05.04	18:30	-56	197	9		06.04	21:00	-67	223	9
05.04	20:20	-90	197	27		06.04	21:20	-90	181	19
05.04	21:00	-90	188	29		06.04	21:50	-45	215	9
05.04	21:30	-22	238	7						

Table 4.2: Retrieved temperature values in April 2009.

June 2009

In June 2009 we observed Venus at maximum western elongation, with approximately 50% disc illumination. The disc size of Venus (22-23″) was significantly smaller than around inferior conjunction. This is shown in the increased relative beam size indicated in Fig. 4.4. Observed positions now included the illuminated limb plus latitudinal scans from limb to terminator at the equator and at ± 22 and 45 degrees. All retrieved temperatures are given in table 4.3. Temperatures reach ∼255 K near the sub solar point (close to equator/limb) and drop to ∼145 K at the south pole and near the terminator. The Earth-Venus topocentric Doppler shift varied between +13.5 and +14.5 km/s.

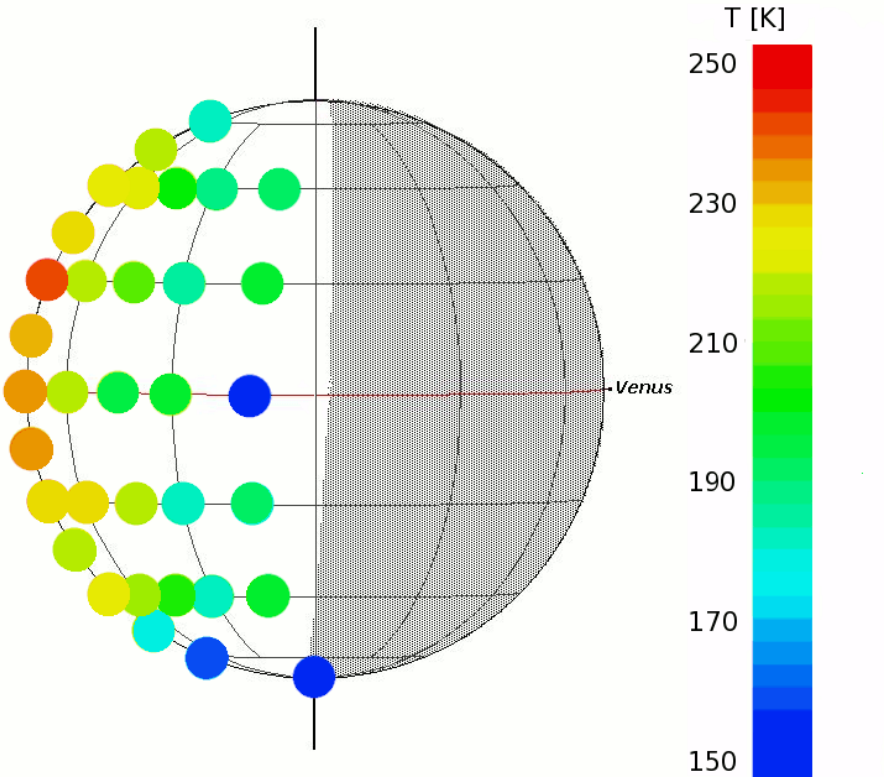

Figure 4.4: *June 2009 Measurements*

DATE	UT	LAT	LONG	T [K]	ERR		DATE	UT	LAT	LONG	T [K]	ERR
02.06	13:00	0	90	234	3		04.06	12:45	0	90	237	20
02.06	13:45	-22	90	216	3		04.06	13:30	-11	90	225	11
02.06	14:15	22	90	238	5		04.06	14:00	11	90	225	8
02.06	14:45	-45	90	226	7		04.06	14:30	33	90	222	7
02.06	15:15	45	90	217	4		04.06	15:00	-33	90	223	5
02.06	15:30	0	90	238	5		04.06	15:15	-56	90	203	6
02.06	16:00	67	90	191	4		04.06	15:45	56	90	218	4
02.06	16:30	-67	90	164	7		04.06	16:00	22	90	240	5
02.06	17:00	-11	90	247	6		04.06	16:45	22	60	203	10
02.06	17:30	11	90	238	10		04.06	17:30	-90	0	157	20
02.06	17:45	0	90	240	13		04.06	18:00	22	60	222	4
02.06	18:30	-33	90	214	9		04.06	18:30	22	45	202	4
02.06	19:15	33	90	234	9		04.06	18:45	22	30	191	6
02.06	20:00	-56	90	197	16		06.06	15:00	0	90	254	9
02.06	20:30	56	90	221	38		06.06	15:30	-22	90	247	9
02.06	21:00	0	90	242	21		06.06	15:45	-22	60	228	4
03.06	12:30	0	90	222	5		06.06	16:30	-22	45	217	4
03.06	13:00	0	60	217	3		06.06	16:45	-22	30	182	6
03.06	13:15	0	45	195	5		06.06	17:30	0	15	149	10
03.06	13:45	0	30	202	7		06.06	17:45	-45	15	198	11
03.06	14:00	-45	90	219	9		06.06	18:30	45	15	194	19
03.06	14:30	-45	60	214	4		06.06	18:45	22	15	195	15
03.06	15:00	-45	45	206	3		06.06	19:15	-22	15	190	21
03.06	15:30	-45	30	183	4		06.06	20:00	0	90	212	12
03.06	16:00	45	90	241	8		07.06	12:30	0	90	241	9
03.06	16:15	45	60	223	4		07.06	12:45	-45	90	229	9
03.06	16:30	45	45	205	3		07.06	13:15	45	90	214	5
03.06	17:00	45	30	188	4		07.06	13:30	-22	90	229	12
03.06	17:45	22	90	247	7		07.06	14:30	-67	90	163	9
03.06	18:00	22	60	226	4		07.06	14:45	67	90	174	7
03.06	18:30	22	45	217	4		07.06	15:15	-90	0	143	25
03.06	19:00	22	30	180	5							
03.06	19:30	-22	90	214	18							

Table 4.3: Retrieved temperature values in June 2009. 'Long' gives longitude offset east of the central meridian in degrees.

4.2 HIPWAC @ IRTF

With HIPWAC it is possible to measure also the rotational temperature of CO_2 by observing the relative intensity of different transition lines. Kinetic and rotational temperatures are assumed to be identical in thermodynamic equilibrium.
From 22–24 October 2007 we observed Venus at the 10.6 μm band of CO_2 using the 3 m NASA Infrared Telescope Facility (IRTF) on Mauna Kea, Hawaii. The observing geometry was similar to the June 2009 run: near maximum western elongation, the morning hemisphere illuminated. We observed 9 different rotational-vibrational lines in the P-branch of the 10 μm band of CO_2 at 45° latitude in both hemispheres as well as at the equator and at 70° southern latitude close to the South polar vortex. All positions on the disk were observed at a given J-level in close temporal proximity thus minimising effects of the instrument or a possibly changing atmosphere. In addition a set of measurements along the equator at various longitudes was acquired for the P(12) transition. Each observation lasted from 4 to 30 minutes depending on line intensity. The angular diameter of Venus varied from 26 to 25 arc-seconds over the course of the observing period compared to the diffraction limited FOV of the telescope of ∼1 arc-second. The Earth-Venus topocentric Doppler shift varied between 12.5 and 13.5 km/s.

A typical spectrum from Venus is presented in Fig. 4.5. Shown is the P(16) line observed at 45° East (45E) of central meridian longitude (CML) and the equator. An overview of all observed lines is given in Tab. 4.4.

An example of the measurements that were taken at each point on Venus is illustrated in Fig. 4.7. All emission lines (J=8 to 30) measured at the equator, 45E position are shown. The integration time for each line was chosen such that a similar signal-to-noise ratio (SNR) of ∼5 at the full spectral resolution of ∼1 MHz was reached thus yielding comparable fitting results for each line with respect to width and intensity.

Fig. 4.8 and Tab. 5.1 depicts the results of the rotational temperature analysis. The panels in Fig. 4.8 show the retrieved intensities plotted against the J-levels at all observed positions on Venus from North to South (45N, Equator, 45S, 70S). A Boltzmann distribution according to

$$I_{P(J'')} \sim I_0 \cdot \nu^4_{J' \rightarrow J''} \cdot (2 \cdot J'') \cdot e^{\frac{-hcB \cdot J''(J''-1)}{k_B T_{rot}}} \tag{4.2}$$

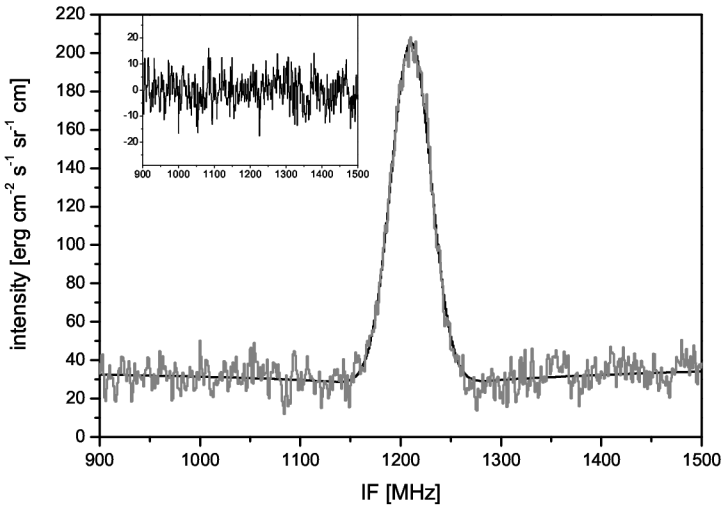

Figure 4.5: *A typical non-LTE CO_2 emission spectrum from Venus. Plotted is the intensity vs. the intermediate frequency for the P(16) line at 947.74198 cm^{-1}. Data were taken at the equator and 45° offset from Venus CML. Integration time was ∼4 minutes. Plotted over the data is a fit to the observed line using a radiative transport code (see text for more information). The inset plot shows the residuals. The linewidth of 47.03 MHz yields a temperature of 234.9 ±5 K according to Eq. 4.1.*

was fitted to the observed intensities to determine the rotational temperatures T_{rot} [63]. In Eq. 4.2, J'' denotes the lower J-level of the transition (as used in the line label $P(J'')$), B is the rotational constant of CO_2 having a value of 0.38714 cm^{-1} [64] for the involved vibrational state and the fundamental constants k_B, c and h have their usual values. The errors from the Gaussian fits to the individual emission lines in addition to a 3% calibration error were used as weigths in the fitting process. The errors given in Fig. 4.8 and Tab. 5.1 are 1-σ uncertainties as calculated by the least-square fitting routine according to Eq. 4.2.

The temperatures retrieved from the linewidths of all lines observed at a given position were averaged to determine the kinetic temperature for this position. The standard deviation for the mean values is 2–6 K.

Table 5.1 gives an overview and comparison of the retrieved values

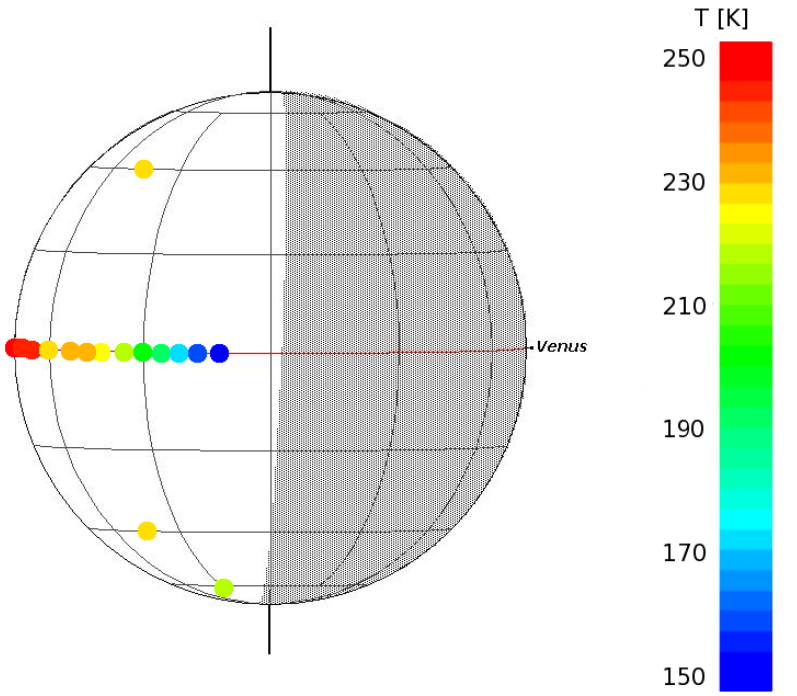

Figure 4.6: *Observed mean temperatures on the Venusian disc. Note the smaller field of view compared to observations at Kitt Peak (Fig. 4.4 due to the bigger mirror at the IRTF.*

for the rotational and the kinetic temperatures from the observations of nine J-levels at latitudes 45N/S, equator and 70S as well as the corresponding VIRA values for the deduced altitude range (see section Introduction). In addition Fig. 4.9 and Table 4.6 present all kinetic temperature values retrieved from the observation of the P(12) line at various SZA along the equator.

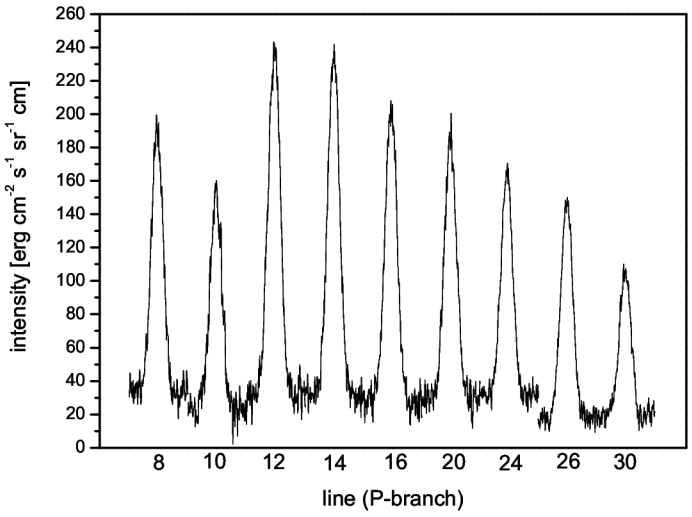

Figure 4.7: *Plot of all observed lines in the 10.6 μm P-branch of the CO_2 molecule. The spectra are calibrated using a built-in blackbody source and the known transmittance of the instrument optics. The uncertainty in the absolute calibration for the whole band is $\sim$10%. The integration time was chosen such that a similar SNR was achieved on all lines.*

Date	Time [UT]	Line	Position Lat/Lon	Intensity [erg/(s cm2 sr cm-1)]			Width (FWHM) [MHz]		
22.10.2008	17:53	P(10)	Eq/45E	133.05	±	1.59	47.43	±	0.52
	17:59	P(10)	45S/45E	159.92	±	1.44	46.27	±	0.40
	18:05	P(10)	45N/45E	150.20	±	1.54	48.20	±	0.45
	18:19	P(10)	70S/30E	85.77	±	1.45	47.33	±	0.78
	18:37	P(14)	Eq/45E	209.59	±	1.13	47.33	±	0.24
	18:43	P(14)	45S/45E	171.49	±	1.23	46.74	±	0.31
	18:54	P(14)	45N/45E	199.71	±	1.23	47.10	±	0.28
	19:05	P(14)	70S/30E	101.27	±	1.21	44.93	±	0.49
	19:30	P(20)	Eq/45E	160.72	±	1.35	49.19	±	0.38
	19:36	P(20)	45S/45E	105.33	±	1.27	50.46	±	0.54
	19:41	P(20)	45N/45E	149.76	±	1.32	47.69	±	0.40
	19:47	P(20)	70S/30E	61.45	±	1.30	45.35	±	0.80
	20:08	P(30)	Eq/45E	87.86	±	1.03	44.46	±	0.47
	20:19	P(30)	45S/45E	48.83	±	1.04	44.46	±	0.75
	20:29	P(30)	45N/45E	69.13	±	1.01	46.60	±	0.59
	20:41	P(30)	70S/30E	27.11	±	0.63	46.32	±	1.15
	21:11	P(26)	Eq/45E	132.79	±	0.91	46.96	±	0.31
	21:23	P(26)	45S/45E	59.11	±	0.90	47.45	±	0.68
	21:44	P(26)	45N/45E	105.09	±	1.00	45.94	±	0.42
	21:55	P(26)	70S/30E	68.83	±	1.33	46.55	±	0.87
23.10.2008	16:26	P(12)	Eq/45E	214.14	±	1.45	48.11	±	0.31
	16:32	P(12)	45S/45E	214.82	±	1.45	48.30	±	0.31
	16:38	P(12)	45N/45E	155.64	±	1.50	46.25	±	0.42
	16:45	P(12)	70S/30E	120.20	±	1.56	44.04	±	0.47
	17:01	P(8)	70S/30E	106.72	±	1.49	45.66	±	0.49
	17:06	P(8)	45N/45E	155.50	±	1.40	46.74	±	0.40
	17:11	P(8)	45S/45E	157.58	±	1.34	47.38	±	0.38
	17:17	P(8)	Eq/45E	163.23	±	1.35	46.77	±	0.35
	17:30	P(16)	Eq/45E	180.36	±	1.42	47.03	±	0.35
	17:35	P(16)	45S/45E	195.18	±	1.41	46.72	±	0.31
	17:39	P(16)	45N/45E	180.33	±	1.36	47.17	±	0.33
	17:45	P(16)	70S/30E	127.87	±	1.42	47.14	±	0.40
	18:00	P(24)	70S/30E	72.70	±	0.98	45.00	±	0.47
	18:14	P(24)	45N/45E	134.87	±	0.94	46.41	±	0.31
	18:23	P(24)	45S/45E	127.17	±	0.99	45.17	±	0.33
	18:34	P(24)	Eq/45E	137.51	±	0.97	46.25	±	0.31
24.10.2008	16:54	P(12)	Eq/60E	237.24	±	1.53	47.00	±	0.28
	17:00	P(12)	Eq/70E	285.32	±	1.54	48.63	±	0.24
	17:05	P(12)	Eq/80E	381.13	±	2.15	48.53	±	0.26
	17:10	P(12)	Eq/90E	482.29	±	2.96	49.45	±	0.28
	17:35	P(12)	Eq/50E	185.60	±	1.63	47.17	±	0.38
	17:40	P(12)	Eq/40E	137.90	±	1.67	46.60	±	0.57
	17:45	P(12)	Eq/30E	99.72	±	1.51	44.06	±	0.59
	17:51	P(12)	Eq/20E	71.05	±	1.45	40.71	±	0.82
	17:58	P(12)	Eq/10E	38.69	±	1.23	34.03	±	0.92
	19:39	P(12)	Eq/15E	50.00	±	0.95	39.21	±	0.57
	19:51	P(12)	Eq/25E	101.86	±	1.13	43.02	±	0.38
	20:03	P(12)	Eq/35E	144.37	±	1.17	45.92	±	0.35
	20:12	P(12)	Eq/45E	211.27	±	1.36	48.06	±	0.28

Table 4.4: *Summary of all observations of non–LTE CO_2 lines on Venus 2007. Longitudes on Venus are relative to CML.*

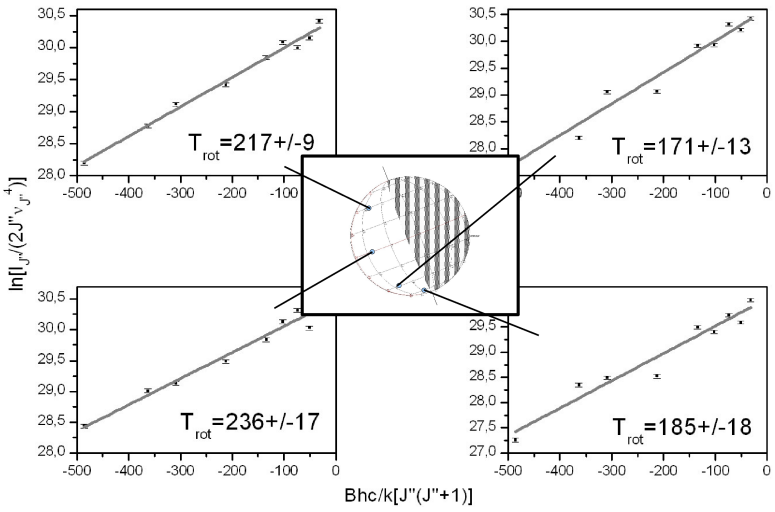

Figure 4.8: *Plot of the intensities of the measured lines at the four positions on Venus. We measured nine rotational lines from P(8) to P(30) in the 10.6 μm band of CO_2. A Boltzmann distribution was fitted to the intensity distribution (see Eq. 4.2). The retrieved temperature range is about 171–236 K.*

observed position	SZA	alt. [km]	T_{rot} [K]	T_{kin} [K]	T_{VIRA} [K]
45° North / 45° East	60°	100–120	217±9	235±2	172–189
Equator / 45° East	45°	100–120	236±17	236±4	175–189
45° South / 45° East	60°	100–120	171±13	236±6	172–189
70° South / 30° East	80°	100–120	185±18	224±4	166–189

Table 4.5: *Retrieved values for the rotational and the kinetic temperatures on various positions on the Venus disc (latitude/offset from CML). Errors are 1-σ probabilities. For comparison the SZA and the corresponding VIRA values for the observed latitude and altitude range of ∼100–120 km are given as well.*

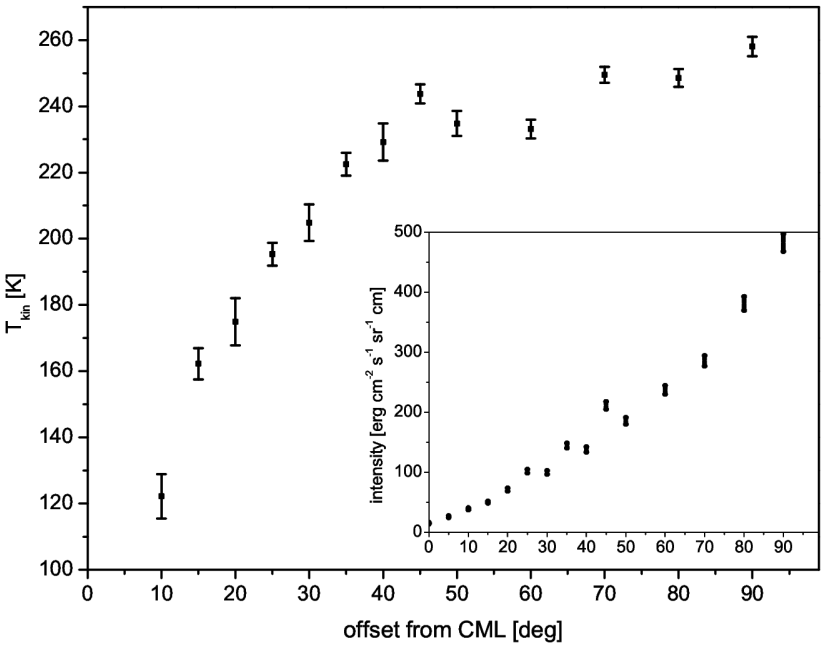

Figure 4.9: *Plot of the temperatures retrieved from observations of the P(12) line at various offsets from CML along the equator. The inset shows the corresponding line intensities.*

observed position	SZA	T_{kin} [K]
Equator / 10° East	83°	122±7
Equator / 15° East	78°	162±5
Equator / 20° East	73°	175±7
Equator / 25° East	68°	195±3
Equator / 30° East	63°	205±6
Equator / 35° East	58°	223±3
Equator / 40° East	53°	229±6
Equator / 45° East	48°	244±3
Equator / 50° East	43°	235±4
Equator / 60° East	33°	233±3
Equator / 70° East	23°	250±2
Equator / 80° East	13°	249±3
Equator / 90° East	3°	258±3

Table 4.6: *Retrieved values for the kinetic temperatures on various positions along the equator relative to the CML. Errors are 1-σ probabilities. The SZA is given as well.*

4.3 IRHS @ IRTF

Using the NASA Goddard Infrared Heterodyne Spectrometer (IRHS) Venus was observed many times from the 1970s until today. Here, a re-analysis of four observing campaigns from 1990 and 1991 is presented. All campaigns were scheduled around inferior conjunction, Jan. 18^{th} 1990 respectively Aug. 22^{nd} 1991, similar to the observations made in March / April 2009.

Table 4.7: *Re-analysed IRHS observing campaigns.*

observing period	inf. conj.	Venus app. size	illum. limb
Jan 3-5 1990	Jan 18 1990	56-58°	evening
Feb 4-5 1990	Jan 18 1990	53-54°	morning
Aug 9-11 1991	Aug 22 1991	53-55°	evening
Sep 6-9 1991	Aug 22 1991	51-53°	morning

All observations were performed at the NASA Infrared Telescope Facility (IRTF) on Mauna Kea, Hawaii. The IRHS was located at the Coudé room of the IRTF.

The angular diameter varied from 51 to 58 arc-seconds, see table 4.8, the field of view of IRHS at the IRTF is 0.85 arc-seconds at 10 μm wavelengths.

Fig. 4.10 shows a typical spectrum of the observed R(8) line of the 10.4 μm band of CO_2. The spectrum was observed on Jan 4th 1990 at the equator and 70 degrees west of the central meridian line (CML). To derive the temperature, every A and B beam was fitted seperately. The selection process of scans to be included in further analysis was done by identifying 'bad scans' which were corrupted possibly due to bad weather or possible technical problems. Those bad scans usually had a fairly low SNR and showed an increased line width. The resulting mean value of the line width distribution was then attributed to the searched atmospheric temperature.

Lamb-dip stabilisation was used which yielded a stability of the local

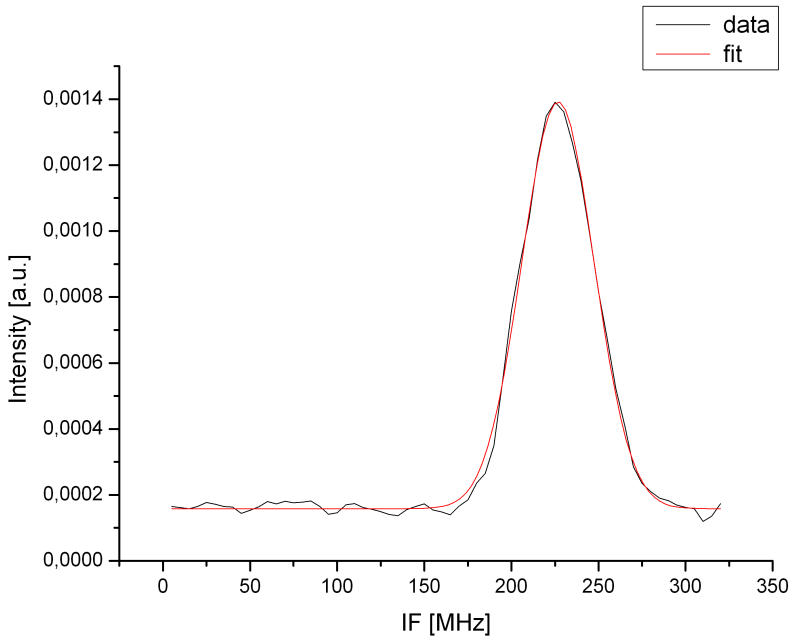

Figure 4.10: *Typical spectrum of a IRHS observation. The spectral resolution is 5 MHz.*

oscillator of less than 0.1 MHz. Figs. 4.11, 4.12 and Table 4.8 present the observing geometry and the observed positions on the Venusian disk.

Table 4.8: *Retrieved values for the kinetic temperatures. Observed position gives latitude and offset to the CML. The solar zenith angle is given as well. Errors are 1-σ probabilities.*

observed position	SZA	T_{kin} [K]
Equator / 70° West	81°	236±5
60 S / 70° West	84.5°	207±5
80 S / 70° West	87°	206±8
40 N / 70° East	81.5°	200±5
Equator / 70° East	79°	207±6
60 S / 70° East	82.5°	220±3
80 S / 70° East	85.5°	219±5
70 N / 75° West	85.5°	197±6
40 N / 75° West	83°	223±5
20 N / 75° West	82.5°	235±13
Equator / 75° West	83°	214±9
20 S / 75° West	84°	204±6
80 N / 75° East	85.5°	199±6
60 N / 75° East	82.5°	212±9
40 N / 75° East	80°	210±9
20 N / 75° East	79°	216±6
Equator / 75° East	79°	224±5

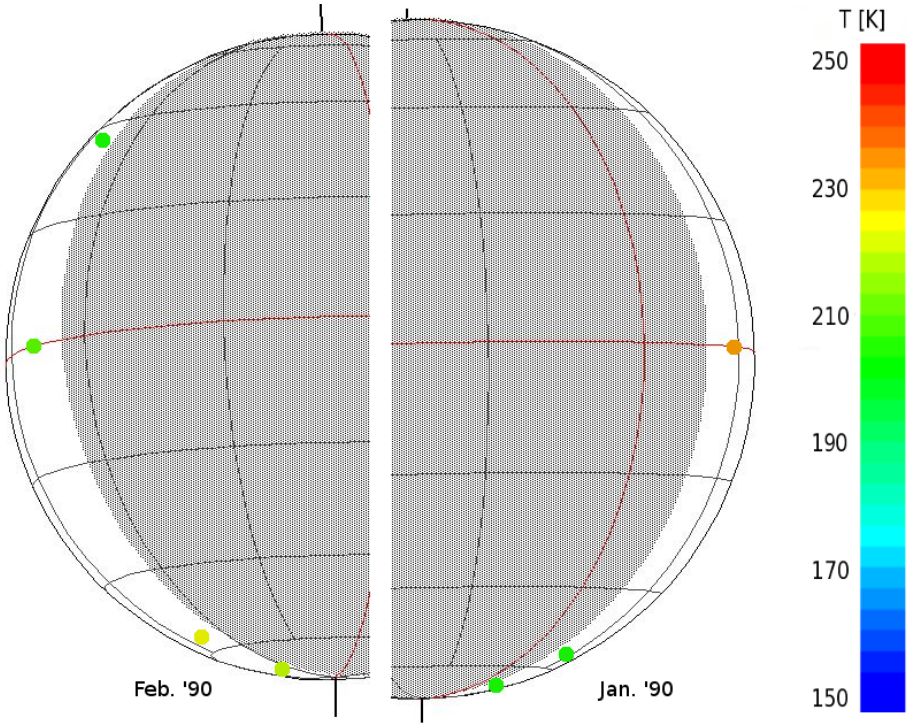

Figure 4.11: *All IRHS Measurements 1990.*

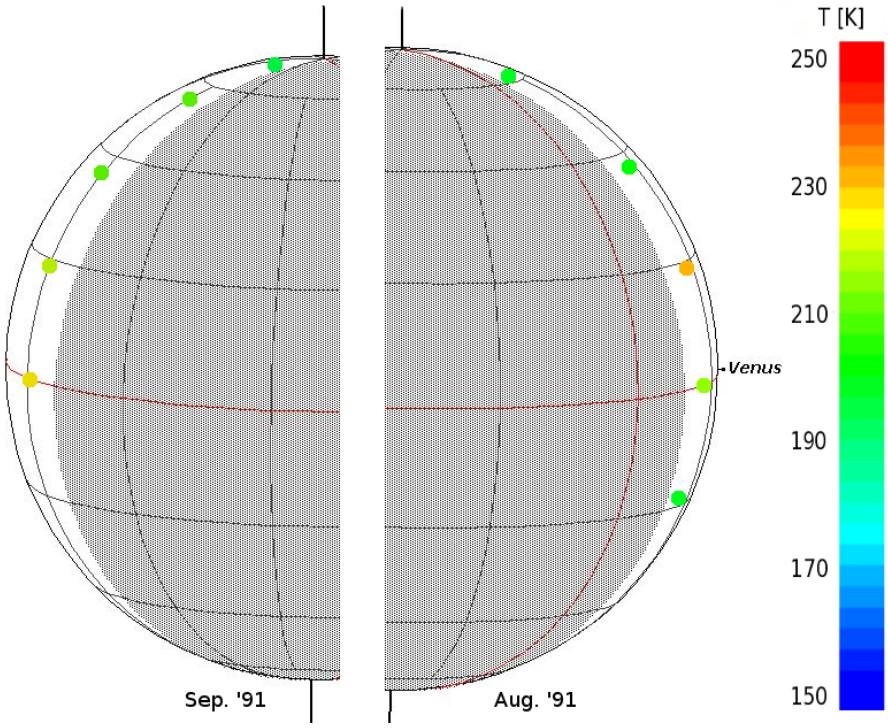

Figure 4.12: *All IRHS Measurements 1991.*

Chapter 5

Data Analysis

In this chapter, I will discuss the results obtained with infrared heterodyne spectroscopy. Short-term variations as well as long-term changes in mesospheric temperatures are investigated. Observations are compared to other retrieval techniques and to model predictions.

5.1 HIPWAC @ IRTF

observed position	SZA	alt. [km]	T_{rot} [K]	T_{kin} [K]	T_{VIRA} [K]
45° North / 45° East	60°	100–120	217±9	235±2	172–189
Equator / 45° East	45°	100–120	236±17	236±4	175–189
45° South / 45° East	60°	100–120	171±13	236±6	172–189
70° South / 30° East	80°	100–120	185±18	224±4	166–189

Table 5.1: *Retrieved values for the rotational and the kinetic temperatures on various positions on the Venus disc (latitude/offset from CML). Errors are 1-σ probabilities. For comparison the SZA and the corresponding VIRA values for the observed latitude and altitude range of ∼100–120 km are given as well.*

From Table 5.1 it can be seen that only for the Equator position the kinetic temperatures match the rotational temperatures within the

1-σ error bars whereas they do not match in the 45N, 45S and 70S observations. The reason for the differences is not obvious. The observed line intensities scatter widely around the Boltzmann distribution curve while the fitting errors for the intensities that go into the plot are rather small. We cannot identify any systematic variations which point to instrumental issues or to variations only affecting individual J-level transitions. In addition, since observations on any J-level transition were performed in close temporal proximity at all four positions on Venus, any such variations would affect all positions similarly. We also see temporal changes in the line intensities of the P(12) observations along the equator: in the inset of Fig. 4.9 showing the intensities vs. the observed position on the Venus disc the values for 25E, 35E, and 45E clearly fall above the observations at 30E and 40E. Here again no instrumental or atmospheric causes could be identified. However, due to the observing sequence used, the odd positions in question (25E, 35E, 45E) were measured $\sim$3 hours after the neighbouring positions. Therefore, this also supports the conclusion of temporal variation in the intensities of the emission lines.

This might also explain the observed asymmetry in rotational temperature between the northern and southern hemispheres of Venus at mid-latitudes (45°). While the kinetic temperatures agree within the error bars for both hemispheres the rotational temperatures do not. If the line intensities show strong temporal variations this effect might impede the retrieval of useful temperature information from the data set acquired over a period of two days.

The possibility of non-negligible contribution from stimulated emission to certain J-levels was ruled out since we do not observe significant gain narrowing.

The kinetic temperatures of 224–236 K are above the VIRA temperatures for the altitude range from 100–120 km and also above the values reported from previous infrared heterodyne observations [55].

5.2 IRHS @ IRTF

Three out of four observations show the expected behaviour of decreasing temperatures towards the terminator and the poles. February 1990 is the exception, showing higher temperatures at 60 and 80 degrees southern latitude. While a single warm measurement at 80° would immediately raise the question if the polar vortex could have an influence, such as shifting the non-LTE emitting region downward, the combination with a warm measurement at 60° contradicts this hypothesis. Measurements [65] of the southern polar vortex show that the altitude of the low latitude cloud structure is stable until 60° and then gradually decreases from 72 to 64 km in the centre of the polar vortex. This of course can not be used alone to infer any similarities with altitude regions of 115 km, but it is the only hint to explain such exceptional results like the February 1990 data. Measurements in January 1990 (80° south) and September 1991 (80° north) do not show a polar warming. But, the polar vortices are known to be highly variable [66], see Fig. 5.1 so this does not eliminate the vortex hypothesis. As the vortex is assumed to be associated with rapid down-welling, the warm temperatures could be explained by an exceptionally high amplitude of the vortex, efficiently reaching latitudes as low as 60 degrees, with down-welling creating turbulences and adiabatic warming and thus altering the temperature at the pressure levels where the non-LTE emission takes place.

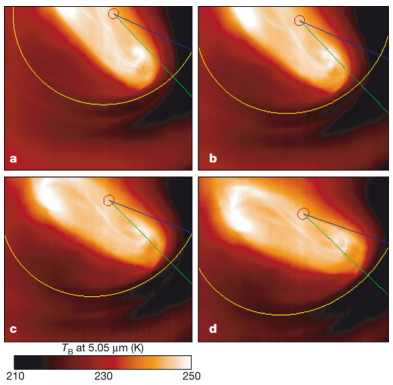

Figure 5.1: *South polar vortex, observed by VIRTIS [66]. Four observation with a time interval of 1 hour at 5 μm , probing an altitude of ∼60 km. Red circle: south pole. Yellow circle: 70° southern latitude. Blue and green curves: meridians at 330° and 350° longitude. The vortex is rotating with a period of 2.5 days.*

5.3 Short-Term Variations

The Venus upper atmosphere is not as stable and simply structured as believed earlier. Our measurements of mesospheric temperatures revealed basic differences like generally higher temperatures, but also variations on very short time scales. In contrast to the IRHS observations, THIS observed some positions repeatedly which enables us now to investigate these variations.

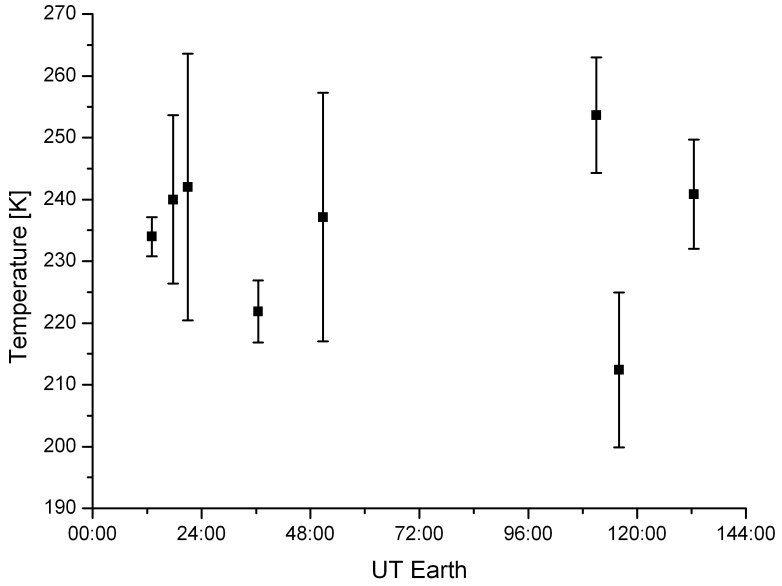

Figure 5.2: *Temperature variations at equator/limb. X- axis are hours after June 2nd 2009 0h UT.*

Fig. 5.2 shows such short-term variations at the position equator/limb during the June 2009 observing run at Kitt Peak. Eight observations during 6 days yield a peak to peak variation of up to 40 K. The two extreme values even were recorded only hours apart. This also reduces the likelihood of technical reasons for this variation as the spectrometer was not modified by any means between those two measurements, so every power supply noise or any other technical influence was the same, leaving a strong indication of true

temperature variation. The biggest uncertainty comes from possible pointing errors as little displacements of the beam on the disc may evoke big temperature variations. However, the biggest gradients are at the vicinity of the day-night terminator, around the subsolar point near equator-limb (for the June 2009 geometry) the measured mean temperatures are very similar.

Such variations are consistent with variations seen by Clancy et al. at sub-mm wavelengths with a spread of 20 K over 9 days (see chapter 5.6 and Fig. 5.14). Also SPICAV and VIRTIS observed variations with similar magnitude. A possible explanation for this high variability is a higher degree of turbulence in the transition zone between superrotation and SS-AS flow.

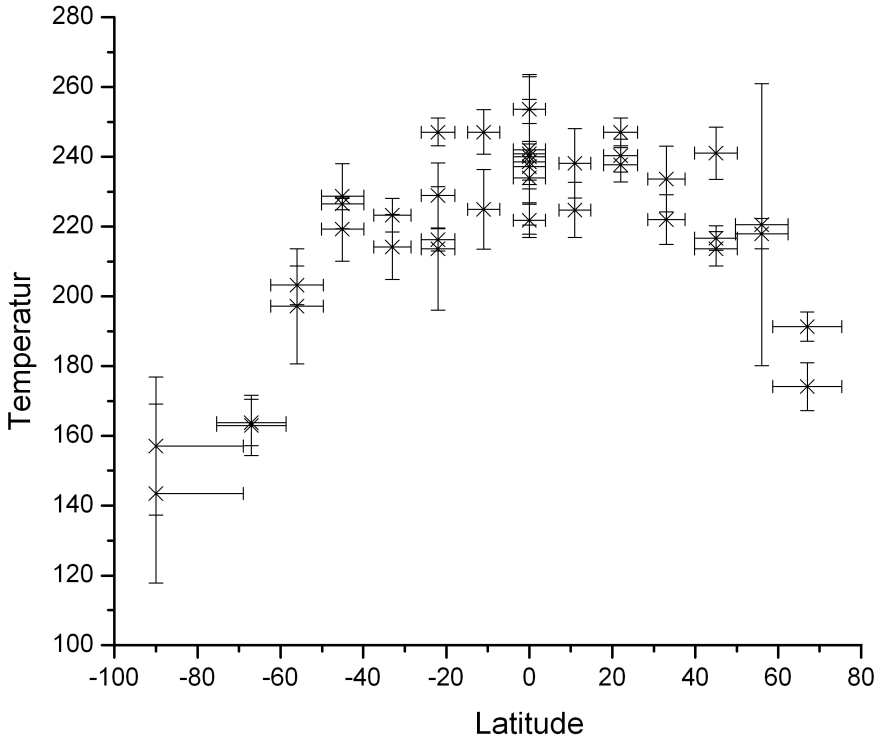

Figure 5.3: *Temperatures at all limb positions during the June 2009 run. The strong latitudinal correlation is as obvious as the strong variation of up to 40 K at the equator.*

5.4 Mid-Term Variations

5.4.1 Inferior Conjunction Morning/Evening Symmetries

In the model of SSAS dominated atmosphere, of a homogeneous temperature distribution from hot (sub solar point) to cold (anti solar point) is predicted and observations at inferior conjunction should produce identical results as the solar zenith angle is approx. 90° for all limb positions. However, as a minimum of illumination is required, observations were scheduled with a time lag of one (2009) or two weeks (1990/91) around inferior conjunction. Thus, SZA varied from 90° at the tips of the crescent down to 65°. Consequently, it is expected to observe warmer temperatures at the bulge of the crescent than at its tips.
As it is not clear, at which altitude the SSAS flow becomes dominant it is important to check these possible symmetries.

THIS March / April 2009
The mean temperatures for all observed positions during the March and April 2009 runs are plotted in Fig. 5.4. Also included are possible global temperature distributions assuming a homogeneous 'model' atmosphere with minimum SZA angles at latitude 25S. It is obvious that April temperatures are higher than in March on the southern hemisphere. Unfortunately, all March data for the northern hemisphere was lost due to technical and weather problems.
Also a big variability can be seen with an amplitude of 15 K around the global mean.

IRHS 1990/91
With regard to the expected morning / evening symmetries the observations taken with IRHS show a even more variable picture. Although it is difficult to retrieve significant conclusions from as few data points as observed e.g. in 1990, some facts can be stated: while the measurements in 1991 globally agree (although within significant variations) with the homogeneous model - warm crescent bulge, cool tips - the February data are significantly different with warmer measurements at 60S and 80S than at the equator. The absolute values of $\sim$220 K also are 20–30 K warmer than observations at those latitudes during other IRHS or THIS runs.
Again, for both campaigns, there seems to be variability of around

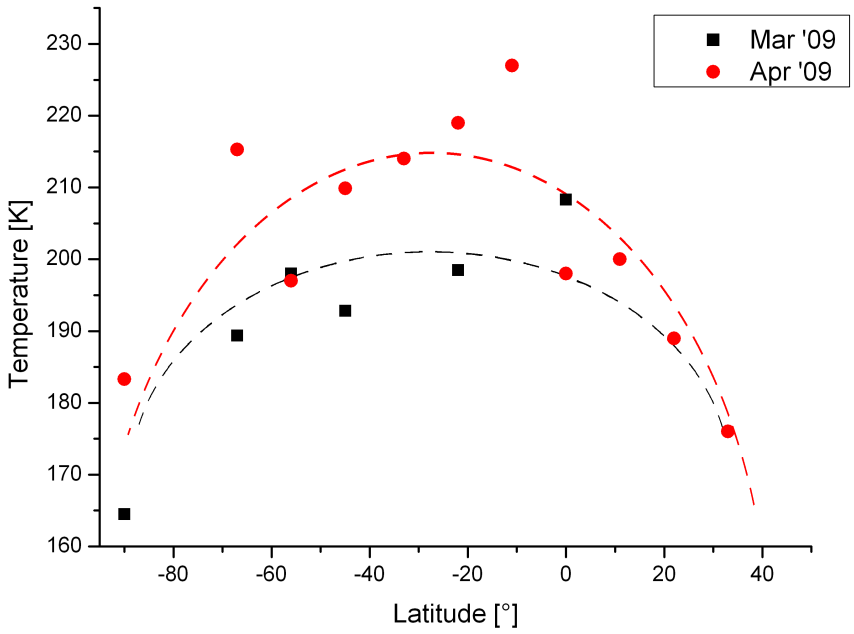

Figure 5.4: *Mean temperatures vs. latitude for the March/April 2009 runs with THIS. Dashed lines suggest the global trend with highest temperatures at the most illuminated latitude (lowest SZA, 25° South). Morning temperatures (April) are slightly higher.*

20 K in the period of two weeks until a month between observations before and after inferior conjunction.

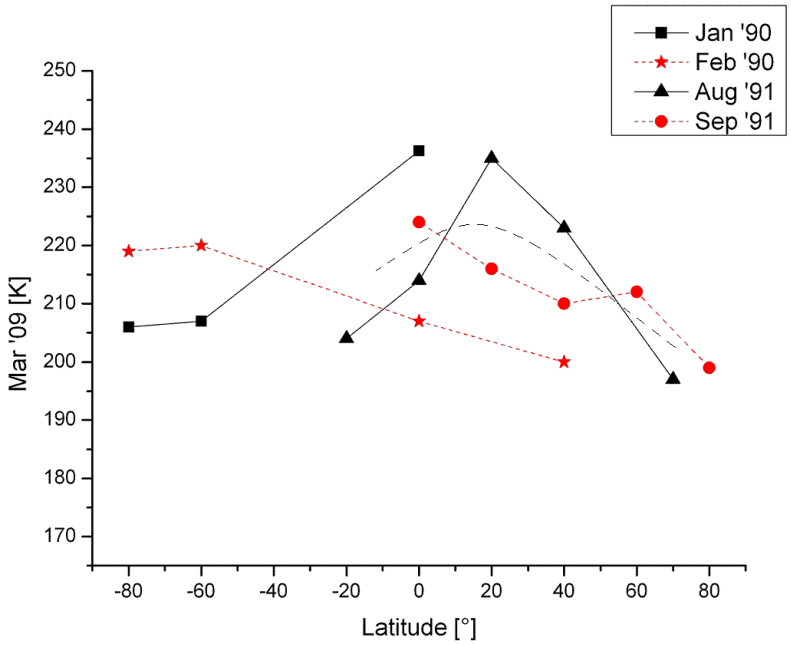

Figure 5.5: *Temperatures vs. latitude for the four IRHS runs. Black indicates evening, red morning limb observations. While in 1991 a global temperature trend might be present (dashed black line), the 1990 observations show a clear asymmetry with unusual high temperatures near the south pole.*

5.5 Long-Term Variations

All IRHet observations
By comparing the results obtained with the three different infrared heterodyne instruments one can see that THIS was observing the lowest temperatures. Both data sets, around inferior conjunction (compared to IRHS, see Fig. 5.6) and at maximum western elongation (compared to HIPWAC, Fig. 5.7) are supporting this. A comparison of IRHS and HIPWAC is difficult due to the different illumination of Venus.
There are two explanations for this observation: either, the CO_2 laser in HIPWAC and IRHS is significantly more noisy than the QCL in THIS, e.g. due to a noisy high voltage power supply, or the variations are real temperature fluctuations. Of course it is difficult to reanalyse data taken twenty years ago. People involved in the project claim that the Lamb dip lock was working very accurately keeping the centre frequency within 0.1 MHz. If the laser power supply was noisy which could lead to a significant line broadening, the lock signal from the Lamb dip cell should have also been affected as the dip itself would have been less pronounced than without the noise. As this was not observed - the width of the lamb dip was measured to be 3–4 MHz which could be explained by power broadening [20]. Also, the whole IRHS spectrometer was set up on optical benches in the Coudé room which ensures a maximum of mechanical stability. It therefore seems plausible that the reason of the broader lines is caused by the observation of higher temperatures rather than by technical effects.

There is another explanation that different lines (THIS used the P12 and P16, HIPWAC used P8-P30, but mainly also P12, while IRHS used the R8 line of the 10.6 μm band) might probe different altitudes and therefore yield unequal temperatures. This effect, however, should be at a scale of a few kilometres only, so that temperature variations there should be negligible [67].

5.5.1 2007-2009 Maximum Elongation

Both observing runs, in 2007 and June 2009 were done at maximum western elongation and therefore are ideally suited to study long-term variations in the mesosphere of Venus. The detailed scan along the illuminated part of the equator taken in 2007 is compared to data

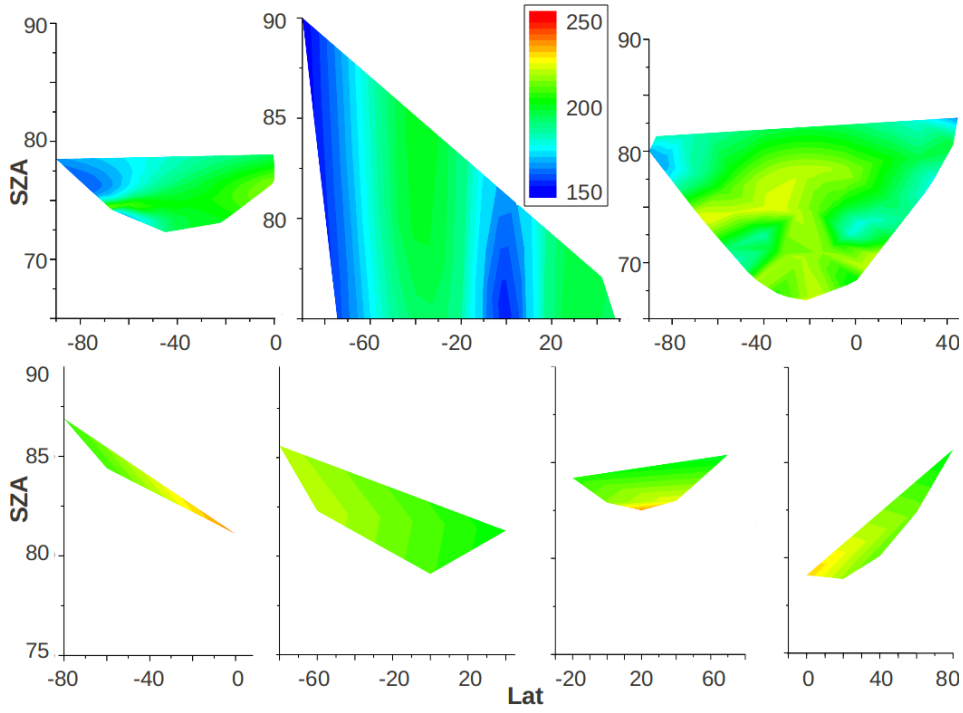

Figure 5.6: *Measured temperatures are plotted regarding their latitudinal position and solar zenith angle. The values are smoothed over the observed Latitude/SZA area. In the upper half, observations from 2009 are shown (March, June (only high SZA observations) and April), at the bottom, IRHS measurements are displayed (Jan90, Feb90, Aug91, Sep91). IRHS observations were done at higher SZA thus are expected to show lower temperatures. Instead, slightly higher temperatures are observed.*

from June 2009 and shown in Fig. 5.7. It is obvious that the temperatures seen in 2009 data is significantly lower than those seen in 2007 data throughout the whole equator scan by 20 K on average. This is also the case for the three non-equator positions measured in 2007, they too are on average 20 K higher than in 2009.

5.5.2 1990-2009 Inferior Conjunction

The observing runs with the IRHS taken around inferior conjunction are very similar to the 2009 March/April runs. The IRHS runs were scheduled two weeks before and after IC (THIS: one week), but they did not observe at the limb but in the middle of the crescent. This results in even higher SZA values for IRHS runs compared to THIS

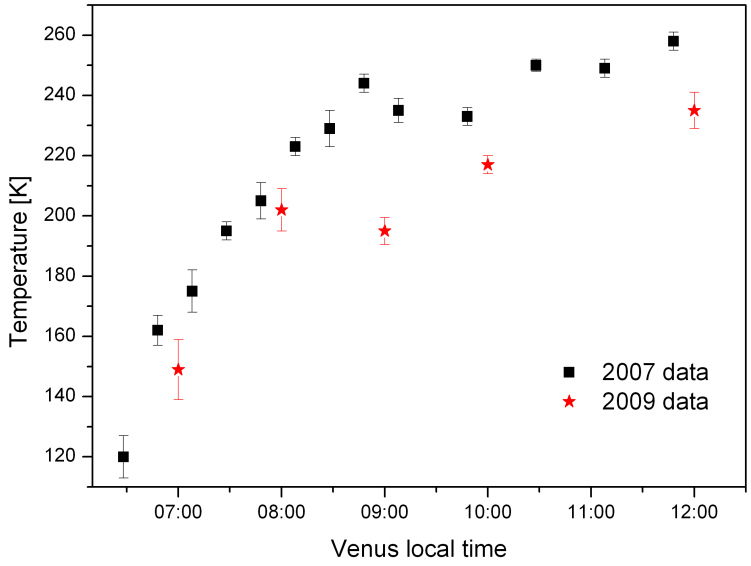

Figure 5.7: *Scan along the equator. Black: temperatures retrieved with HIPWAC 2007, red: results from June 2009 (THIS)*

data. In contrast to the thus expected lower temperatures, IRHS was observing comparable and even higher temperatures than THIS (see Figs. 5.6 and 5.8).

The reason why THIS is seeing lower temperatures than IRHS and HIPWAC is not clear. Although short and mid-term variations would certainly be able to add up to such differences it is striking that basically all 5 observation runs using a CO_2-LO yield higher temperatures than the three QCL-LO runs with THIS. A systematic difference can therefore not be ruled out and can only be addressed by a careful linewidth monitoring of the HIPWAC LO.
However, as long as not falsified, it is equally possible that the observed temperature drift is real. In this regard, an important aspect might be the solar activity. It is well proven that temperatures in the higher thermosphere (around 200 km) do significantly differ between solar activity minimum and maximum [68], [69] report for 160–170 km altitude a neutral atmosphere temperature shift from 250 K during solar minimum to 300 K during solar maximum.
Observations with IRHS in 1990 and 1991 were done in concurrence

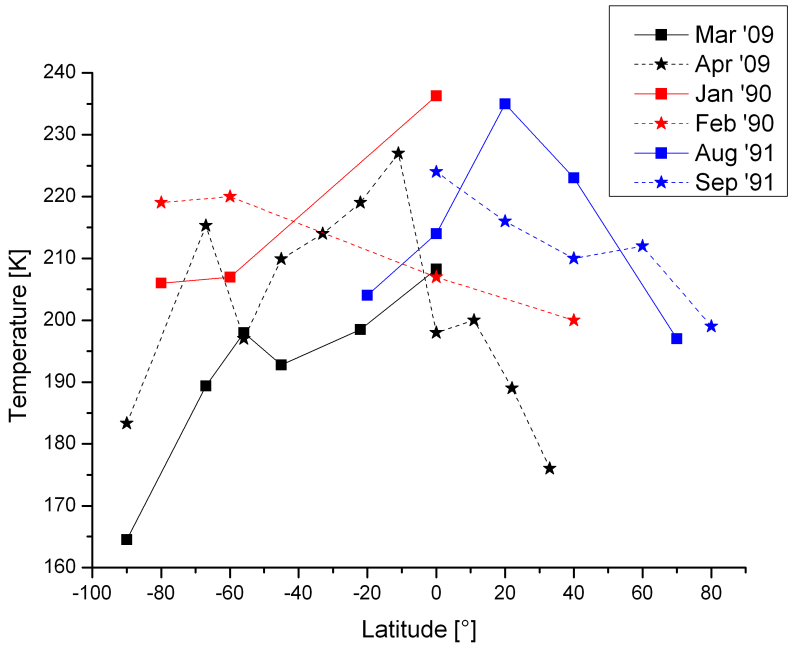

Figure 5.8: *Mean temperatures from all 'near-IC' runs. Note that solar zenith angles for all IRHS observations are* $\sim 10°$ higher *than THIS data. In contradiction to thereby expected lower temperatures, observations yield slightly higher temperatures for IRHS data.*

with a solar maximum (see Fig. 5.9). In contrast, 2009 was a year with exceptionally low solar activity, even for a solar minimum.
To distinguish between systematical differences and solar activity reasons of the different measurements, data of other solar cycle phases have to be investigated. Indeed, there are more Venus data IRHS observed with IRHS which have to be analysed in the near future concerning temperatures. Also, more observations with THIS are planned for the future as the solar activity is increasing again.
Yet, observations with HIPWAC in 2007, also already during solar minimum do not quite fit in the picture of solar activity influence. It is obvious that more data points are needed to further constrain the solar activity hypothesis.

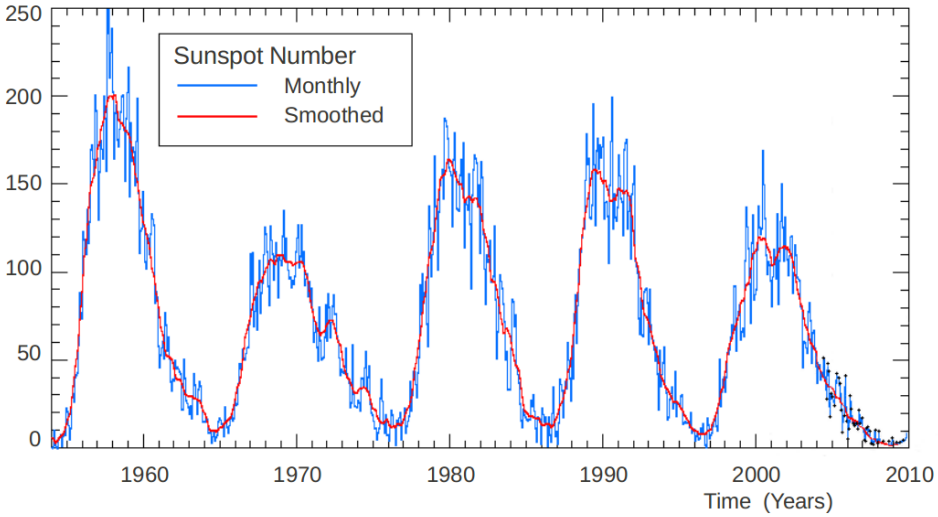

Figure 5.9: *Last 5 Solar Cycles [70]. IRHS observations in 1990/91 coincide with a solar maximum, whereas THIS and HIPWAC were observing during solar minimum in 2007 and 2009.*

5.6 Comparison to mm / sub-mm Observations

Multi-wavelength Campaign - Infrared & Sub-mm, March 2009

During the March observing run, it was possible to simultaneously observe Venus at sub-mm wavelengths. Due to different observing lengths ($\sim$10 min with THIS, 2-3 min at sub-mm) the sub-mm observations were scheduled in a loop of 5 positions on the limb, which were observed also with THIS. While this coordinated campaign was primarily targeting simultaneous observation of winds, it of course was equally interesting to investigate the results on the temperatures as well. Fig. 5.11 shows the retrieved sub-mm temperature profile with the IRHet data point for the position equator / limb. Obviously, the temperatures disagree. This can be explained by the differences in beam size of the two observing techniques. While the small FOV of infrared heterodyne observations is only seeing the sunlit crescent of Venus (and even only the warmest part of it, directly at the limb), the extended sub-mm beam is dominated by the night side of Venus as the crescent is only a small fraction of the FOV. Indeed the temperature profile agrees with profiles of the night side measured earlier [46, 35].
IRHet observations at the tip of the crescent, closer to the day/night terminator at a SZA value near 90° are moving closer to the observed sub-mm measurements as can be seen in Fig. 5.12. Given the big difference in beam size, the observations qualitatively agree very well. Still, a more detailed comparison with sub-mm data could be done for maximum elongation observations, see next paragraph.

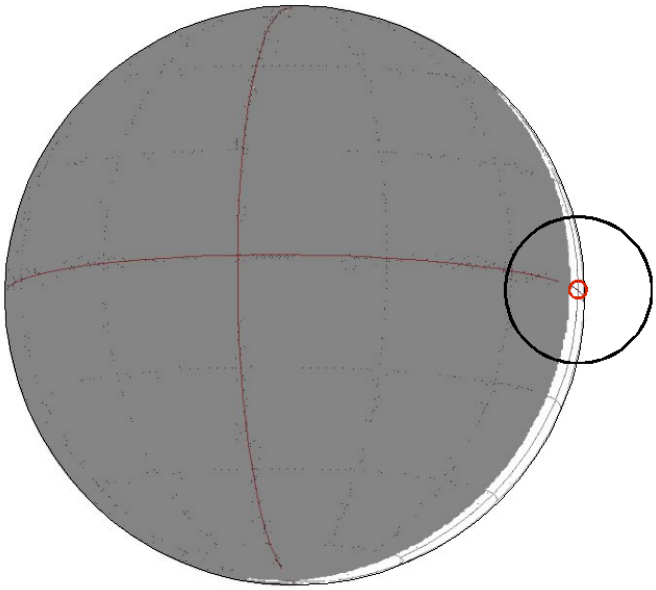

Figure 5.10: *Comparison of the beam sizes of sub-mm (black) and infrared heterodyne (red) at scale on the Venusian disc. The infrared beam is filled with the sun-lit crescent, whereas the sub-mm beam is dominated by nighttime regions.*

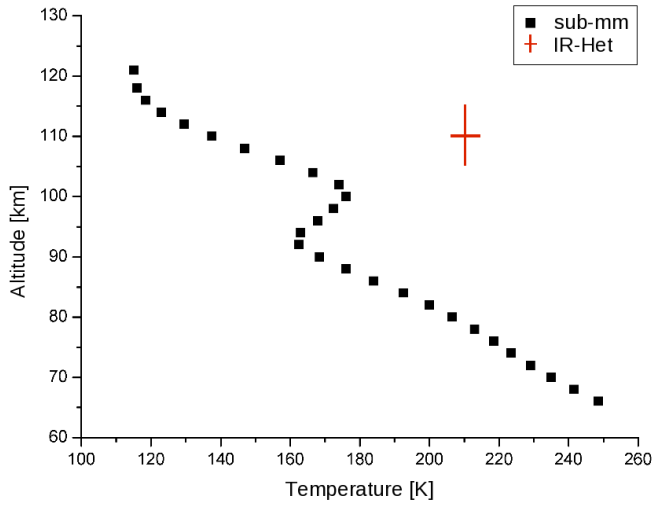

Figure 5.11: *Simultaneously observed temperatures at equator / limb using infrared heterodyne (red) and sub-mm (black) techniques, recorded March 21st 2009. Due to the big beam the sub-mm observation is dominated by nighttime temperatures, while the infrared beam is totally located on the illuminated crescent.*

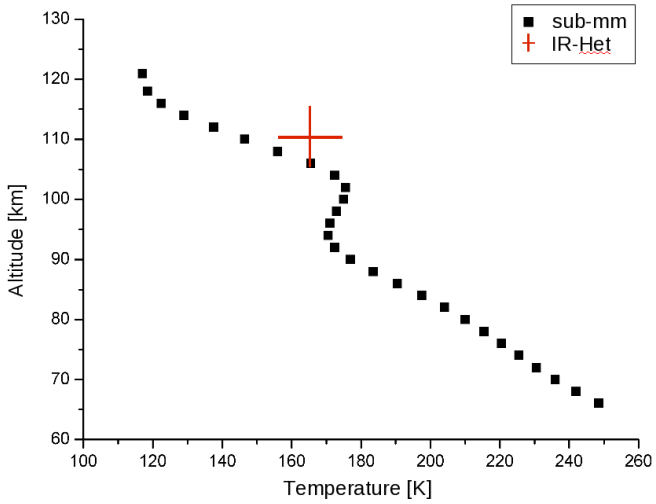

Figure 5.12: *Simultaneously observed temperatures at south pole / limb using infrared heterodyne (red) and sub-mm (black) techniques, recorded March 21st 2009. At the very tip of the crescent the difference to the nighttime dominated sub-mm observation is significantly reduced.*

Max. Elongation : Sub-mm / Infrared

The only day side observations at comparable altitudes to infrared heterodyne measurements are sub-mm observations, repeatedly done by Clancy et al. and recently also by Rengel et al. As a showcase, the June 2009 THIS data is compared to sub-mm data taken in 2007 [35]. Though this was maximum eastern elongation, so the evening terminator bisected Venus's disc, it is still a good opportunity to examine similarities and differences of both observing techniques.
In contrast to the simultaneous observations in March 2009, it was now possible to point (nearly) the whole sub-mm beam onto the illuminated hemisphere (labelled 'equator 3:30 PM' in Fig. 5.13). As a trade off, the 14 arc-second beam now fills the whole hemisphere. This is the fundamental problem when comparing sub-mm data with infrared data. As infrared observations could resolve about 70 independent points on the disc (actually observed: 34, Fig. 4.4), sub-mm observations can only give an average value derived from the whole hemisphere.

Observations of Clancy et al. give daytime temperatures from 80 up to around 105 km altitude. These profiles can be extrapolated to 110 km in order to compare them to infrared heterodyne results. Due to the different spatial resolution it is expected to observe a wide spread of infrared heterodyne temperatures around some sub-mm average which would be given by the convolution of the temperature field within the telescope field of view.

The results displayed in Fig. 5.14 are nicely agreeing with that assumption. In this plot, sub-mm observations of the dayside (red), nightside (blue) and disc-centred (green) taken on four different days in June 2007 are superimposed. Black crosses and circles indicate Pioneer Venus Orbiter observations. The black lines are earlier sub-mm measurements taken near inferior conjunction (midnight, solid) and superior conjunction (midday, dashed). At $\sim$ 115 km altitude, the infrared heterodyne results (June 2009, violet) are shown. The main features are in very good agreement: the midday line is pointing towards the highest IRHet values, IRHet terminator temperatures are near the transition from central to nightside beam in the sub-mm.

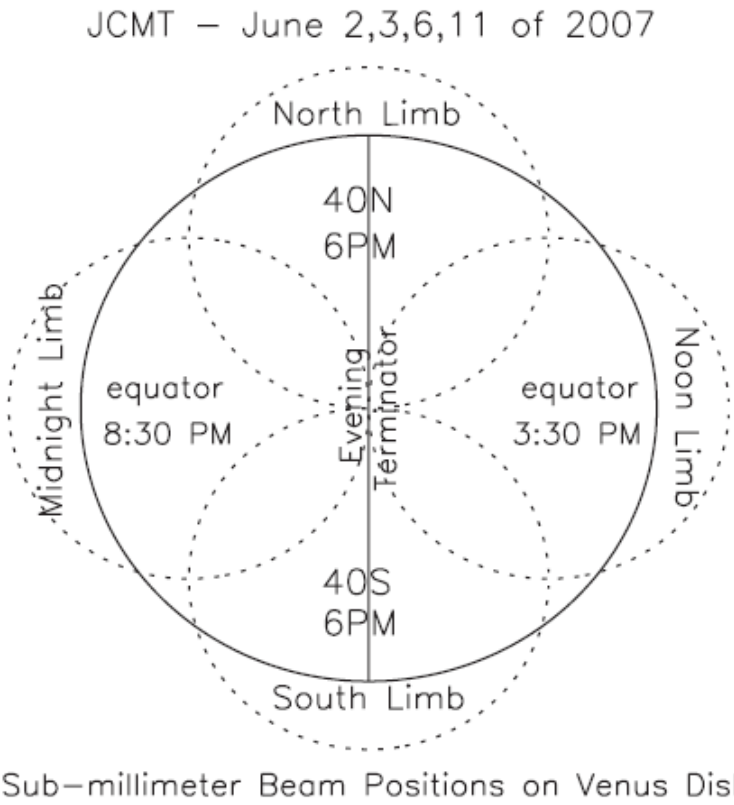

Figure 5.13: *The location of four 14 arc-seconds sub-mm beams at a half illuminated Venus disc (22-23 arc-seconds) observed June 2007 [35]. Also there are the approximate local times and latitudes for each beam position indicated.*

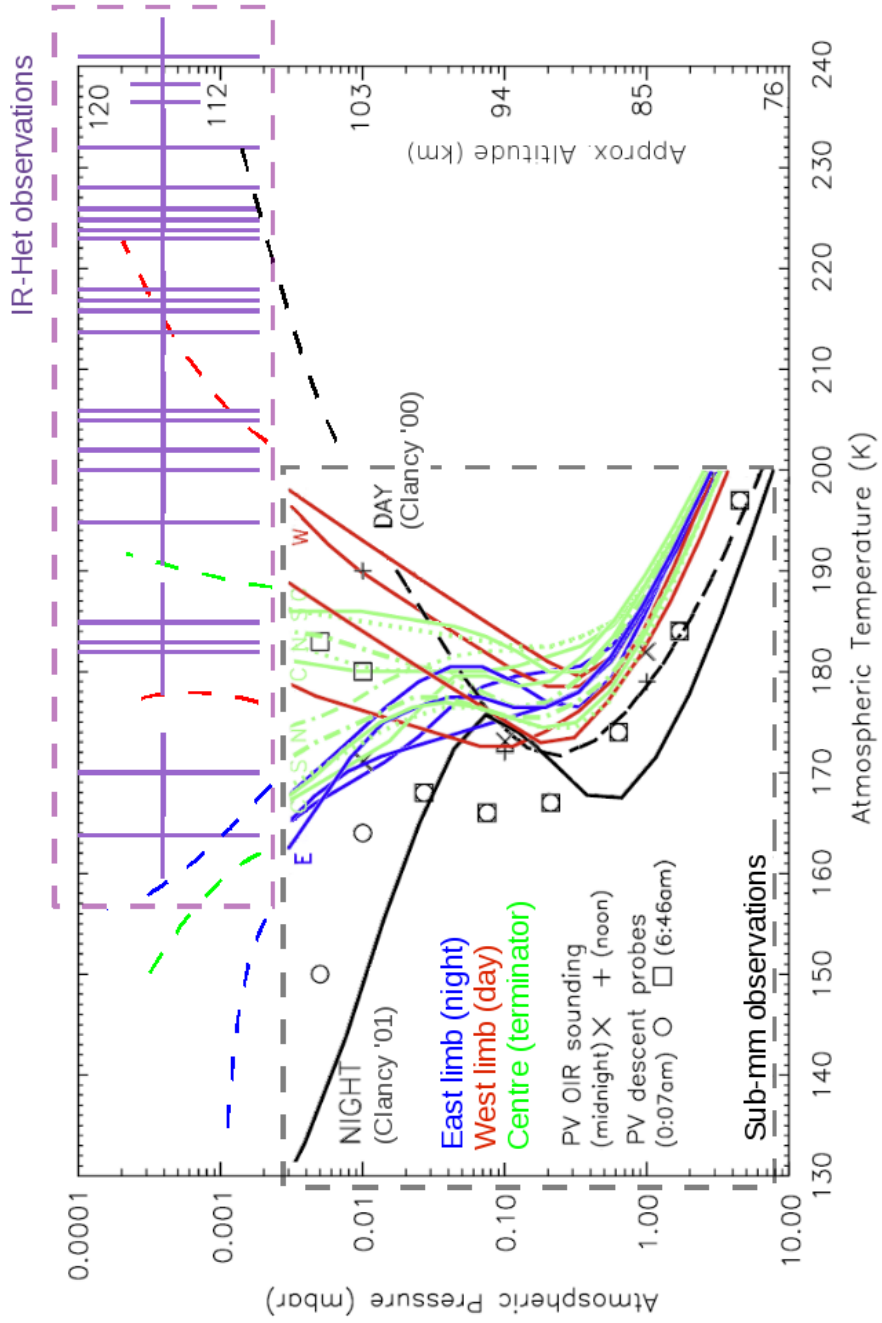

Figure 5.14: *Comparison of sub-mm (lower left) and infrared heterodyne (upper right) temperatures. Sub-mm plots shown are a superposition of all plots shown in [35]. Colours indicate observations of the day-side (red) / night-side (blue) hemisphere and the terminator (green). Observations of inferior conjunction ('Night', solid black), superior conjunction ('Day', dashed black) and from Pioneer Venus (black symbols) are also given. Infrared heterodyne observations (purple) are inserted at 115 km altitude. They fit well in the corresponding extrapolated regions (dashed coloured lines): highest values, obtained near the sub solar point agree with sub-mm superior conjunction measurements, lower values from the terminator agree with the respective sub-mm values.*

Long-term mm observations

From 1982-1990, Clancy et al. observed Venus at mm wavelength [71]. They used the NRAO Kitt Peak 11 and 12 meter antennas which lead to beam sizes of 32 to 60 arc-seconds, two to four times bigger than their later observations using the JCMT at sub-mm wavelengths. Thus, even at inferior conjunction, their beam was as big as the disc of Venus. However, they observed remarkable results. While the results for the observations taken in 1982, 1988 and 1990 correspond to the VIRA model within the observation uncertainties, temperatures in 1986 and especially 1985 were much higher, up to ∼45 K compared to the 1982 observations, see Fig. 5.15. This effect increases while rising in altitude. At 70 km, the temperature is constant during all observations the biggest differences are seen from 95 to 110 km altitude at the upper boundary of the observed altitude range.

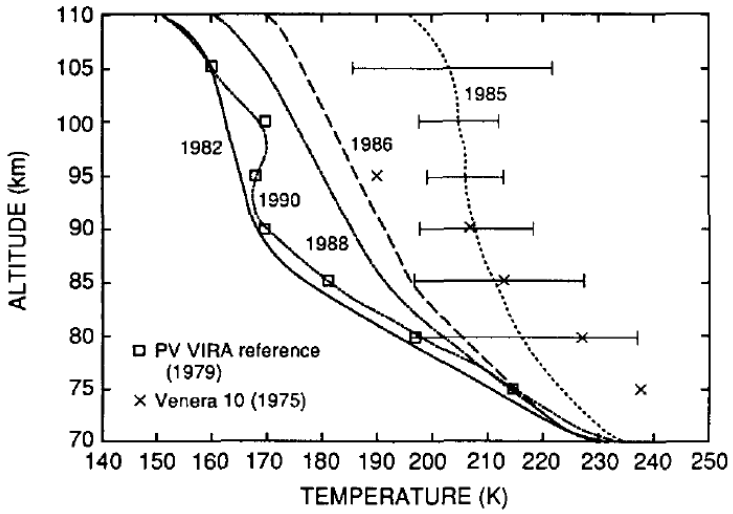

Figure 5.15: *Long-term mm observations by Clancy et al. [71]. Variations up to 45 K are seen in day side observations during 8 years.*

5.7 Comparison to model predictions

The temperature predictions of the VIRA model are given in broad global regions: day and night side are divided into three sub-regions: polar-, middle- and equatorial latitudes. In the altitude range from 100–120 km the expected temperatures reach up to 190 K and drop to 166, 172 and 175 K respectively for the three regions.
Observed temperatures in this altitude range generally are significantly higher than VIRA predictions. This is consistent with other recent ground-based and space-based observations ([45, 35], see chapter 3). Only at polar latitudes or close to the terminator and with high spatial resolution, similar temperatures are observed.
As a consequence, global circulation models which a priori start from an atmospheric structure set by VIRA will give results according to this fact.
The basic structure given by VIRA still holds: highest temperatures around the sub-solar point and a decrease proportional to SZA. But going into the details there are big differences emerging between observations and model predictions.

Fig. 5.16 shows recent results of the Imperial College London (IC) model of the temperature distribution at the equator for altitudes of 110–120 km [72]. The measured temperature data points from June 2009 are shown in black, including error bars. Assuming an emission altitude of 110–115 km, the plot suggests that the model needs to apply a steeper gradient for the temperature inversion going to higher altitudes. A model altitude of around 125 km would approximately fit the observations.

Fig. 5.17 illustrates the ICL attempt (red) to connect the VIRA model for altitudes lower than 100 km and for local times around noon with the VTS-3 model ([73], like VIRA an empirical model based on Pioneer Venus data) for the higher thermosphere. The shape of the temperature profile between those models from 10 to 10^{-3} Pa is fitted to data from sub-mm and infrared observations Again, infrared heterodyne data points are included in black (9, 10 and 12 h Venus local time). In order to fit both, sub-mm observations and VTS-3 model, the IC model features a kind of 'double inversion layer': temperatures start to cool down, just above the region probed by sub-mm, and then again steeply rise at about 130 km altitude. Infrared heterodyne observations already caused a strengthening of this double

inversion as the temperatures for midday local time are significantly higher than expected by earlier model predictions.

Fig. 5.18 displays the equatorial temperature field calculated by the VTGCM model [74]. Again, the model seems to reproduce the temperature structure shifted by approx. 10 km in altitude, and predicted temperatures are too low except for observation at the terminator. Deviations at noon reach 30 K.
The VTGCM model is primarily targeted at the thermosphere, the observed altitudes of 110 km are near the lower boundary of the model. It therefore might not be unlikely that deviations from observations occur with such a magnitude.
An interesting point here is the modelled temperature dependency with the solar cycle. Fig. 5.18 shows on the left panel the solar minimum case (with June 2009 points included at 110–115 km). On the right panel, the solar maximum case is depicted, including the results of IRHS observations. Although the colour code is unfortunately not the same, one can see a clear temperature increase at solar maximum above $\sim$135 km altitude at the day side. Temperatures at 160 km span from 230–310 K from solar minimum to maximum, a difference even more pronounced than stated in [69].

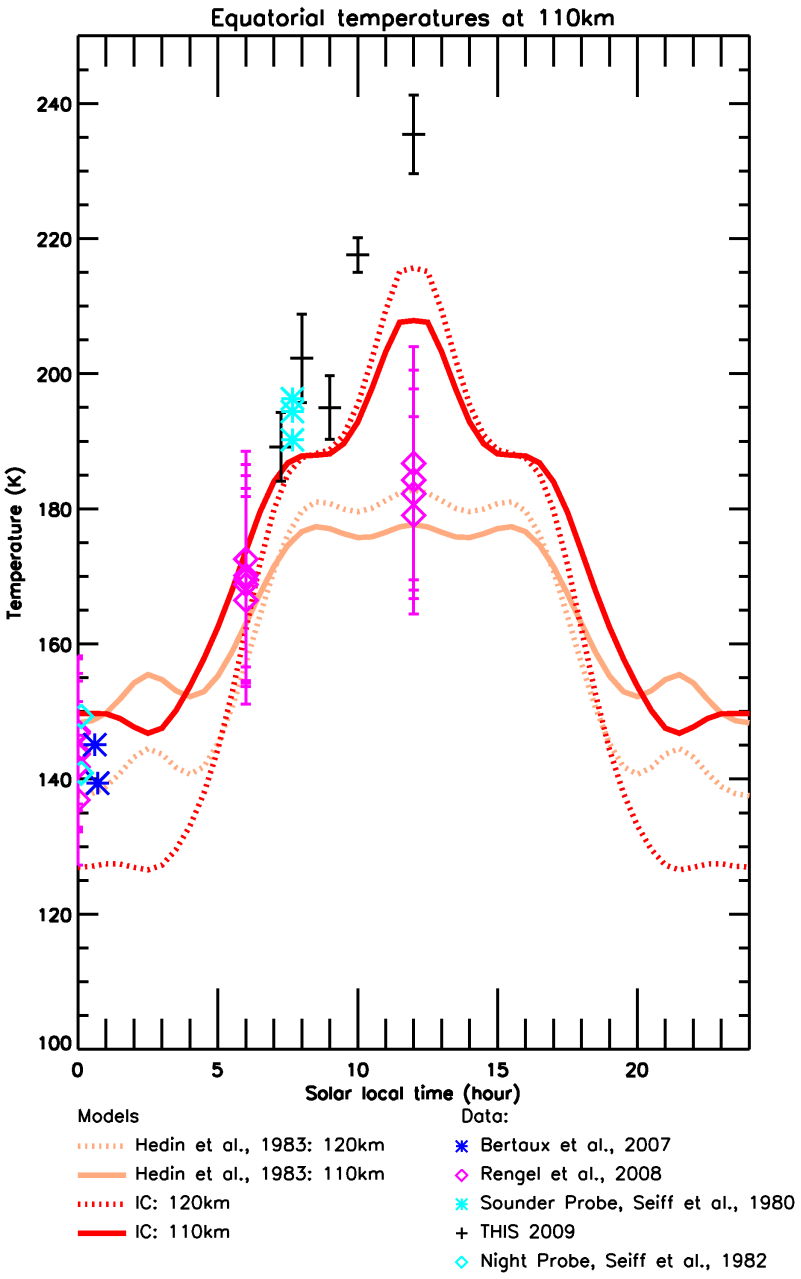

Figure 5.16: *Comparison between equatorial temperatures of the Imperial College London- (red) and the VTS-3 model (orange) and observed data as indicated. THIS observations from June 2009 are plotted in black. [72]*

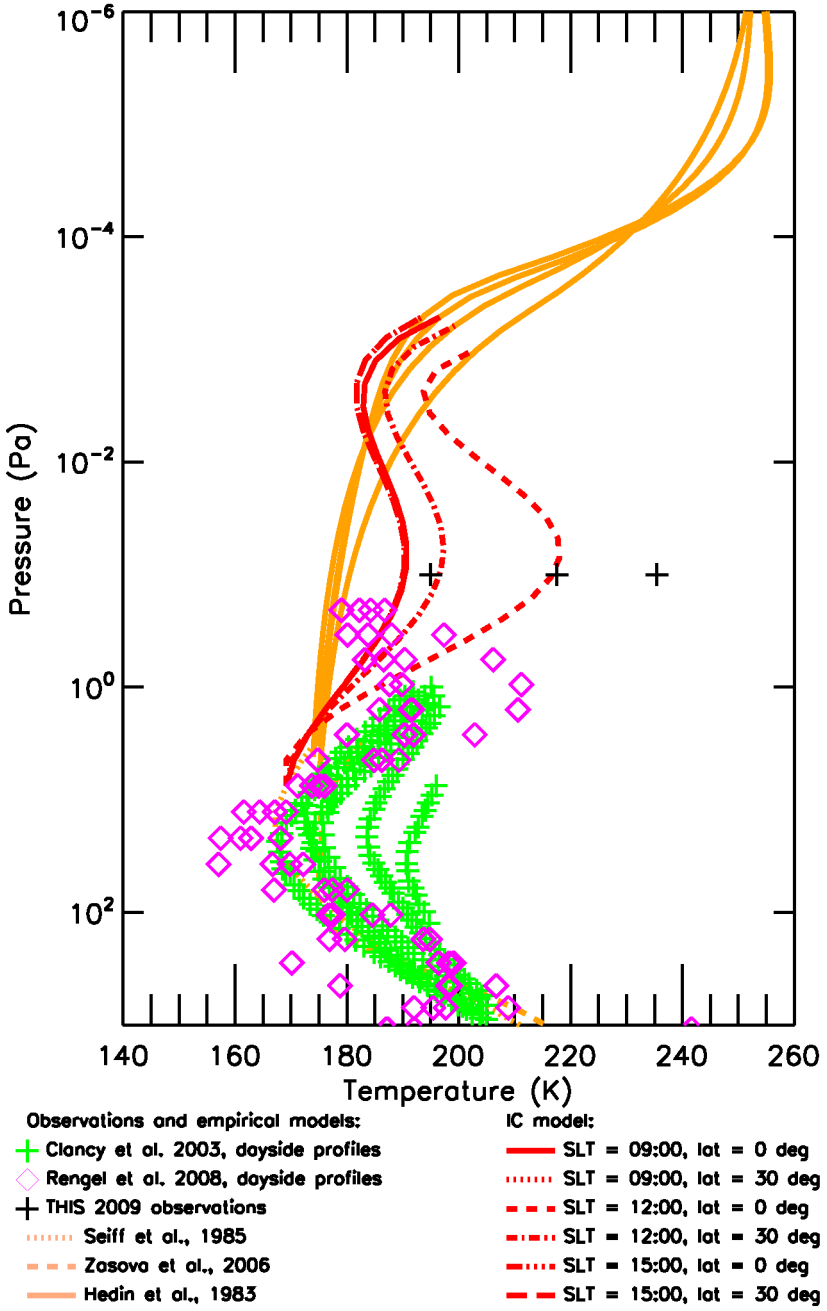

Figure 5.17: *Averaged ICL temperature profile for local times 09:00-15:00 at the equator (red) connecting VIRA for the lower atmosphere (yellow dashed/dotted) and VTS-3 for the upper atmosphere (yellow, solid)[72]. IC predictions agree with 'averaging' data like sub-mm observations by Clancy (green) but differ from IRHet observations (black, plotted are values at equator and local times 9, 10 and 12 h).*

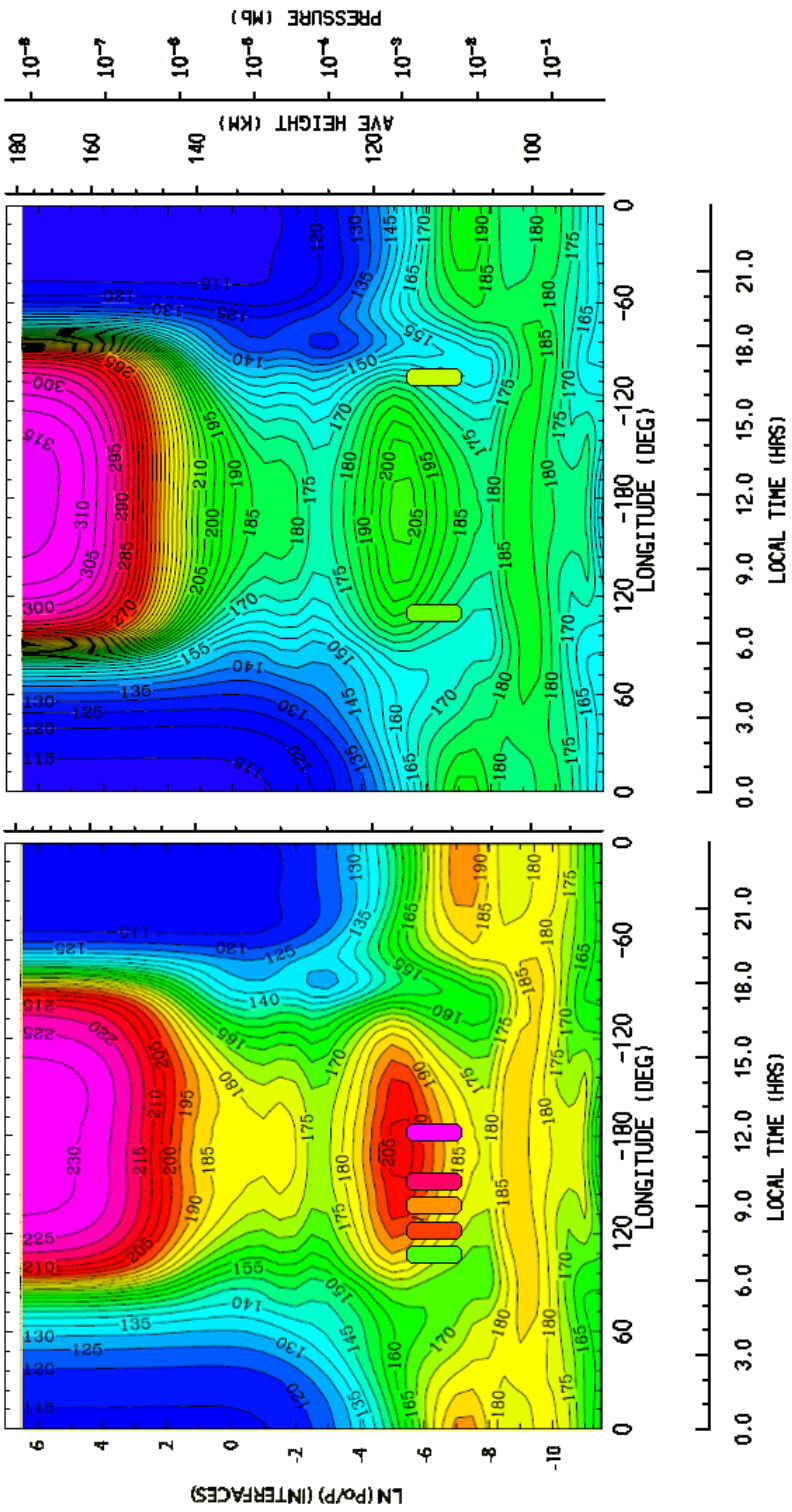

Figure 5.18: *Model for the thermosphere during solar minimum (left) and solar maximum (right) [74]. Note that colour codes are* **not** *identical! Below 130 km the model gives* **the same** *temperatures in both cases. At 110 km altitude the IRHet measurements are included in the respective colour code. (THIS June '09 values for solar minimum, IRHS mean values for solar maximum. All observations disagree with the model by ~ 40 degrees.*

5.8 Conclusions

Emission altitude

A crucial aspect in the analysis is the proper determination of the emission altitude. The assumed altitude of 110–115 km of the non-LTE emission is based on model calculations which itself uses VIRA pressure/temperature profiles. This is a somewhat unfortunate situation as temperature measurements are indicating that VIRA profiles are not the proper way to describe the atmosphere. However, as long as there are no better reference profiles, this is the 'best guess' possible. The non-LTE model needs the conditions for the whole atmosphere up to the emission altitude, so changing only the temperature in the upper boundary does not make sense. However, as there are limb sounding measurements on Venus as well as on Mars confirming the respective altitude predicted by the model, it seems that changes of the temperature do not alter the altitude of the non-LTE emitting pressure region too much.

Temperature retrieval

Obviously, the Venus International Reference Atmosphere needs to be updated again. Infrared heterodyne spectroscopy in consent to other observation techniques observed generally higher temperatures than predicted.

Variability

Measurements with infrared heterodyne spectroscopy demonstrate a high variability of Venus's mesospheric temperatures. short-term variations of up to 40 K within a few (Earth-) days were recorded. This is in agreement with other observations done with sub-mm Earth-based and near-infrared / UV space-based spectroscopy. This indicates a much more turbulent atmosphere in altitudes around 100-120 km than thought before. A reason for such turbulence can be the transition between the two global wind patterns: the superrotation in the troposphere and lower mesosphere, and the SS-AS flow in the thermosphere are basically different atmospheric regions. At some altitude the superrotation has to switch over to the SS-AS flow,

which is aligned in the opposite direction for the morning terminator hemisphere. Both wind patterns are expected to reach wind speeds in the order of 100 m/s. It therefore would not be surprising if massive turbulences would occur in the transition zone, giving rise to the observed temperature variations.

VIRA

Given the temperature variations on short time scales described above, the deviation from the VIRA model can be seen as a long-term variation. However,as observations with the PVO descent probes were so few and confined to three very small areas, it is more likely that VIRA observations themselves represent a variation of a global mean we see today using many different techniques observing nearly continuously from ground and space. Thus, a new reference atmosphere is urgently needed.

Transition Superrotation-SSAS

Whether the emission altitude of around 115 km is dynamically dominated by superrotation or the SSAS-flow is still unsolved and matter of debate today. For example, is is totally unknown where the return flow from the anti solar point back to the sub solar point is located. These questions are of course best addressed using wind measurements, e.g. [75, 76]. The 2009 THIS data-set was investigated for superrotation in June (no SSAS-component in the line of sight at the noon limb), and for SSAS winds observed at inferior conjunction in addition to the superrotation. No significant superrotation was observed.
The observed temperatures as well might suggest that the SSAS flow is already the dominating dynamical pattern at the emission altitude as the temperatures better fit to higher model altitudes.

Solar cycle influence

Long-term temperature differences can be a result of changing solar activity. While big temperature variations between solar minimum and maximum are observed in the upper thermosphere (above 160 km) this effect so far is believed to vanish below 140 km altitude.

Infrared heterodyne observations during solar maximum 1990/1991 and solar minimum 2009 hint a correlation, but more data is needed to verify this. IRHS data from 1980s and 1990s is available for re-analysis and will be subject of investigations in the near future.
Long-term observations using mm wavelength by Clancy et al. show much higher variability than the observed difference between IRHS and THIS. Also the infrared heterodyne data set demonstrates a high variability on all time scales. It therefore will be a difficult task, if not impossible at all, to search for solar cycle influence at altitudes around 115–120 km.

Chapter 6

Expanding to longer wavelengths

In this chapter, the laboratory measurements presented in chapter 7 are motivated by presenting a selection of possible targets for infrared heterodyne spectroscopy in the wavelength region from 12 to 17 micron.

6.1 Motivation: Potential for Atomic and Molecular Line Spectroscopy

The magnetic field of stars can be directly measured using the Zeeman splitting of atomic lines like the Mg I line at 12.2 μm . As investigated by using the TEXES spectrograph observing Procyon [77], the Zeeman lines can be separated if the magnetic field causes a Zeeman splitting big enough. TEXES could not detect a Zeeman splitting thus only provide an upper limit of 800 Gauss for the magnetic field strength of Procyon. Infrared Heterodyne Spectroscopy with its ultra high spectral resolution could see this separation witch much more detail and will be able to detect weaker magnetic fields.

Acetylene (C_2H_2) has its lowest transitions at around 13.5 micron. It is a very interesting molecule: it is found in the solar system, in the atmospheres of the giant gas planets as well as on Titan and in comets. It is also found in as in extra solar objects like circumplanetary discs [79]. It is especially interesting because it is a

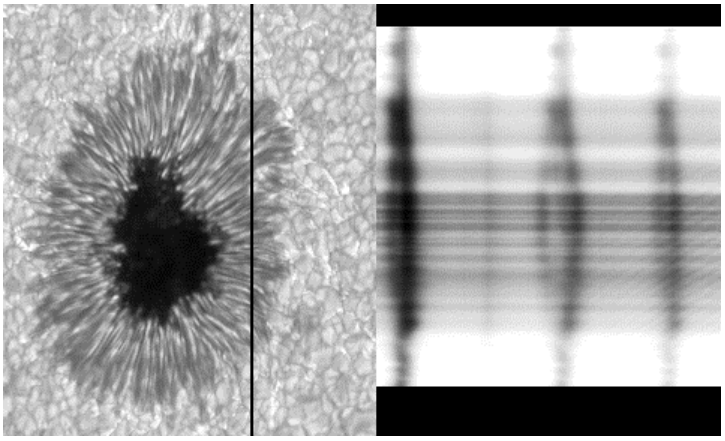

Figure 6.1: *Zeeman splitting (right) of Solar lines across a sunspot [78].*

component which can create complex organic molecules like amino acids and other precursors of proteins and DNA.

Other possible targets include Ethane (C_2H_6), Ethylene (C_2H_4), N_2O, NO_2, Ne II, CH_4 and more. For example, in circumstellar and circumplanetary discs it would be very interesting to probe different temperature regions with the respective molecule as they form in different environments.

6.2 Molecular Hydrogen

The primary target at long wavelength, at 17.035 and 28.22 μm to be precise, is molecular hydrogen. The rest of this chapter will point out its importance for astrophysics and the possible applications for infrared heterodyne spectroscopy.

6.2.1 Molecular Hydrogen in the Interstellar Medium (ISM)

Hydrogen is the most abundant element in the universe, and next to Helium (and Lithium) one of the primordial elements formed during the big bang. Formation of molecular hydrogen in the very early universe started in the recombination era, predominantly with the associative detachment process via H^- ions [80]. The bulk H_2 for-

mation, however, occurred with the collapse of the first cosmological objects, where high densities, needed for the very rare three-body collisions, were reached [81, 82]. In the evolved universe with higher metallicities, it is suggested that H_2 forms on dust grain surfaces, though this process, especially in the diffuse medium is not yet exactly understood [83, 84, 85].The formation of H_2 on grains in the interstellar medium initiates the chemistry of interstellar clouds. The H_2^+ ions produced by cosmic ray ionisation of H_2 react with H_2 to create H_3^+, detected in the late 90s in the interstellar gas by infrared absorption [86], and the H_3^+ ions participate in proton transfer reactions with neutral atoms and molecules, leading to a rich chemistry and an array of complex molecules. Molecular hydrogen is the simplest neutral molecule but it has enough complexity to serve as a probe of a variety of physical surroundings. It is the most abundant molecular species, able to survive in hostile environments and is found nearly everywhere in the universe touching most of the important questions in astronomy. H_2 is central to the evolution of the early universe and the formation of galaxies and the interstellar gas. Its chemistry controls the ionisation and thermal balance in the ISM and the mechanisms of star formation. In addition it has a higher efficiency as a coolant compared to the hydrogen atom. As its radiative and collisional properties are reasonably well understood, it is possible to obtain realistic models of the response of H_2 to its environment. Equally important to the discovery of H_2 in different environments is the possible existence of large amounts of undetected H_2. H_2 may go unseen because its standard tracer, CO, is underabundant (or frozen out) or because the gas is too cold for excitation to occur. Cold H_2 is a candidate for hidden mass or 'dark matter' in the universe, not at a level to change the global cosmological distribution of baryonic matter, dark matter and dark energy, but as contribution to the galactic baryonic dark matter [87, 88].
Because H_2 is a homo-nuclear diatomic molecule, it does not have an electric dipole moment, which means that only quadrupole transitions are allowed by which the H_2 molecule can radiate. Thus cold H_2 is invisible for radio or sub-mm observations. Hydrogen molecules have been detected in absorption and emission at ultraviolet and infrared wavelengths, but so far only in emission at lowest pure rotational transitions into the ground states of ortho ($S_0(1)$, 17.035 μm) and para-H_2 ($S_0(0)$, 28.22 μm). While most observations target hot star forming regions or photon dominated regions (PDRs), the main fraction of H_2 is situated in cold gas. It is possible to observe absorptions using the $S_0(1)$ line, although the rotational temperature

of J=1 is at $\approx$ 170 K, because the J=1 $\rightarrow$ J=0 transition is highly forbidden. In PDRs for example, the $S_0(1)$ transition is still the brightest H_2 emission line down to 100 K, and only below 30 K nearly all H_2 will exist in the para state [89]. Consequently, future observations of the $S_0(0)$ absorption with SOFIA (see chapter **??**) will then probe all of the cold molecular hydrogen. However, already the $S_0(1)$ line alone will return a variety of scientific output on its own and does not need extended preparatory work as all hardware components are already developed and available.

6.2.2 Cold H_2 from CO

Lacking the ability to directly observe H_2, it is common to use tracer molecules to deduce abundances of H_2. For example carbon monoxide (CO), being the second most abundant molecule in space ($\sim 10^{-4}$ relative to H_2) and easy to observe due to its low excitation energy. Therefore it is used to map the molecular hydrogen in the universe [90]. The CO molecules do exchange energy with the H_2 molecules by collisions and hence the low-j transitions are often in a thermodynamic equilibrium with H_2. The excitation energy of the lowest rotational transition at 115 GHz (2.6 mm) is small ($\sim$ 5 K), so it is easy to observe their emission lines at radio wavelengths. However, this scenario is severely oversimplified. There are many different CO/H_2 ratios for different environments, and many times it fails to explain the observed data as different environments show variable abundances of both molecules and the ratio might be dependent on the metallicity and the radiation field [91, 92, 93, 94].

6.2.3 Star Formation and Protoplanetary Discs

Being the most abundant species in molecular clouds, H_2 is crucial for star formation. Its dissociation enables the final collapse to the stellar core [95]. Therefore it is also dominant in circumstellar discs and in the formation of planets [96]. However, most data on circumstellar discs were acquired observing the dust within the disc as it is more easily done, e.g. with the Spitzer satellite [97]. Models often assume temperatures of gas and dust to be equal, but at low densities the gas will thermally decouple from the dust. More detailed information about the gas in discs is required to strengthen the models with respect to disc mass or planetary formation processes. The

characteristics of the forming planets, particularly giant planets, are directly tied to the evolution of the gas content in the disk. The presence of planets may lead to the opening-up of a gap that stops further accretion onto the star. Conversely, the energetic processes accompanying star formation in the form of jets and winds have a profound influence on the evolution of the circumstellar disk, and may halt planet formation. Recently, H_2 has been detected in circumstellar discs with TEXES [98] and Spitzer [99], while using VISIR resulted in both, detection [100] and non-detection[101]. Heterodyne observations will provide the higher spectral resolution necessary for example to address the dependency of the dynamics or the chemical composition on the radial distance to the star.

6.2.4 Molecular Hydrogen in Planetary Atmospheres

Molecular hydrogen is the main component of the giant planets [102, 103], but was also detected for example in the atmosphere of Mars [104]. In the inner core of Jupiter and Saturn, H_2 is highly compressed, forming metallic hydrogen [105, 106]. The inner structure, however, is poorly known [107]. It was suggested by Vorontsov et al. [108] that Jupiter might oscillate similar to the sun. Oscillations were measured by Schmider and Mosser [109, 110] in the troposphere of Jupiter. Observations of giant planet acoustic oscillations are a powerful tool for inferring the internal structure, like the radius of the planetary core or the localisation of the level where the transition of molecular to metallic molecular hydrogen occurs [111]. Infrared Heterodyne Spectroscopy can provide the high resolution needed for observations of planetary oscillations [110]. With its bright $S_0(1)$ line [110], Jupiter will also serve as an ideal testbed for later observations of dimmer targets.
On Mars, observations of H_2 agree with the models of hydrodynamic escape and support the implication of once existing oceans on Mars. THIS [58] was already used successfully to measure planetary atmospheric dynamics on Mars [58] and Venus with ultra high spectral resolution equal to a few m/s [23]. This is exactly the resolution needed for the search for Jovian oscillations.
Furthermore, high resolution observations of molecular hydrogen will provide detailed temperature profiles of the stratospheres of the outer planets, again also on Jupiter but especially Uranus and Neptune. Unlike Jupiter and Saturn where the strong 7-μm band of methane allows for sensing of the stratosphere, Uranus and Nep-

tune have no well mixed atmospheric component in the thermal infrared other than H_2 [112, 113]. [112] detected H_2 with IRSHELL at a spectral resolution of $\approx 10^4$. Higher resolution provided by infrared heterodyne spectroscopy could fully resolve the lines, and vertical temperature profiles can be deduced using the BEAMINT radiative transfer code supplied by our collaborators at NASA/GSFC [114]. Also models of H_2-H_2 collision-induced absorption [115] can be tested. With THIS we deduced height profiles of Ozone in the Earth's atmosphere and measured temperatures of SiO and H_2O molecules in sunspots [116].

6.2.5 H_2 Observations

Much information about H_2 has been gathered by space missions during the last decade with the satellites ISO [117] (for reviews of ISO H_2 science see [118, 83]), FUSE [119] and SPITZER [120]. It was also studied by its X-ray absorption with CHANDRA [121]. In the infrared, ISO and SPITZER have detected H_2 emission lines, while FUSE did mostly observe UV absorptions. H_2 targets of ISO and SPITZER have been star forming regions and circumstellar environments of young stellar objects [91, 122, 99], PDRs, where formation rates and the ortho-to-para ratio could be measured [123, 124, 125], shocks [124, 99], links to dust and polycyclic aromatic hydrocarbons (PAHs) [118] and finally the observation of extragalactic sources [126, 127]. FUSE observations include circumstellar discs [92], Planets and Comets (emission lines) [104, 128] and the galactic and extragalactic ISM [129, 130]. It was possible for the first time to study the whole series of pure rotational H_2 transitions. In this way, the interesting transition regions of the interstellar medium, separating neutral and ionised gas could be probed for their temperatures and densities. Also, formation rates of H_2 and the possibility of formation on PAHs or very small grains was suggested. H_2 lines turned out to be a valuable tool to examine shock environments, for example to estimate the age of the shock. In the field of star formation, new knowledge was obtained about excitation mechanisms at different evolutionary stages of young stellar objects. However, all these missions do lack spectral resolution compared to ground based facilities. To get the kinematic information and reduce line blending effects resolutions higher than 10^4 are necessary.
Ground-based observations at high spectral resolution in the mid-

infrared were done with grating spectrographs like CSHELL [131] and TEXES [22, 132, 133, 134], which observed low vibrational transitions in absorption and pure rotational line emission of the $S_0(1)$ line at 17.035 μm. IRSHELL [112] observed H_2 in the atmosphere of Neptune.
With THIS, first direct measurements of the abundance and the distribution of H_2 will be possible. With the ultra-high resolution of heterodyne spectroscopy, we will get detailed kinematic information on the environment of the studied gas. Furthermore, the three-dimensional structure along the line of sight can be deduced. It will also probe models of protoplanetary discs [135] to see how the gas is separated from the known dust distribution.
Together with future observations of the $S_0(0)$ line at 28 μm it will be possible to determine the temperature distribution of the H_2 formed in the interstellar medium. 28 μm will be observed from the airborne infrared observatory SOFIA.

Table 6.1: *THIS sensitivity characteristics at 17 μm wavelength.*

Wavelength	Bandwidth	Resolution	sensitivity (8m mirror)
17 μm	50 km/s	1 km/s	0.3 Jy/hour
17 μm	50 km/s	100 m/s	1 Jy/hour
17 μm	50 km/s	10 m/s	3 Jy/hour

6.3 Preliminary Work - Astronomy

The spectrometer THIS has been used successfully on various observation runs in the past. High precision determination of atmospheric dynamics on Mars and Venus were done as well as investigations of molecular features in sunspots and the telluric atmosphere.
A first proof of concept for detecting extrasolar signals with THIS was done in 2003 at the McMath-Pierce Solar Telescope on Kitt Peak/Az, USA (1.5 m mirror). Similar to the observations planed, an absorption feature was measured against a hot background source, in that case telluric ozone against the continuum radiation of Alpha Orionis (Betelgeuse). The spectrum shown in figure 6.2 is a 20 min observation of an Ozone line at 9.635 μm . From a sky-dip

measurement - solar flux vs. zenith angle - a coupling efficiency between telescope and spectrometer of 55 % and an atmospheric transmission of 18 % was deduced. At 9.6 μm, the brightness temperature difference between sky and Betelgeuse is 2913 K [136]. Scaled with a beam filling factor of $2.4 \cdot 10^{-3}$ and the coupling efficiency to the telescope, a mean background temperature of 692 mK was expected, in agreement with the measurement. Calculated backwards to the sensitivity of THIS with respect to background sources, we find similar sensitivities than shown in table 1. This indicates the excellent capabilities of the spectrometer THIS, which are promising to detect absorption of the $S_0(1)$ line for the first time.

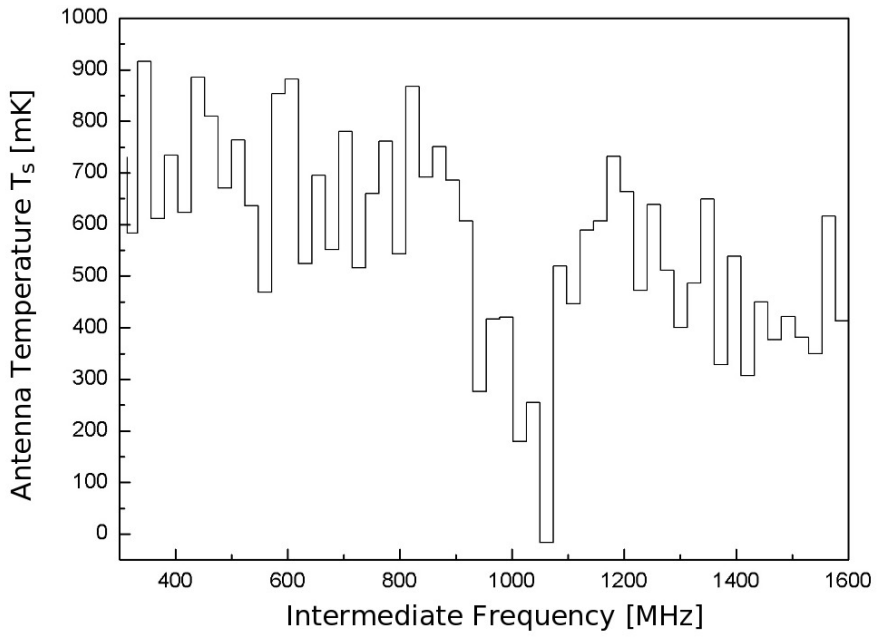

Figure 6.2: *Telluric Ozone Absorption against Betelgeuse [137].*

Chapter 7

Laboratory Measurements

To expand the coverage of THIS towards longer wavelengths, one needs three new fundamental components: a local oscillator working at the desired frequency, appropriate optics like dewar windows and diplexer beamsplitters and a fast detector with high sensitivity. In this chapter the laboratory measurements to evaluate possible solutions for all three components are presented.

7.1 Test setup for 17 μm

Most optical parts used in THIS are independent of the used wavelengths like flat or off-axis focusing mirrors. For dewar windows and diplexer beamsplitters, optics made of KRS-5 (a thallium salt: 58 mol% TlJ, 42 mol% TlBr) were chosen. In contrast to zinc selenide KRS-5 extends a good optical transmission up to $\sim$40 μm , see Fig. 7.1. This will make it also a good optical material for possible future observations of molecular hydrogen at 28 micron.
There were some problems in the coating process, as the company was not used to such thick coatings (which tend to detach quite easily). The transmission of the obtained windows were measured together with a ZnSe window for reference (Fig. 7.2). The transmission for the coated KRS-5 was specified to >85 % by the manufacturer.

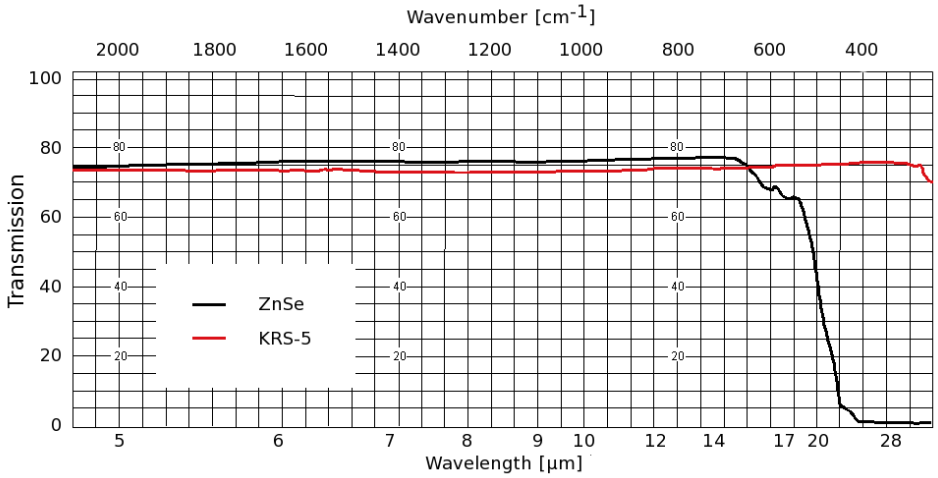

Figure 7.1: *Transmission curves of the used optics materials. ZnSe (black), the standard material in the mid infrared can be used up to ∼ 15 /mm (670 cm^{-1}). KRS-5 (red) extends a good transmission up to 40 µm . [138]*

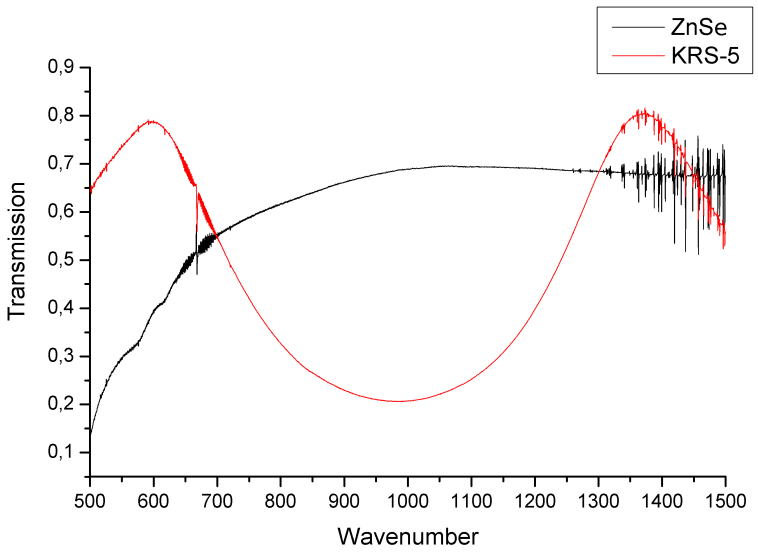

Figure 7.2: *Transmission curves measured with a Fourier Transform spectrometer (uncalibrated). The KRS-5 was coated for optimal transmission at 17 micron (588 cm^{-1}). CO_2 (670 cm^{-1}) and water absorption bands are clearly visible.*

7.1.1 The pulsed 17 μm test-Laser

For testing purposes we received a pulsed QCL provided by the group of Prof. Jerome Faist, University of Neuchatel (now ETH Zuerich). This device is centred around 17 μm with liquid nitrogen operation at 16.9 micron (Fig. 7.3). In contrast to the normally used continuous wave (cw) QCLs, pulsed lasers need a different power control approach. Two power supplies were used together with a pulse generator and a FET circuit to feed the laser with short ($\sim$100 ns) pulses via a low impedance line.

Unfortunately, the design of a cw-QCL at the required wavelength (17.035 μm) was not fitting in the projects and to the manpower available at the University of Neuchatel. However, with QCLs becoming more and more commercially available, companies are confident to design and manufacture a QCL with the desired characteristics at reasonable prices [139].

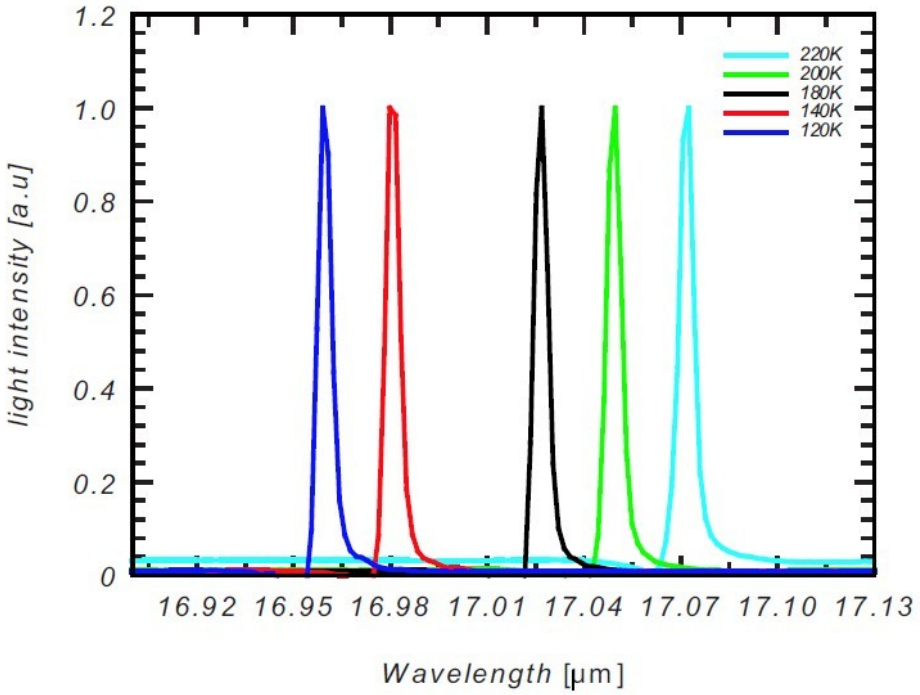

Figure 7.3: *Emission wavelength of the pulsed test device at different operating temperatures. At 77 K an wavelength of $\sim$16.9 μm is obtained. [140]*

7.2 Detectors

The biggest task in the extension of the wavelength coverage is the question about the appropriate detector. While the optics are more or less wavelength independent or can adapted quite easily, and the development of quantum cascade lasers is still increasing, the detector question remains a topic of research. In this work, two possible detectors are investigated for their ability to be implemented in THIS. In the following, I will describe the laboratory test measurements done with a Mercury-Cadmium-Telluride Photodiode (MCT), as in use in the 10 μm setup) and a newly developed Quantum Cascade Detector (QCD).

7.3 Mercury-Cadmium-Telluride Photodiode

Property	*HgTe*	$Hg_{1-x}Cd_xTe$						*CdTe*
x	0	0.194	0.205	0.225	0.31	0.44	0.62	1.0
a (Å)	6.461	6.464	6.464	6.464	6.465	6.468	6.472	6.481
T (K)	77	77	77	77	140	200	250	300
E_G (eV)	−0.261	0.073	0.091	0.123	0.272	0.474	0.749	1.490
λ_{CO} (μm)		16.9	13.6	10.1	4.6	2.6	1.7	0.8

Figure 7.4: *Dependence of MCT cutoff-wavelength (λ_{CO}) with alloy composition x [141]. Reducing the Tellurium/Mercury ratio increases the cutoff-wavelengths. Other observables given are lattice constant a, energy band gap E_G*

Mercury-Cadmium-Telluride photo diodes (MCT) are standard infrared detectors. However, it is not self-evident that these detectors are fast enough and capable to cover the required bandwidth specification of some GHz. Even in the commercially well developed wavelength region around 10 μm , it is not easy to obtain a MCT detector for heterodyne applications. With prices around 50 kUSD at this wavelength region, the rate increases by at least one order of magnitude when going to 'exotic' wavelength regions like 17 micron. HgCdTe detectors are semiconductor diodes. The actual detector is a thin HgCdTe layer defining the active area. Photons with $h \cdot \nu$ greater than the band gap of the semiconductor excite electrons into the conduction band, increasing the conductivity of the chip.

To obtain the change in conductivity, a bias current is required. The wavelength of maximum response is dependent an the band gap, which can be varied by altering the relative composition of the alloy. Reducing the Cadmium fraction increases the responsivity for longer wavelength [141], see Fig. 7.4.

Judson MCT For alignment purposes and as a power reference, a Judson J15D22 (from now on named JMCT) was used. This JMCT detector has a maximum sensitivity at 16-17 micron and a cut off wavelength of 22 micron (Fig. 7.5). It is not fast enough to serve as a heterodyne mixer/detector (see Fig. 7.7) but can be used to compare the output power of the used QCLs. Figure 7.5 shows the functions for the specific detectivity D*, which is equal to the inverse noise equivalent power (NEP) normalised to unit area and unit bandwidth.

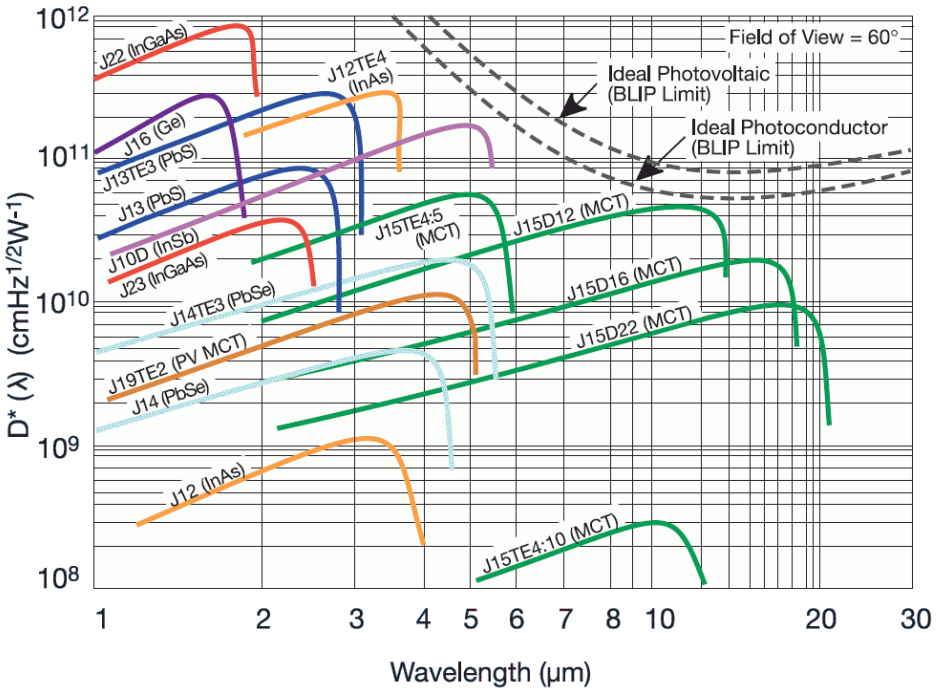

Figure 7.5: *Detectivity for Judson infrared detectors. J15D22 was used to compare the output power of different QCLs from 10 to 17 micron*

The THIS - MCT

The detector used in THIS since 2005 is a four pixel MCT built by Raytheon Vision Systems. Its operating temperature is 77 K. Each pixel is equipped with an integrated grating structure to optimise the response for a certain wavelength region (see Fig. 7.6. Thanks to these structures, very high quantum efficiencies are possible, in our case up to 81% at 10.7 μm , a similar detector used by our colleagues at NASA GSFC even reaches 89% quantum efficiency. These are outstanding good values. As a drawback, due to the gratings, the responsivity sharply drops for wavelengths longer than 11 μm . Because of this reason, for the measurements investigated in this chapter the detector used previously for THIS, also from Raytheon (therefore now: RMCT), was used. This RMCT has no grating structure applied and is therefore well suited to test the spectral responsivity at liquid helium temperatures.

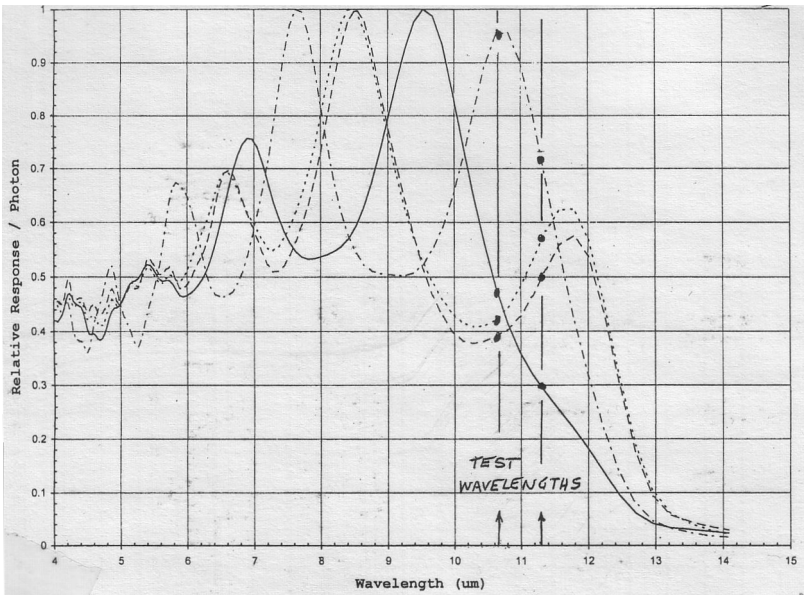

Figure 7.6: *Currently used MCT detector in THIS. The four pixels are equipped with integrated gratings to optimally cover the wavelength region from 7.5 – 11 micron.*

7.3.1 MCTs at 4 K

The RMCT is designed for optimum operation at 10 micron at liquid nitrogen temperature. As can be seen in Fig. 7.9, the cut-off wavelength, where thermal noise becomes dominant is significantly depending on the operating temperature, cooling shifts the curve upward to longer wavelengths. Detectors with a cut-off at 12 μm at 77 K possess a cut-off at 7 μm at room temperature.
The question to be investigated was how much this curve is furthermore shifted upward if the detector is cooled to liquid helium temperatures (4.2 K). For this experiment, the detector was illuminated with three lasers at different wavelengths at 9.2, 13.2 and 16.9 μm , and the response was captured while the detector temperature was increased.
However, there was no absolute calibration possible. The laser power was recorded with a power meter and the JMCT as well to estimate the relative responses. All values are shown in table 7.1. The 17 μm laser reached up to 170 µW on the power meter. At 50 kHz pulse repetition and about 200 ns pulse length this corresponds to 17 mW cw (continuous wave) operation. With the 9 and 13 μm lasers, 15 and 2.3 mW were obtained. The absorption of the power meter is the same for all used wavelengths (see Fig. 7.8), so these values give a reference for the measured responses of the two MCTs. The JMCT should have a similar detectivity at 13 and 17 μm (Fig. 7.5). The values given in table 7.1 are given assuming a boxcar function for the 17 μm pulse. The obtained pulse signal is integrated and converted into a rectangle with the width of the voltage pulse applied to the laser.

λ [μm]	power meter [mW]	JMCT [V]	RMCT [mA]
9.2	19	20	0.97
13.2	2.3	24	0.8
17	17	9.75	0.8

Table 7.1: *Response of the Raytheon MCT at 4 K compared to the Judson MCT and a power meter. The 17 μm power meter value is extrapolated from integrated pulsed readings.*

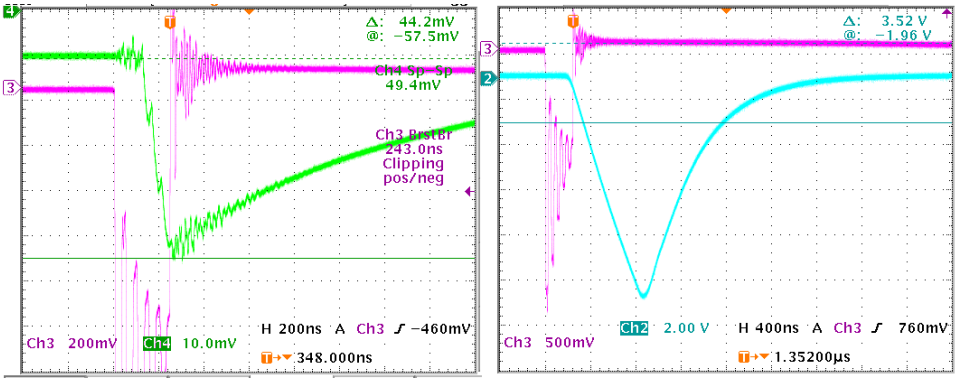

Figure 7.7: *Different responses to the pulsed 17–µm laser (laser voltage, red). The RMCT (left, green) is much faster than the Judson-MCT (right, blue). It can be seen that it takes some time until the lasing process is triggered. As soon as the voltage pulse stops, the RMCT sees a declining signal, possibly real due to the lifetime of excited electrons in the QCL. The same pulse seen with the JMCT is obviously broadened and retarded.*

Yet, it is not clear if this is overestimating the response. The problem is shown in Fig. 7.7. Here, the response to the 17 μm laser is illustrated for the RMCT (left) and the JMCT (right). It can be seen that the RMCT reacts much faster than the JMCT. The emission is seen retarded from the voltage pulse, probably due to the non-ideal pulse flank. Then the rise in the detected signal stops simultaneously with the voltage pulse. However, the signal is not dropping fast, but it seems that the lasing is slowly decaying while the conduction band electrons 'spill out'. The FWHM of $\sim$1 µs, on the other hand is much too long compared to the computed sub-ps upper state lifetimes [142] and to the pulses measured in Neuchatel (Fig. 7.18). As the RMCT has a bandwidth of some GHz, it can resolve features of 1 ns or less. It therefore seems to be a real broadening of the laser pulse, arising probably also from the non-ideal laser drive control.

The resistance of the RMCT changed with temperature from 50 to 200 Ohm, see Fig. 7.10. The obtained detector responses in Volt were convolved with the retrieved resistance function to derive the detector current, see Figs. 7.11–7.13. The drop in sensitivity below $\sim$20 K might be due to errors in measuring the fast gradient change of the resistance.
Unfortunately, the used 10 μm laser was difficult to focus onto the detector. This may originate in a worse beam profile or a signif-

icantly higher divergence of the laser. The result are comparable results at 4 K, where a much higher signal of the 10 μm laser was expected due to the detector characteristics and the high output power of the laser. Even taking into account those uncertainties, it is promising to get comparable results for all three lasers at the peak at 20 K. This suggests that efficient heterodyne detection at 17 μm wavelength might be possible at 20 K.
At 13 μm , heterodyne observations might be also feasible at liquid nitrogen temperatures as the response gradient is only slightly worse than at 9 μm . Definite conclusions, however, are subject to future investigations.

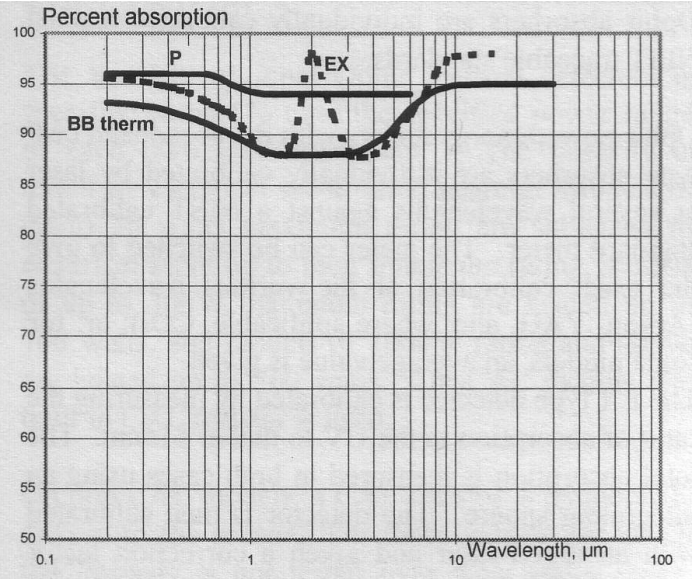

Figure 7.8: *Absorption vs. wavelength from the power meter manual. The broad band absorber (BB) shows a wavelength independent curve above 9 μm .*

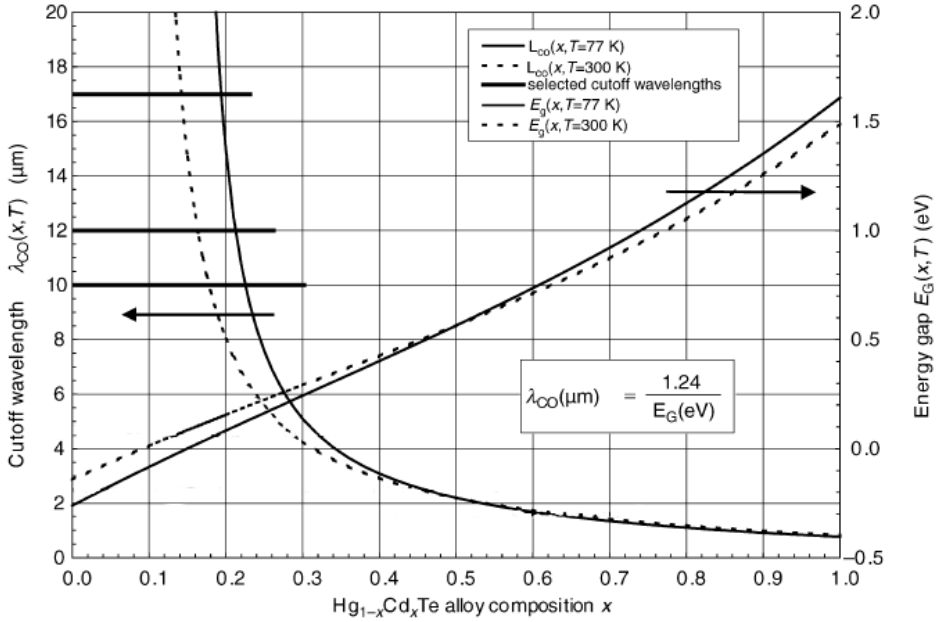

Figure 7.9: *Temperature dependence for MCT detectors by [141]. Cooling reduces thermal noise and shifts the detector cutoff towards longer wavelengths.*

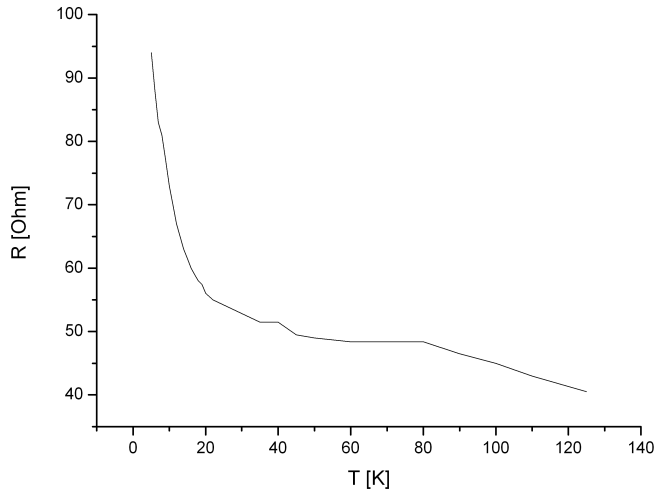

Figure 7.10: *Temperature dependency of the resistance of the RMCT.*

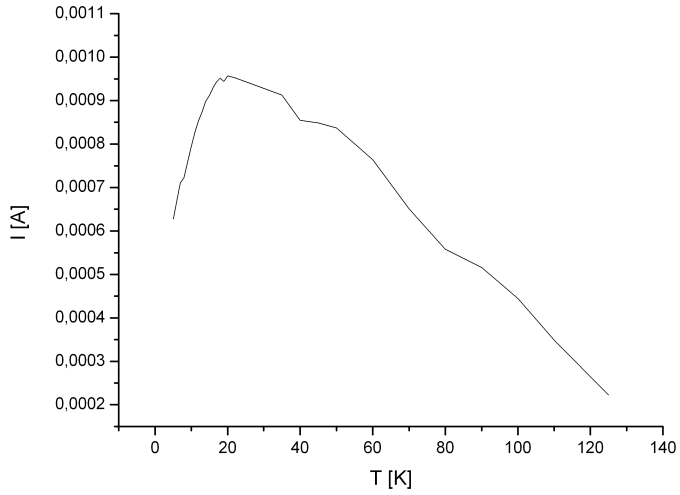

Figure 7.11: *Measured detector current versus temperature using a 9.2 µm FP-QCL*

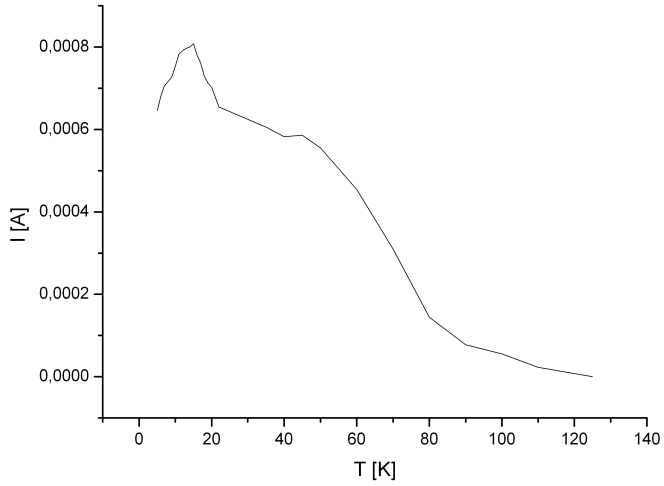

Figure 7.12: *Measured detector current versus temperature using a 13.2 µm DFB-QCL*

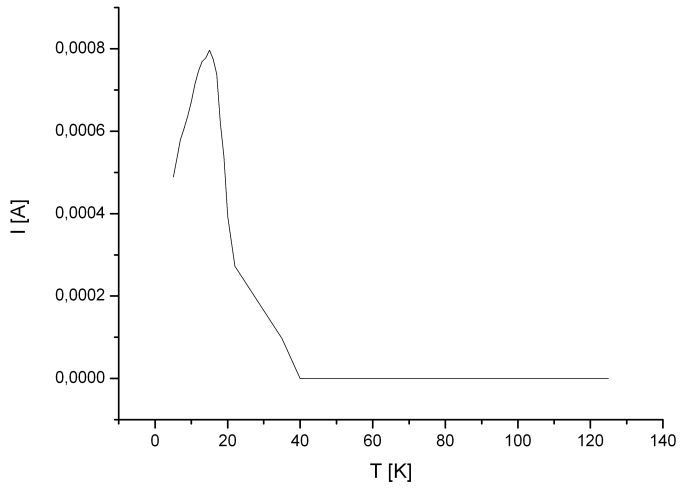

Figure 7.13: *Integrated detector current during 250 ns pulses at 17 μm*

7.4 Quantum Cascade Detector

Quantum Cascade Photodetectors (QCDs) are a very new development, evolving out of the increasing research on quantum cascade lasers (QCLs) [143, 144, 145]. In principle, a QCD works like an inverse QCL. In contrast to a Quantum well infrared photodetector (QWIP) there is no need to apply a bias electric field to a multiple quantum well hetero-structure in order to ionise the quantum wells and collect the photocurrent (see Fig. 7.14. Therefore a QCD has no dark current. In a QCD electrons are carried from their fundamental state to the next period through a cascade of quantum wells. The quantum structure is designed to generate an electronic displacement through a cascade of quantum levels when the device is illuminated. The structure consists of a succession of N coupled quantum wells. The first well is n-doped in order to populate its first level of energy in the conduction band. The absorption of an electron transfers an electron from the first to higher levels. Due to coupling between the the quantum wells, the wave function of the excited state is delocalised over the first two quantum wells. Phonon emission brings the electron in a lower level, which is delocalised to the following quantum well and so on. So the charge is transferred over a discrete distance if the detector is illuminated. This leads to a significant potential difference. The last well is then identical to the first one and the unit can be repeated to increase the potential difference. The result is a photocurrent without any bias.

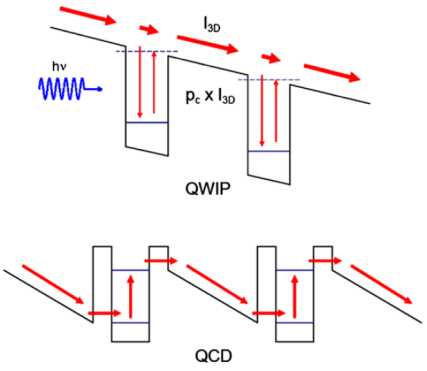

Figure 7.14: *Schematic comparison of a QWIP and a QCD. In the QWIP, electron transport in the conduction band is accomplished by an external voltage bias whereas in a QCD, an internal potential ramp ensures the carrier transport [145].*

During this work a QCD was tested in collaboration with the University of Neuchatel (Switzerland) [146]. They provided a pulsed laser at 17 μm [142, 140] and a QCD optimised for 16.5 μm wavelength. The actual mounting was realised on top of a SMA adapter where the QCD chip was glued and bonded to, see Fig. 7.15. As it can be seen, light has to illuminate the QCD under an oblique angle in this case 45 degrees. This is due to polarisation constraints, only the electric field component perpendicular to the quantum well layers interacts with the transitions used in the QCD. This geometry constraint is used to create a multi-pass waveguide configuration (Fig. 7.16). Light gets reflected internally in the waveguide and thus passes the active region repeatedly.

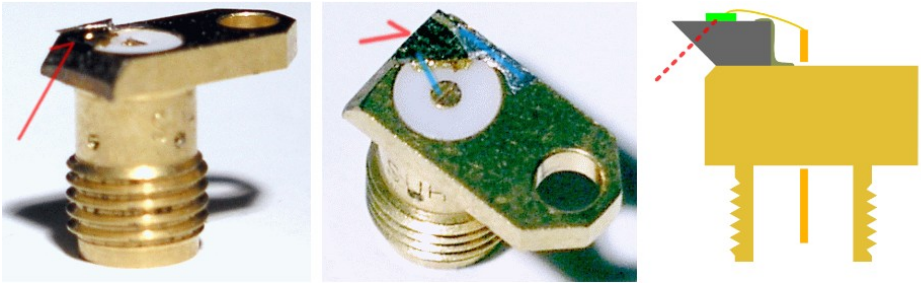

Figure 7.15: *Quantum Cascade Detector mounted on a SMA adapter*

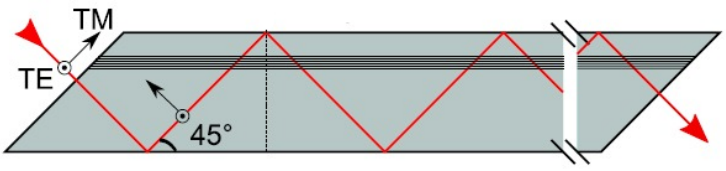

Figure 7.16: *Due to polarisation constraints a QCD has to be illuminated under an oblique angle. With a 45 degree design it is possible to pass repeatedly the active zone, thus enhancing the signal strength [147].*

In a first experiment the responsivity was measured using the QCD as detector in a Fourier Transform infrared spectrometer with a 1460°C globar and a KBr beamsplitter [147]. The resulting responsivity for two different substrate growth processes is shown in Fig. 7.17. It peaks at 610 cm^{-1} or 16.4 μm . At 10 K, the responsivity is measured to be 3.7 mA/W, with a drop of ∼50% at 16.9 μm , the emitting wavelength of the pulsed test laser. Compared to MCTs currently used with THIS with responsivities of up to 8 A/W (at 10 μm wavelength), there is a lack of three orders of magnitude in the responsivity of this quantum cascade detector.

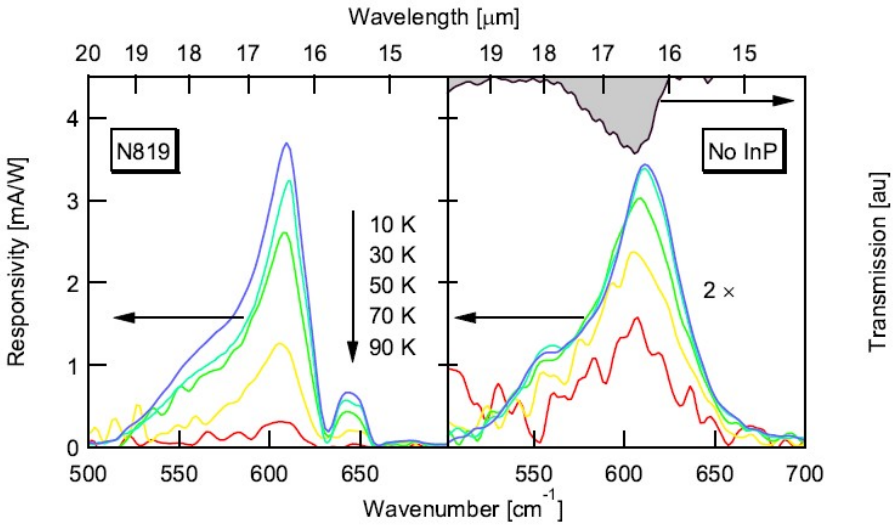

Figure 7.17: *Quantum Cascade Detector mounted on a SMA adapter*

In a second experiment the pulsed 17 μm laser was detected by the QCD. The measured pulses, both laser current and QCD signal, are shown in Fig. 7.18. Like with the MCT, it is obvious that the lasing process is retarded. Here, the Neuchatel QCL drive current electronics were superior to the setup in Cologne as the retardation is only 5 to 10 ns compared to about 150 ns. However, the shortest pulse which could be realised with the electronics was a 5 ns pulse. This sets a lower limit to the bandwidth of the detector of 200 MHz. The real bandwidth though is assumed to be around 10 GHz or higher. With a similar QCD at 5 μm , also developed at Neuchatel, a 23 GHz bandwidth was measured [148]. This result still was limited by the

experimental setup and a bandwidth of 69 GHz was assumed, in the same order as e.g. the 82 GHz obtained for a QWIP [149]. Currently, the bandwidth of THIS is 3 GHz.

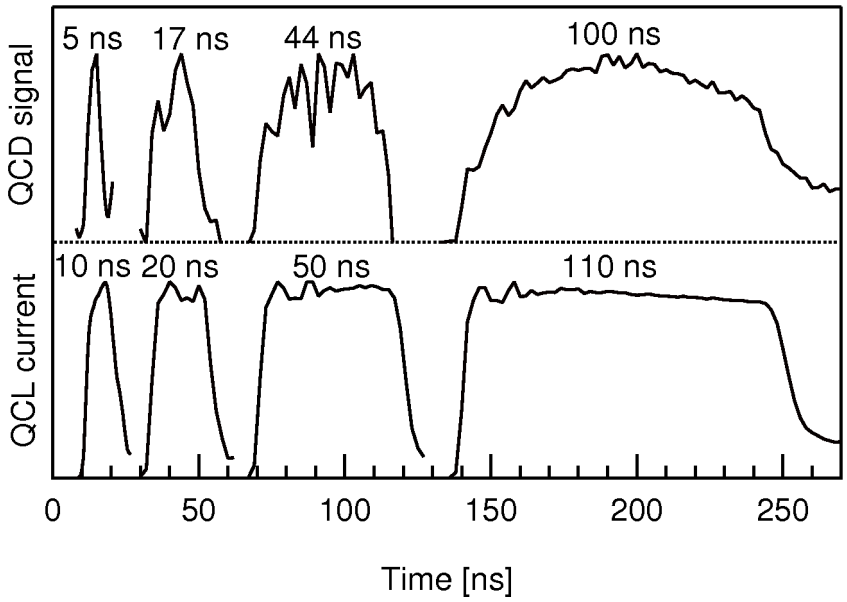

Figure 7.18: *Pulsed laser: lower panel: pulse current. Upper panel: QCD response*

In the last years the evolution of quantum cascade detectors is quickly advanced. Recently a QCD at 14.3 μm with a responsivity of 85 mA/W was presented [150]. If this progress continues, QCDs will be very promising for infrared heterodyne spectroscopy in the future. If responsivities comparable to MCT values at 10 μm will be achieved, QCDs will even allow to increase the bandwidth of infrared heterodyne spectroscopy, which would be favourable when observing in the interstellar medium with objects in galactic scales. Of course, one has to think of way to increase the bandwidth of the spectrometer back-end as well.

7.5 Results and Outlook

Infrared heterodyne spectroscopy at long mid-infrared wavelengths from 12-17 micron will need appropriate and convenient detectors. Although it seems to be possible to observe strong planetary targets around 13 μm using available MCT detectors at liquid helium temperatures new developments are needed for 17 or even 28 micron. Quantum Cascade Detectors are a promising new and rapidly evolving development which could lead to broadband devices with enough sensitivity within the next couple of years. Up to 17 micron, MCTs tailored to the desired wavelength are probably the best, though hardly affordable option to get devices at liquid nitrogen temperature. At telescopes, this would be far more convenient than operating with helium.

Another promising approach for mid-infrared detectors are Superconducting Hot Electron Bolometers (SHEBs), being developed also at the 1st Physics Institute in Cologne [151, 152]. Such Bolometers are state of the art technology used for Terahertz and Radio applications. For example, the GREAT instrument to be flying on board the NASA/DLR airborne observatory SOFIA uses SHEBs as waveguide mixers. First tests with HEB preceding van-der-Pauw structures unfortunately were not successful. As the device is much bigger than those used at THz frequencies, it probably received too much background radiation, which prevented it to reach the superconducting transition temperature. However, this will be subject for future master and PhD thesises in Cologne.

Chapter 8

Outlook

Venus Temperatures

In this thesis temperatures in the upper mesosphere of Venus proved to be highly variable. More data is needed to investigate possible reasons for this variability. More old IRHS data will be re-analysed to increase the data set. Temperature measurements can be used to refine evolving global circulation models which can be cross checked by the observation of mesospheric winds which is done with the same infrared heterodyne spectrum used for temperature retrieval. Ideally, future observations are scheduled simultaneously with other observations such as sub-mm like it was successfully carried out for the first time within this work. This will make it easier to compare between the different retrieval methods. Possible influence from solar activity seems to be unlikely to be observed at altitudes of around 120 km, given the variability being present anyhow. Nevertheless, it might be worth to keep this possibility in mind during future investigations.

Detector Evaluation

MCT detectors seem to be ready for operation at longer wavelength if cooled appropriately. At moderately long wavelength it might be even sufficient to cool to 77 K. This has to be verified in the near future. Other detector types like quantum cascade detectors are de-

veloping fast and might be an alternative solution sometimes.
In the course of future projects, the feasibility of superconducting Hot Electron Bolometers (HEBs) as heterodyne mixer at mid infrared wavelength will be studied. Such devices need liquid helium temperatures to reach the superconducting transition temperature, but promise high sensitivity combined with high bandwidths.

THIS in the Future

Future projects for THIS include the search for Methane in the atmosphere of Mars. Observations of Ethane and Acetylene in the atmosphere of Jupiter and also observations of trace gases like ozone in the atmosphere of the Earth. Of course, more wind and temperature measurements in the atmospheres of Venus and Mars will be done also to continue and refine the work that is being done.
Technically, the next step is the use of broadband QCL devices being controlled and frequency locked by an external cavity set-up. This is the topic of the thesis Dusan Stupar is working on. This will extremely broaden the wavelength coverage of THIS, making it truly 'tuneable'.

Bibliography

[1] M. Sornig. Investigations of upper atmosphere dynamics on mars and venus by high resolution infrared heterodyne spectroscopy of co_2. *Dissertation*, Universität zu Köln, 2009.

[2] G. Sonnabend. Aufbau und Charakterisierung des Infrarot-Heterodyn-Spektrometers THIS. *Dissertation*, Universität zu Köln, 2002.

[3] M. Olbrich. Akusto-optische signalverarbeitung mit dem material rutil. *Dissertation*, Universität zu Köln, 2006.

[4] R. Schieder, V. Tolls, and G. Winnewisser. The Cologne acousto optical spectrometers. *Experimental Astronomy*, 1:101–121, March 1989.

[5] website. http://www.astro.uni-koeln.de/site/workgroups/astro_instrumentation/aos. 2010.

[6] R. F. Kazarinov and R. A. Suris. Possibility of the amplification of electromagnetic waves in a semiconductor with a superlattice. *Soviet Physics Semiconductors*, 5:707ff, 1971.

[7] J. Faist, F. Capasso, D. L. Sivco, C. Sirtori, A. L. Hutchinson, and A. Y. Cho. Quantum Cascade Laser. *Science*, 264:553–556, April 1994.

[8] R. F. Curl, F. Capasso, C. Gmachl, A. A. Kosterev, B. McManus, R. Lewicki, M. Pusharsky, G. Wysocki, and F. K. Tittel. Quantum cascade lasers in chemical physics. *Chemical Physics Letters*, 487:1–18, February 2010.

[9] D. Stupar, J. Krieg, P. Krötz, M. Sornig, G. Sonnabend, T. Giesen, and R. Schieder. Fully reflective external-cavity

setup for quantum-cascade lasers as a local oscillator in mid-infrared wavelength heterodyne spectroscopy. *Applied Optics*, 47:2993ff, 2008.

[10] A. L. Schawlow and C. H. Townes. Infrared and Optical Masers. *Physical Review*, 112:1940–1949, December 1958.

[11] C. Henry. Theory of the linewidth of semiconductor lasers. *IEEE Journal of Quantum Electronics*, 18:259–264, February 1982.

[12] S. Bartalini, S. Borri, P. Cancio, A. Castrillo, I. Galli, G. Giusfredi, D. Mazzotti, L. Gianfrani, and P. de Natale. Observing the Intrinsic Linewidth of a Quantum-Cascade Laser: Beyond the Schawlow-Townes Limit. *Physical Review Letters*, 104(8):083904–+, February 2010.

[13] D. Hofstetter, M. Beck, T. Aellen, and J. Faist. High-temperature operation of distributed feedback quantum-cascade lasers at 5.3 μm. *Applied Physics Letters*, 78:396–+, January 2001.

[14] H. M. Wiseman. Light amplification without stimulated emission: Beyond the standard quantum limit to the laser linewidth. Phys. Rev. A, 60:4083–4093, November 1999.

[15] M. Yamanishi, T. Edamura, K. Fujita, N. Akikusa, and H. Kan. Theory of the Intrinsic Linewidth of Quantum-Cascade Lasers: Hidden Reason for the Narrow Linewidth and Line-Broadening by Thermal Photons. *IEEE Journal of Quantum Electronics*, 44:12–29, January 2008.

[16] M. S. Taubman, T. L. Myers, B. D. Cannon, R. M. Williams, F. Capasso, C. Gmachl, D. L. Sivco, and A. Y. Cho. Frequency stabilization of quantum-cascade lasers by use of optical cavities. *Optics Letters*, 27:2164–2166, December 2002.

[17] G. Sonnabend, D. Wirtz, and R. Schieder. Evaluation of quantum-cascade lasers as local oscillators for infrared heterodyne spectroscopy. *Applied Optics*, 44:7170–7172, November 2005.

[18] N. Mukherjee, R. Go, and C. K. N. Patel. Linewidth measurement of external grating cavity quantum cascade laser using saturation spectroscopy. *Applied Physics Letters*, 92(11):111116–+, March 2008.

[19] M. M. Abbas, L. W. Brown, D. Buhl, T. A. Clark, J. Hillman, T. Kostiuk, V. Kunde, and M. J. Mumma. A 10 Micron Superheterodyne Receiver For Spectral Line Observations. In *Bulletin of the American Astronomical Society*, volume 8 of *Bulletin of the American Astronomical Society*, pages 508–+, September 1976.

[20] J. Goldstein. Absolute wind measurements in the lower thermosphere of venus using infrared heterodyne spectroscopy. *Dissertation*, University of Pennsylvania, 1989.

[21] R. Schieder. Noise at Direct- and Heterodyne-Detection in the Infrared. *submitted to JQSRT*, 2008.

[22] J. H. Lacy, M. J. Richter, T. K. Greathouse, D. T. Jaffe, and Q. Zhu. TEXES: A Sensitive High-Resolution Grating Spectrograph for the Mid-Infrared. PASP, 114:153–168, February 2002.

[23] G. Sonnabend, M. Sornig, P. Krötz, D. Stupar, and R. Schieder. Ultra high spectral resolution observations of planetary atmospheres using the Cologne tuneable heterodyne infrared spectrometer. *Journal of Quantitative Spectroscopy and Radiative Transfer*, 109:1016–1029, April 2008.

[24] S. Bougher, A. Brecht, T. McDunn, A. Valeille, and J. Bell. Model simulations of the upper atmospheres of venus and mars: Processes regulating solar cycle variability. *Talk, International Conference on Comparative Planetology: Venus-Earth-Mars*, May 2009.

[25] A. J. Kliore, V. I. Moroz, and G. M. Keating. The Venus International Reference Atmosphere. *Advances in Space Research*, 5, 1985.

[26] V. I. Moroz and L. V. Zasova. VIRA-2: a review of inputs for updating the Venus International Reference Atmosphere. *Advances in Space Research*, 19:1191–1201, May 1997.

[27] L. V. Zasova, V. I. Moroz, V. M. Linkin, I. V. Khatuntsev, and B. S. Maiorov. Structure of the Venusian atmosphere from surface up to 100 km. *Cosmic Research*, 44:364–383, July 2006.

[28] L. V. Zasova, N. Ignatiev, I. Khatuntsev, and V. Linkin. Structure of the Venus atmosphere. *Planetary and Space Science*, 55:1712–1728, October 2007.

[29] website. http://venus.aeronomie.be/en/venus/temperature greenhouseeffect.htm. 2010.

[30] S. W. Bougher, R. E. Dickinson, E. C. Ridley, R. G. Roble, A. F. Nagy, and T. E. Cravens. Venus mesosphere and thermosphere. II - Global circulation, temperature, and density variations. *Icarus*, 68:284–312, November 1986.

[31] S. W. Bougher and R. G. Roble. Comparative terrestrial planet thermospheres. I - Solar cycle variation of global mean temperatures. J. Geophys. Res., 96:11045–+, July 1991.

[32] A. D. Richmond, E. C. Ridley, and R. G. Roble. A thermosphere/ionosphere general circulation model with coupled electrodynamics. Geophys. Res. Lett., 19:601–604, March 1992.

[33] I. C. F. Müller-Wodarg, R. V. Yelle, M. Mendillo, L. A. Young, and A. D. Aylward. The thermosphere of Titan simulated by a global three-dimensional time-dependent model. J. Geophys. Res., 105:20833–20856, 2000.

[34] S. Lebonnois and M. Sornig. *private communication*.

[35] R. T. Clancy, B. J. Sandor, and G. H. Moriarty-Schieven. Venus upper atmospheric CO, temperature, and winds across the afternoon/evening terminator from June 2007 JCMT submillimeter line observations. *Planetary and Space Science*, 56:1344–1354, August 2008.

[36] M. Rengel, P. Hartogh, and C. Jarchow. Mesospheric vertical thermal structure and winds on Venus from HHSMT CO spectral-line observations. Planet. Space Sci., 56:1368–1384, August 2008.

[37] M. Rengel, P. Hartogh, and C. Jarchow. HHSMT observations of the Venusian mesospheric temperature, winds, and CO abundance around the MESSENGER flyby. Planet. Space Sci., 56:1688–1695, November 2008.

[38] J. Bailey, V. S. Meadows, S. Chamberlain, and D. Crisp. The temperature of the Venus mesosphere from O2 ($a^1\Delta_g$) airglow observations. *Icarus*, 197:247–259, September 2008.

[39] P. Connes, J. F. Noxon, W. A. Traub, and N. P. Carleton. O_2 ($a^1\Delta_g$ emission in the day and night airglow of Venus. ApJ, 233:L29–L32, October 1979.

[40] D. Crisp, V. S. Meadows, B. Bézard, C. de Bergh, J.-P. Maillard, and F. P. Mills. Ground-based near-infrared observations of the Venus nightside: 1.27-μm O_2(aΔ_g) airglow from the upper atmosphere. J. Geophys. Res., 101:4577–4594, 1996.

[41] P. Drossart, G. Piccioni, J. C. Gérard, M. A. Lopez-Valverde, A. Sanchez-Lavega, L. Zasova, R. Hueso, F. W. Taylor, B. Bézard, A. Adriani, F. Angrilli, G. Arnold, K. H. Baines, G. Bellucci, J. Benkhoff, J. P. Bibring, A. Blanco, M. I. Blecka, R. W. Carlson, A. Coradini, A. di Lellis, T. Encrenaz, S. Erard, S. Fonti, V. Formisano, T. Fouchet, R. Garcia, R. Haus, J. Helbert, N. I. Ignatiev, P. Irwin, Y. Langevin, S. Lebonnois, D. Luz, L. Marinangeli, V. Orofino, A. V. Rodin, M. C. Roos-Serote, B. Saggin, D. M. Stam, D. Titov, G. Visconti, M. Zambelli, C. Tsang, E. Ammannito, A. Barbis, R. Berlin, C. Bettanini, A. Boccaccini, G. Bonnello, M. Bouyé, F. Capaccioni, A. Cardesin, F. Carraro, G. Cherubini, M. Cosi, M. Dami, M. de Nino, D. Del Vento, M. di Giampietro, A. Donati, O. Dupuis, S. Espinasse, A. Fabbri, A. Fave, I. Ficai Veltroni, G. Filacchione, K. Garceran, Y. Ghomchi, M. Giustizi, B. Gondet, Y. Hello, F. Henry, S. Hofer, G. Huntzinger, J. Kachlicki, R. Knoll, D. Kouach, A. Mazzoni, R. Melchiorri, G. Mondello, F. Monti, C. Neumann, F. Nuccilli, J. Parisot, C. Pasqui, S. Perferi, G. Peter, A. Piacentino, C. Pompei, J.-M. Réess, J.-P. Rivet, A. Romano, N. Russ, M. Santoni, A. Scarpelli, A. Sémery, A. Soufflot, D. Stefanovitch, E. Suetta, F. Tarchi, N. Tonetti, F. Tosi, and B. Ulmer. A dynamic upper atmosphere of Venus as revealed by VIRTIS on Venus Express. *Nature*, 450:641–645, November 2007.

[42] C. Roldan, M. A. Lopez-Valverde, M. Lopez-Puertas, and D. P. Edwards. Non-LTE Infrared Emissions of CO_2 in the Atmosphere of Venus. *Icarus*, 147:11–25, September 2000.

[43] M.A. Lopez-Valverde, G. Sonnabend, M. Sornig, and P. Kroetz. Modelling the atmosphereic CO_2 10-/mm laser emission in Mars and Venus at high spectral resolution. *submitted to Planetary Space Sciences*, 2009.

[44] D. Grassi, P. Drossart, G. Piccioni, N. I. Ignatiev, L. V. Zasova, A. Adriani, M. L. Moriconi, P. G. J. Irwin, A. Negrão, and A. Migliorini. Retrieval of air temperature profiles in the Venusian mesosphere from VIRTIS-M data: Description and vali-

dation of algorithms. *Journal of Geophysical Research (Planets)*, 113:0–+, October 2008.

[45] J.-L. Bertaux, A.-C. Vandaele, O. Korablev, E. Villard, A. Fedorova, D. Fussen, E. Quémerais, D. Belyaev, A. Mahieux, F. Montmessin, C. Muller, E. Neefs, D. Nevejans, V. Wilquet, J. P. Dubois, A. Hauchecorne, A. Stepanov, I. Vinogradov, A. Rodin, J.-L. Bertaux, D. Nevejans, O. Korablev, F. Montmessin, A.-C. Vandaele, A. Fedorova, M. Cabane, E. Chassefière, J. Y. Chaufray, E. Dimarellis, J. P. Dubois, A. Hauchecorne, F. Leblanc, F. Lefèvre, P. Rannou, E. Quémerais, E. Villard, D. Fussen, C. Muller, E. Neefs, E. van Ransbeeck, V. Wilquet, A. Rodin, A. Stepanov, I. Vinogradov, L. Zasova, F. Forget, S. Lebonnois, D. Titov, S. Rafkin, G. Durry, J. C. Gérard, and B. Sandel. A warm layer in Venus' cryosphere and high-altitude measurements of HF, HCl, H_2O and HDO. Nature, 450:646–649, November 2007.

[46] R. T. Clancy, B. J. Sandor, and G. H. Moriarty-Schieven. Observational definition of the Venus mesopause: vertical structure, diurnal variation, and temporal instability. *Icarus*, 161:1–16, January 2003.

[47] E. Lellouch, J. J. Goldstein, J. Rosenqvist, S. W. Bougher, and G. Paubert. Global circulation, thermal structure, and carbon monoxide distribution in Venus' mesosphere in 1991. *Icarus*, 110:315–339, August 1994.

[48] M. Pätzold, B. Häusler, M. K. Bird, S. Tellmann, R. Mattei, S. W. Asmar, V. Dehant, W. Eidel, T. Imamura, R. A. Simpson, and G. L. Tyler. The structure of Venus' middle atmosphere and ionosphere. *nature*, 450:657–660, nov 2007.

[49] S. Tellmann, M. Pätzold, B. Häusler, M. K. Bird, and G. L. Tyler. Structure of the Venus neutral atmosphere as observed by the Radio Science experiment VeRa on Venus Express. *Journal of Geophysical Research (Planets)*, 114(E13):0–+, April 2009.

[50] A. L. Betz, M. A. Johnson, R. A. McLaren, and E. C. Sutton. Heterodyne detection of CO2 emission lines and wind velocities in the atmosphere of Venus. ApJ, 208:L141–L144, September 1976.

[51] M. J. Mumma, D. Buhl, G. Chin, D. Deming, F. Espenak, T. Kostiuk, and D. Zipoy. Discovery of natural gain amplifica-

tion in the 10-micrometer carbon dioxide laser bands on Mars - A natural laser. *Science*, 212:45–49, April 1981.

[52] D. Deming and M. J. Mumma. Modeling of the 10-micron natural laser emission from the mesospheres of Mars and Venus. *Icarus*, 55:356–368, September 1983.

[53] M. A. López-Valverde, P. Drossart, R. Carlson, R. Mehlman, and M. Roos-Serote. Non-LTE infrared observations at Venus: From NIMS/Galileo to VIRTIS/Venus Express. Planet. Space Sci., 55:1757–1771, October 2007.

[54] E. Lellouch, T. Clancy, D. Crisp, A.J. Kliore, D. Titov, and S.W. Bougher. Monitoring of Mesospheric Structure and Dynamics. In S. Bougher, D. Hunten, and Phillips R., editors, *Venus II*, pages 295–324. University of Arizona Press, Tucson, 1997.

[55] D. Deming, F. Espenak, D. Jennings, T. Kostiuk, M. Mumma, and D. Zipoy. Observations of the 10-micron natural laser emission from the mesospheres of Mars and Venus. *Icarus*, 55:347–355, September 1983.

[56] G. Gilli, M. A. López-Valverde, P. Drossart, G. Piccioni, S. Erard, and A. Cardesín Moinelo. Limb observations of CO_2 and CO non-LTE emissions in the Venus atmosphere by VIRTIS/Venus Express. *Journal of Geophysical Research (Planets)*, 114(E13):0–+, March 2009.

[57] W. C. Maguire, J. C. Pearl, M. D. Smith, B. J. Conrath, A. A. Kutepov, M. S. Kaelberer, E. Winter, and P. R. Christensen. Observations of high-altitude CO_2 hot bands in Mars by the orbiting Thermal Emission Spectrometer. *Journal of Geophysical Research (Planets)*, 107:5063–+, September 2002.

[58] G. Sonnabend, M. Sornig, P. Krötz, R. Schieder, and K. E. Fast. High spatial resolution mapping of Mars mesospheric zonal winds by infrared heterodyne spectroscopy of CO_2. *Geophysical Research Letters*, 33:18201, September 2006.

[59] F. Schmülling, B. ;. Klumb, M. Harter, R. Schieder, B. Vowinkel, and G. Winnewisser. High-sensitivity mid-infrared heterodyne spectrometer with a tunable diode laser as a local oscillator. *Appl. Opt.*, 37:5771–5776, August 1998.

[60] P. Bernath. *Spectra of Atoms and Molecules*. Oxford University Press, 2005.

[61] T. Hewagama, J. Goldstein, T. A. Livengood, D. Buhl, F. Espenak, K. Fast, T. Kostiuk, and F. Schmülling. Beam Integrated High-Resolution Infrared Spectra: Accurate Modeling of Thermal Emission from Extended Clear Atmospheres. J. Quant. Spec. Radiat. Transf., 109:1098–1117, 2008.

[62] D. P. Edwards. GENLN2: A general line-by-line atmospheric transmittance and radiance model. Version 3.0: Description and users guide. Technical report, January 1992.

[63] G. Herzberg. *Molecular Spectra and Molecular Structure*. van Nostrand Reinhold Company, 1939.

[64] T. J. Bridges and T. Y. Chang. Accurate Rotational Constants of $C^{12}O_2^{16}$ from Measurement of cw Beats in Bulk GaAs Between CO_2 Vibrational-Rotational Laser Lines. *Physical Review Letters*, 22:811–814, April 1969.

[65] D. V. Titov, F. W. Taylor, H. Svedhem, N. I. Ignatiev, W. J. Markiewicz, G. Piccioni, and P. Drossart. Atmospheric structure and dynamics as the cause of ultraviolet markings in the clouds of Venus. Nature, 456:620–623, December 2008.

[66] G. Piccioni, P. Drossart, and Sanchez-Lavega et al. South-polar features on Venus similar to those near the north pole. *Natur*, 450:637–640, November 2007.

[67] M. A. Lopez-Valverde. *private communication*.

[68] A. J. Kliore and L. F. Mullen. Solar-cycle changes in the thermal structure of the Venus dayside ionosphere. *Advances in Space Research*, 10:15–29, 1990.

[69] A. J. Kliore. Solar Cycle Changes in Venus Upper Atmosphere Temperatures. In *Bulletin of the American Astronomical Society*, volume 21 of *Bulletin of the American Astronomical Society*, pages 925–+, June 1989.

[70] websites. http://www.swpc.noaa.gov/solarcycle/ and http://sidc.oma.be. 2010.

[71] R. T. Clancy and D. O. Muhleman. Long-term (1979-1990) changes in the thermal, dynamical, and compositional structure of the Venus mesosphere as inferred from microwave spectral line observations of C-12O, C-13O, and CO-18. *Icarus*, 89:129–146, January 1991.

[72] S. Tingle. *private communication*.

[73] A. E. Hedin, H. B. Niemann, W. T. Kasprzak, and A. Seiff. Global empirical model of the Venus thermosphere. J. Geophys. Res., 88:73–83, January 1983.

[74] A. Brecht, S. Bougher, S. Rafkin, and B. Foster. Venus Upper Atmosphere Winds Traced by Night Airglow Distributions: NCAR VTGCM Simulations. *Poster, AGU Fall Meeting*, December 2007.

[75] M. Sornig, T. Livengood, G. Sonnabend, P. Kroetz, D. Stupar, T. Kostiuk, and R. Schieder. Venus upper atmosphere winds from ground-based heterodyne spectroscopy of CO_2 at 10μm wavelength. *Planetary and Space Science*, 56:1399–1406, August 2008.

[76] M. Sornig, G. Sonnabend, P. Kroetz, and D. Stupar. *in preparation*.

[77] N. Ryde, A. J. Korn, M. J. Richter, and F. Ryde. The Zeeman-sensitive Emission Lines of Mg I at 12 Microns in Procyon. ApJ, 617:551–558, December 2004.

[78] website. http://eo.nso.edu/rasl/user_area/rasl_teachguide.html. 2010.

[79] F. Lahuis, E. F. van Dishoeck, A. C. A. Boogert, K. M. Pontoppidan, G. A. Blake, C. P. Dullemond, N. J. Evans, II, M. R. Hogerheijde, J. K. Jørgensen, J. E. Kessler-Silacci, and C. Knez. Hot Organic Molecules toward a Young Low-Mass Star: A Look at Inner Disk Chemistry. ApJ, 636:L145–L148, January 2006.

[80] A. Dalgarno. Molecular processes in the early universe. *Journal of Physics: Conference Series*, 4:10 ff, 2005.

[81] F. Palla, E. E. Salpeter, and S. W. Stahler. Primordial star formation - The role of molecular hydrogen. ApJ, 271:632–641, August 1983.

[82] S. Lepp, P. C. Stancil, and A. Dalgarno. TOPICAL REVIEW: Atomic and molecular processes in the early Universe . *Journal of Physics B*, 35:57 ff, May 2002.

[83] E. Habart, M. Walmsley, L. Verstraete, S. Cazaux, R. Maiolino, P. Cox, F. Boulanger, and G. P. Des Forêts. Molecular Hydrogen. *Space Science Reviews*, 119:71–91, August 2005.

[84] E. Habart, F. Boulanger, L. Verstraete, C. M. Walmsley, and G. Pineau des Forêts. Some empirical estimates of the H_2 formation rate in photon-dominated regions. A&A, 414:531–544, February 2004.

[85] S. Cazaux and A. G. G. M. Tielens. Molecular Hydrogen Formation in the Interstellar Medium. ApJ, 575:L29–L32, August 2002.

[86] T. R. Geballe and T. Oka. Detection of H_3^+ in interstellar space. Nature, 384:334–335, November 1996.

[87] F. Combes and D. Pfenniger. Perspectives for detecting cold H_2 in outer galactic disks. A&A, 327:453–466, November 1997.

[88] P. Kalberla, J. Kerp, and U. Haud. The Galactic Dark Matter Halo: Is it H_2? In *H_2 in space*, page 297 ff. Cambridge University Press, 2001.

[89] M. G. Burton, D. J. Hollenbach, and A. G. G. Tielens. Mid-infrared rotational line emission from interstellar molecular hydrogen. ApJ, 399:563 ff, November 1992.

[90] T. M. Dame, D. Hartmann, and P. Thaddeus. The Milky Way in Molecular Clouds: A New Complete CO Survey. ApJ, 547:792–813, February 2001.

[91] W. F. Thi, G. A. Blake, E. F. van Dishoeck, G. J. van Zadelhoff, J. M. M. Horn, E. E. Becklin, V. Mannings, A. I. Sargent, M. E. van den Ancker, and A. Natta. Substantial reservoirs of molecular hydrogen in the debris disks around young stars. Nature, 409:60–63, January 2001.

[92] A. Lecavelier des Etangs, A. Vidal-Madjar, A. Roberge, P. D. Feldman, M. Deleuil, M. André, W. P. Blair, J.-C. Bouret, J.-M. Désert, R. Ferlet, S. Friedman, G. Hébrard, M. Lemoine, and H. W. Moos. Deficiency of molecular hydrogen in the disk of β Pictoris. Nature, 412:706–708, August 2001.

[93] E. F. van Dishoeck, A. E. Glassgold, M. Guelin, D. T. Jaffe, D. A. Neufeld, A. G. G. M. Tielens, and C. M. Walmsley. Panel Discussion : the CO/H_2 Abundance Ratio. In *Astrochemistry of Cosmic Phenomena*, volume 150, page 285 ff, 1992.

[94] F. P. Israel. H_2 and its relation to CO in the LMC and other magellanic irregular galaxies. A&A, 328:471–482, December 1997.

[95] R. B. Larson. Numerical calculations of the dynamics of collapsing proto-star. MNRAS, 145:271–+, 1969.

[96] C. P. Dullemond, D. Hollenbach, I. Kamp, and P. D'Alessio. Models of the Structure and Evolution of Protoplanetary Disks. In *Protostars and Planets V*, page 555 ff, 2007.

[97] M. R. Meyer, L. A. Hillenbrand, and D. E. Backman et al. The Formation and Evolution of Planetary Systems: First Results from a Spitzer Legacy Science Program. ApJS, 154:422–427, September 2004.

[98] M. A. Bitner, M. J. Richter, J. H. Lacy, T. K. Greathouse, D. T. Jaffe, and G. A. Blake. TEXES Observations of Pure Rotational H_2 Emission from AB Aurigae. ApJ, 661:L69–L72, May 2007.

[99] S. P. Quanz, T. Henning, J. Bouwman, H. Linz, and F. Lahuis. Deeply Embedded Objects and Shocked Molecular Hydrogen: The Environment of the FU Orionis Stars RNO 1B/1C. ApJ, 658:487–497, March 2007.

[100] C. Martin-Zaïdi, P.-O. Lagage, E. Pantin, and E. Habart. Detection of Warm Molecular Hydrogen in the Circumstellar Disk around the Herbig Ae Star HD 97048. ApJ, 666:L117–L120, September 2007.

[101] A. Carmona, M. E van den Ancker, T. Henning, Y. Pavlyuchenkov, C. P. Dullemond, M. Goto, W. F-. Thi, J. Bouwman, and L. B. F. M. Waters. A Search for Mid-Infrared Molecular Hydrogen Emission from Protoplanetary Disks. *accepted by A&A*, October 2007.

[102] H. B. Niemann, S. K. Atreya, G. R. Carignan, T. M. Donahue, J. A. Haberman, D. N. Harpold, R. E. Hartle, D. M. Hunten, W. T. Kasprzak, P. R. Mahaffy, T. C. Owen, and S. H. Way. The composition of the Jovian atmosphere as determined by the Galileo probe mass spectrometer. J. Geophys. Res., 103:22831–22846, September 1998.

[103] V. G. Kunde, F. M. Flasar, D. E. Jennings, B. Bézard, D. F. Strobel, B. J. Conrath, C. A. Nixon, G. L. Bjoraker, P. N. Romani, R. K. Achterberg, A. A. Simon-Miller, P. Irwin, J. C. Brasunas, J. C. Pearl, M. D. Smith, G. S. Orton, P. J. Gierasch, L. J. Spilker, R. C. Carlson, A. A. Mamoutkine, S. B. Calcutt, P. L. Read, F. W. Taylor, T. Fouchet, P. Parrish, A. Barucci, R. Courtin,

A. Coustenis, D. Gautier, E. Lellouch, A. Marten, R. Prangé, Y. Biraud, C. Ferrari, T. C. Owen, M. M. Abbas, R. E. Samuelson, F. Raulin, P. Ade, C. J. Césarsky, K. U. Grossman, and A. Coradini. Jupiter's Atmospheric Composition from the Cassini Thermal Infrared Spectroscopy Experiment. *Science*, 305:1582–1587, September 2004.

[104] V. A. Krasnopolsky and P. D. Feldman. Detection of Molecular Hydrogen in the Atmosphere of Mars. *Science*, 294:1914–1917, November 2001.

[105] E. Wigner and H. B. Huntington. On the Possibility of a Metallic Modification of Hydrogen. J. Chem. Phys., 3:764–770, December 1935.

[106] W. J. Nellis, M. Ross, and N. C. Holmes. Temperature Measurements of Shock-Compressed Liquid Hydrogen: Implications for the Interior of Jupiter. *Science*, 269:1249–1252, September 1995.

[107] T. Guillot, D. J. Stevenson, W. B. Hubbard, and D. Saumon. The interior of jupiter. In *Jupiter. The Planet, Satellites and Magnetosphere*, page 35 ff. Cambridge Univ. Press, 2004.

[108] S. V. Vorontsov, V. N. Zharkov, and V. M. Lubimov. The free oscillations of Jupiter and Saturn. *Icarus*, 27:109–118, January 1976.

[109] F.-X. Schmider, E. Fossat, and B. Mosser. Possible detection of Jovian global oscillations. A&A, 248:281–291, August 1991.

[110] B. Mosser, D. Gautier, and T. Kostiuk. On the detectability of Jovian oscillations with infrared heterodyne measurements. *Icarus*, 96:15–26, March 1992.

[111] G. Chabrier, D. Saumon, W. B. Hubbard, and J. I. Lunine. The molecular-metallic transition of hydrogen and the structure of Jupiter and Saturn. ApJ, 391:817–826, June 1992.

[112] G. S. Orton, J. H. Lacy, J. M. Achtermann, P. Parmar, and W. E. Blass. Thermal spectroscopy of Neptune - The stratospheric temperature, hydrocarbon abundances, and isotopic ratios. *Icarus*, 100:541–555, December 1992.

[113] G. S. Orton. *private communication*.

[114] T. Hewagama, J. Goldstein, D. Buhl, F. Espenak, K. Fast, T. Kostiuk, and T. A. Livengood. Spectral Line Analysis for Planetary Atmospheric Dynamics Retrieval. In *Bulletin of the American Astronomical Society*, page 1093 ff, September 1998.

[115] G. S. Orton, M. Gustafsson, M. Burgdorf, and V. Meadows. Revised ab initio models for H_2/H_2 collision-induced absorption at low temperatures. *Icarus*, 189:544–549, August 2007.

[116] G. Sonnabend, D. Wirtz, R. Schieder, and P. F. Bernath. High-Resolution Infrared Measurements of H_2O and SiO in Sunspots. *Applied Optics*, 233:205–213, February 2006.

[117] M. F. Kessler, J. A. Steinz, M. E. Anderegg, J. Clavel, G. Drechsel, P. Estaria, J. Faelker, J. R. Riedinger, A. Robson, B. G. Taylor, and S. Ximenez de Ferran. The Infrared Space Observatory (ISO) mission. A&A, 315:L27–L31, November 1996.

[118] E. F. van Dishoeck. ISO Spectroscopy of Gas and Dust: From Molecular Clouds to Protoplanetary Disks. ARA&A, 42:119–167, September 2004.

[119] H. W. Moos, W. C. Cash, L. L. Cowie, A. F. Davidsen, A. K. Dupree, P. D. Feldman, S. D. Friedman, J. C. Green, R. F. Green, C. Gry, J. B. Hutchings, E. B. Jenkins, J. L. Linsky, R. F. Malina, A. G. Michalitsianos, B. D. Savage, J. M. Shull, O. H. W. Siegmund, T. P. Snow, G. Sonneborn, A. Vidal-Madjar, A. J. Willis, B. E. Woodgate, D. G. York, T. B. Ake, B.-G. Andersson, J. P. Andrews, R. H. Barkhouser, L. Bianchi, W. P. Blair, K. R. Brownsberger, A. N. Cha, P. Chayer, S. J. Conard, A. W. Fullerton, G. A. Gaines, R. Grange, M. A. Gummin, G. Hebrard, G. A. Kriss, J. W. Kruk, D. Mark, D. K. McCarthy, C. L. Morbey, R. Murowinski, E. M. Murphy, W. R. Oegerle, R. G. Ohl, C. Oliveira, S. N. Osterman, D. J. Sahnow, M. Saisse, K. R. Sembach, H. A. Weaver, B. Y. Welsh, E. Wilkinson, and W. Zheng. Overview of the Far Ultraviolet Spectroscopic Explorer Mission. ApJ, 538:L1–L6, July 2000.

[120] M. W. Werner, T. L. Roellig, F. J. Low, G. H. Rieke, M. Rieke, W. F. Hoffmann, E. Young, J. R. Houck, B. Brandl, G. G. Fazio, J. L. Hora, R. D. Gehrz, G. Helou, B. T. Soifer, J. Stauffer, J. Keene, P. Eisenhardt, D. Gallagher, T. N. Gautier, W. Irace, C. R. Lawrence, L. Simmons, J. E. Van Cleve, M. Jura, E. L. Wright, and D. P. Cruikshank. The Spitzer Space Telescope Mission. ApJS, 154:1–9, September 2004.

[121] J. S. Arabadjis and J. N. Bregman. Measuring Molecular, Neutral Atomic, and Warm Ionized Galactic Gas through X-Ray Absorption. ApJ, 510:806–821, January 1999.

[122] M. van den Ancker, P. R. Wesselius, and A. G. G. M. Tielens. ISO Spectroscopy of H_2 in Star Forming Regions. In *H_2 in space*, page 139 ff. Cambridge University Press, 2001.

[123] E. F. van Dishoeck, C. M. Wright, J. Cernicharo, E. Gonzalez-Alfonso, T. de Graauw, F. P. Helmich, and B. Vandenbussche. The ISO-SWS 2.4-45.2 Micron Spectrum Toward Orion IR c2. ApJ, 502:L173 ff, August 1998.

[124] D. A. Neufeld, G. J. Melnick, P. Sonnentrucker, E. A. Bergin, J. D. Green, K. H. Kim, D. M. Watson, W. J. Forrest, and J. L. Pipher. Spitzer Observations of HH 54 and HH 7-11: Mapping the H_2 Ortho-to-Para Ratio in Shocked Molecular Gas. ApJ, 649:816–835, October 2006.

[125] E. Habart, F. Boulanger, L. Verstraete, G. Pineau des Forêts, E. Falgarone, and A. Abergel. H_2 infrared line emission across the bright side of the rho Ophiuchi main cloud. A&A, 397:623–634, January 2003.

[126] P. N. Appleton, K. C. Xu, W. Reach, M. A. Dopita, Y. Gao, N. Lu, C. C. Popescu, J. W. Sulentic, R. J. Tuffs, and M. S. Yun. Powerful High-Velocity Dispersion Molecular Hydrogen Associated with an Intergalactic Shock Wave in Stephan's Quintet. ApJ, 639:L51–L54, March 2006.

[127] S. J. Higdon, J. L. Higdon, and J. Marshall. First Detection of PAHs and Warm Molecular Hydrogen in Tidal Dwarf Galaxies. ApJ, 640:768–783, April 2006.

[128] P. D. Feldman, H. A. Weaver, and E. B. Burgh. Far Ultraviolet Spectroscopic Explorer Observations of CO and H_2 Emission in Comet C/2001 A2 (LINEAR). ApJ, 576:L91–L94, September 2002.

[129] H. Bluhm, K. S. de Boer, O. Marggraf, P. Richter, and B. P. Wakker. Interstellar H_2 in M 33 detected with FUSE. A&A, 398:983–991, February 2003.

[130] P. Richter, K. R. Sembach, B. P. Wakker, and B. D. Savage. Molecular Hydrogen in High-Velocity Clouds. ApJ, 562:L181–L184, December 2001.

[131] J. H. Lacy, R. Knacke, T. R. Geballe, and A. T. Tokunaga. Detection of absorption by H_2 in molecular clouds: A direct measurement of the H2:CO ratio. ApJ, 428:L69–L72, June 1994.

[132] P. S. Parmar, J. H. Lacy, and J. M. Achtermann. Detection of low-J pure-rotational emission from H2 in the Orion Bar region - Evidence for small-scale clumpiness. ApJ, 372:L25–L28, May 1991.

[133] M. J. Richter, D. T. Jaffe, G. A. Blake, and J. H. Lacy. Looking for Pure Rotational H_2 Emission from Protoplanetary Disks. ApJ, 572:L161–L164, June 2002.

[134] K. N. Allers, D. T. Jaffe, J. H. Lacy, B. T. Draine, and M. J. Richter. H_2 Pure Rotational Lines in the Orion Bar. ApJ, 630:368–380, September 2005.

[135] L. Barrière-Fouchet, J.-F. Gonzalez, J. R. Murray, R. J. Humble, and S. T. Maddison. Dust distribution in protoplanetary disks. Vertical settling and radial migration. A&A, 443:185–194, November 2005.

[136] M. Bester, W. C. Danchi, D. Hale, C. H. Townes, C. G. Degiacomi, D. Mekarnia, and T. R. Geballe. Measurement at 11 Micron Wavelengths of the Diameters of alpha Orionis and alpha Scorpii: Changes in Effective Temperature of alpha Orionis and Very Recent Dust Emission. ApJ, 463:336 ff, May 1996.

[137] D. Wirtz. Erste Beobachtungen mit dem abstimmbaren Infrarot-Heterodynsystem THIS. *Dissertation*, Universität zu Köln, 2005.

[138] website. http://www.korth.de/transmiss. 2010.

[139] J. Bruno. Maxion Technologies, inc. *private communication*.

[140] J. Faist. ETH Zuerich. *private communication*.

[141] M. Reine. Fundamental properties of mercury cadmium telluride. In *Encyclopedia of Modern Optics*. Academic Press, London, 2004.

[142] M. Rochat, D. Hofstetter, M. Beck, and J. Faist. Long-wavelength (λ˜16 μm), room-temperature, single-frequency quantum-cascade lasers based on a bound-to-continuum transition. *Applied Physics Letters*, 79:4271 ff, December 2001.

[143] D. Hofstetter, M. Beck, and J. Faist. Quantum-cascade-laser structures as photodetectors. *Applied Physics Letters*, 81:2683–+, October 2002.

[144] L. Gendron, C. Koeniguer, X. Marcadet, and V. Berger. Quantum cascade detectors. *Infrared Physics and Technology*, 47:175–181, October 2005.

[145] D. Hofstetter, F. R. Giorgetta, E. Baumann, Q. Yang, C. Manz, and K. Köhler. Mid-infrared quantum cascade detectors for applications in spectroscopy and pyrometry. *Applied Physics B: Lasers and Optics*, pages 135–+, March 2010.

[146] F. R. Giorgetta, E. Baumann, M. Graf, L. Ajili, N. Hoyler, M. Giovannini, J. Faist, D. Hofstetter, P. Krötz, and G. Sonnabend. 16.5 μm quantum cascade detector using miniband transport. *Applied Physics Letters*, 90(23):231111–+, June 2007.

[147] F. R. Giorgetta. Design, fabrication, and testing of intersubband infrared photodetectors operating at wavelengths between 2μm and 17μm . *Dissertation*, University of Neuchatel, 2007.

[148] D. Hofstetter, M. Graf, T. Aellen, J. Faist, L. Hvozdara, and S. Blaser. 23 GHz operation of a room temperature photovoltaic quantum cascade detector at 5.35 μm. *Applied Physics Letters*, 89:1119 ff, August 2006.

[149] H. C. Liu, J. Li, E. R. Brown, K. A. McIntosh, K. B. Nichols, and M. J. Manfra. Quantum well intersubband heterodyne infrared detection up to 82 GHz. *Applied Physics Letters*, 67:1594–1596, September 1995.

[150] A. Buffaz, L. Doyennette, V. Berger, M. Carras, and A. Nedelcu. Quantum cascade detectors for long wave infrared detection. *Talk, The 10th International Conference on Intersubband Transitions in Quantum Wells*, 2009.

[151] S. Bedorf. Development of ultrathin niobium nitride and niobium titanium nitride films for thz hot-electron bolometers. *Dissertation*, Universität zu Köln, 2006.

[152] P. Munoz-Pradas. Waveguide heterodyne mixers at thz-frequencies — superconducting hot electron bolometers on 2-Âµm si3n4 membranes for great and condor. *Dissertation*, Universität zu Köln, 2007.

Acknowledgements

This work would have not been possible without the support of many people.
First, I would like to thank Prof. Rudolf Schieder for supervising this thesis, for many fruitful discussions and the guidance during the past years. Many thanks to Prof. Susanne Crewell for co-reviewing this thesis.

The data of the Goddard Infrared Heterodyne Spectrometer from 1990-91 were provided by Goddard Heterodyne HIPWAC team. A big thank you therefore to Ted Kostiuk, Jeff Goldstein, Frank Schmülling, Kelly Fast, Tim Livengood, John Annen, Juan Delgado, and Tilak Hewagama. Also for making music together and sharing dinner at Mio's.

Special thanks to the THIS group, Guido Sonnabend, Manuela Sornig, Dusan Stupar and Tobias Stangier for all the fun at the observing runs, conference dinners, garden parties, for singing 'The Internationale' in a US rental car and much more. And, of course, for many discussions about the Venus' atmosphere, adjusting sessions in the lab, and invaluable scientific input during the last years.

Many people at the 1. Physics Institute also contributed to the success of this work:
I want to thank Patrick Pütz for the help with the liquid helium handling, Uwe Lindhorst, Bernhard Schmidt and Frank Bielau for electronics support, the whole fine-mechanical workshop for always accurate work and for trusting my technical drawings. The spectroscopy group not only for inviting my to the christmas parties, but for providing their leak detector - although it was broke. Special thanks therefore to Urs Graf for providing a *working* leak detector!
Thanks to Prof. Jürgen Stutzki and PD Carsten Kramer for proof reading the DFG grant application on molecular hydrogen.

Thanks to Esther Baumann, Fabrizio Giorgetta and Daniel Hofstetter (Uni. Neuchatel) for providing the QCD device and for measuring together. Also I want to acknowledge the provision of the 17 μm pulsed laser by Jerome Faist (Neuchatel, now ETH Zuerich).

The observing runs would not have been possible without the dedicated support of the staff on site. Especially, I want to thank Eric Galayda and Claude Plymate for the support at the McMath-Pierce Solar Telescope. They always pulled a rabbit out of a hat when we were wondering if the telescope now was irreversibly broke.

Thanks to Miguel Angel Lopez Valverde (Instituto de Astrofisica de Andalusia, Granada) I got insight into modelling the non-LTE emission. Also thanks to Susannah Tingle, Imperial Colege London, for sharing information about their model.

Vielen Dank meinem Bruder Martin für sein beharrliches Korrekturlesen!

Am meisten Dank gebührt jedoch Dominique für ihr Dasein und ihre Liebe.

Ich versichere, dass ich die vorgelegte Dissertation selbstständig und ohne unzulässige Hilfe angefertigt, die benutzten Quellen und Hilfsmittel vollständig angegeben und die Stellen der Arbeit - einschließlich Tabellen, Karten und Abbildungen -, die anderen Werken im Wortlaut oder dem Sinn nach entnommen sind, in jedem Einzelfall als Entlehnung kenntlich gemacht habe, dass diese Dissertation noch keiner anderen Fakultät zur Prüfung vorgelegen hat, dass sie abgesehen von unten angegebenen Teilpublikationen noch nicht veröffentlicht worden ist und dass ich eine solche Veröffentlichung vor Abschluss des Promotionsverfahrens nicht vornehmen werde.
Die Bestimmungen der geltenden Promotionsordnung sind mir bekannt. Die von mir vorgelegte Dissertation ist von Herrn Prof. Dr. Rudolf Schieder betreut worden.

Nachfolgend genannte Teilpublikationen liegen vor:

P. Krötz, F. Schmülling, T. Kostiuk, J. Goldstein, G. Sonnabend, M. Sornig, D. Stupar and R. Schieder. Long-term observations of Venus upper mesospheric temperatures from ground based spectroscopy of CO_2. *Icarus* in preparation

P. Krötz, D. Stupar, J. Krieg et al. Applications for Quantum Cascade Lasers and Detectors in Mid-Infrared High-Resolution Heterodyne Astronomy. In *Applied Physics B*, Vol. 90, 2, 187, 2008

G. Sonnabend, P. Krötz, M. Sornig and D. Stupar Direct observations of Venus upper mesospheric temperatures from ground based spectroscopy of CO_2. accepted for publication, *Geophysical Research Letters* 2010

F. Giorgetta, E. Baumann, P. Krötz et al. 16.5 μm quantum cascade detector using miniband transport. In *Applied Physics Letters*, Vol. 90, 231111, 2008

G. Sonnabend, M. Sornig, R. Schieder, et al. Temperatures in Venus upper atmosphere from mid-infrared heterodyne spectroscopy of CO_2 around 10 μm wavelength. In *Planetary and Space Sciences*, Vol. 56 1407 2008

Ich versichere, dass ich alle Angaben wahrheitsgemäß nach bestem Wissen und Gewissen gemacht habe und verpflichte mich, jedmögliche, die obigen Angaben betreffenden Veränderung, dem Dekanat unverzüglich mitzuteilen.

.....	.....
Datum	Unterschrift